Study of the Observables of Highly Compressed Baryonic Matter Produced in Nucleus-Nucleus Collision in CBM Experiment at FAIR

Dissertation
submitted for the award of the degree of
Master of Philosophy
in
Physics
by

Shabir Ahmad

Under the Supervision of

Dr. M. Farooq Mir

Department of Physics,
University of Kashmir, Srinagar, 190 006

January, 2012

Acknowledgments

I would like to take this opportunity to thank all those people who contributed to the completion of this work. First, I would like to gratefully acknowledge and extend my heartfelt gratitude to my Research Supervisor, **Dr.M.Farooq Mir** for introducing me into the field of High Energy Physics and providing me various opportunities to work in other collaborating centres. His constant guidance helped me a lot to finish this research work in time.

My regardful thanks are due to **Prof. Sheikh Javid Ahmad**, Head of Physics Department, University of Kashmir, and **Dr. Manzoor A. Malik**, acting H.O.D. Physics, for providing me with necessary infrastructure, help, support and other facilities during my tenure of research. I also extend my thanks to the whole teaching faculty of the department for their generous help whenever needed.

My sincere thanks to **Dr. Subhasis Chattopadhayay**, an eminent Scientist in experimental high energy physics, VECC, Kolkata for his valuable suggestions and timely help in the completion of my analysis work in appropriate time. My special thanks are also to our CBM Collaborators especially **Dr. Y.P. Viyogi**, **Dr. Zubyer** and **P.P.Bhaduri** from VECC, for their guidance and academic suggestions throughout my research period.

My sincere thanks to senior scholars and my friends Mr. Raja Nisar, Mr. Waheed Ahmad and Mr. Gowher Hussain for their timely suggestions. My special thanks to my friends Mr. Asif Iqbal, Mr. Mubashir Hamid, Mr. Waseem Raja, Mr. Firdous Ahmad, Mr. Asloob Ahmad and Miss Suraya for their help during the completion of my course work. Thanks are also due to research scholars Mr. Mukesh Sharma (JU), Mr. Kalyan Dey (GU), Mr. Arun Kumar (BHU), Miss Hushnud and Mr. Tariq (AMU) for their help, support, and good wishes.

I sincerely thank all the members of technical and non-technical/non-teaching staff of the department for their affection and kind co-operation.

I have no words to express my gratitude to my parents, brother, sister and close friends for bearing with me throughout my M. Phil. programme. I shall always remain indebted to them for their unstinted support, be it financially, morally or inspirationally.

Shabir Ahmad

Post Graduate Department of Physics, University of Kashmir, Srinagar.

Certificate

This is to certify that the dissertation entitled "***Study of the Observables of Highly Compressed Baryonic Matter Produced in Nucleus-Nucleus Collision in CBM Experiment at FAIR***" submitted by ***Shabir Ahmad***, in partial fulfillment for the award of the degree of ***Master of Philosophy*** in ***Physics***, is the original research work carried out by him under our supervision and guidance. It is further certified that the dissertation has not been submitted for the award of M. Phil. or any other degree to this University or any other University. The scholar has attended the department for statutory period as required under rules.

Dr. M. Farooq Mir
(*Supervisor*)

Dr. Manzoor A. Malik
(*Head of the department*)

Dedicated

to
My Parents

Contents

List of Figures

List of Tables

Chapter 1

Theoretical Overview

Until the beginning of the 20^{th} century, atoms were thought to be the fundamental indivisible building blocks of all forms of matter. In 1900's through the experiments of Rutherford- protons, neutrons and electrons came to be regarded as the fundamental particles of nature. In 1964, Gell-Mann and G.Zweig suggest that these particles are made up of quarks [1, 2] and in 1969, scientists got the evidence for existence of quarks [3]. The science of this study is called *Elementary Particle Physics* or sometimes *High Energy Physics (HEP)*. Figure 1.1 depicts the scale of particles.

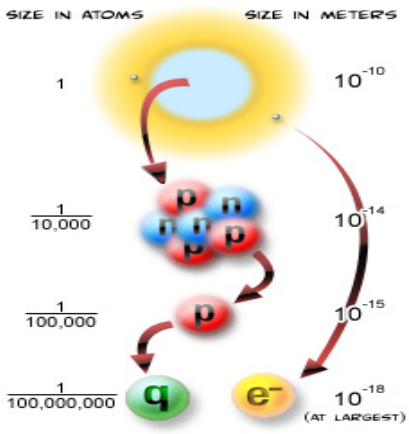

Figure 1.1: Scale of particle sizes

By the early 1960s, as after the invention of accelerators that accelerate protons or electrons to high energies and smash them(called relativistic collisions) into nuclei to produce new particles [4]. Hundreds of new particles were found. Could all of these then be the new fundamental particles? Confusion reigned until it became clear late in the last century, through a long series of experiments and theoretical studies, that there existed a very simple scheme of two basic sets of particles: the *quarks* and *leptons* and a set of *fundamental forces* transmitted through the exchange of particles called *gauge bosons*. *Standard Model* is the theory that describes the role of these fundamental particles and interactions between them [5]. And the role of particle physics is to test this model in all conceivable ways, seeking to discover whether *something more lies beyond it.*

In this unit we will give brief introduction of particle physics, relativistic heavy ion collisions, new state of deconfined quarks and gluons known as

FERMIONS matter constituents spin = 1/2, 3/2, 5/2, ...

Leptons spin = 1/2

Flavor	Mass GeV/c^2	Electric charge
ν_e electron neutrino	$<1\times10^{-8}$	0
e electron	0.000511	−1
ν_μ muon neutrino	<0.0002	0
μ muon	0.106	−1
ν_τ tau neutrino	<0.02	0
τ tau	1.7771	−1

Quarks spin = 1/2

Flavor	Approx. Mass GeV/c^2	Electric charge
u up	0.003	2/3
d down	0.006	−1/3
c charm	1.3	2/3
s strange	0.1	−1/3
t top	175	2/3
b bottom	4.3	−1/3

(a) fundamental fermions

BOSONS force carriers spin = 0, 1, 2, ...

Unified Electroweak spin = 1

Name	Mass GeV/c^2	Electric charge
γ photon	0	0
W^-	80.4	−1
W^+	80.4	+1
Z^0	91.187	0

Strong (color) spin = 1

Name	Mass GeV/c^2	Electric charge
g gluon	0	0

(b) intermediate gauge bosons

Figure 1.2: Properties of Fermions and Bosons

Quark Gluon Plasma(QGP) and finally Facility for Anti-proton and Ion Research(FAIR) at GSI, Germany.

1.1 Elementary Particles

According to highly successful mathematical theories of particles physics known as the *standard model*, formulated in 1970s, matter is built from a small number of fundamental spin 1/2 particles, or fermions: *six quarks (u,d,c,s,t,b)* and *six leptons*($e,\mu,\tau,\nu_e,\ \nu_\mu,\ \nu_\tau$) and integral spin particles called gauge bosons ($\gamma, W^\pm, Z^0, g$) as intermediators of interactions[6].

Six quarks are grouped into 3 pairs as shown figure 1.2a. Each quark comes in three colors; red, green, and blue. The quarks are peculiar as they posses a charge which is a fraction of that for the electron.

Quarks combine into particles called hadrons in two ways known as ; *(1)Baryon* which is a system of three quarks (e.g. *proton : uud*) and *(2)Meson*, a quark - anti-quark pair system (e.g. π *:* $u\bar{d}$). Baryons are usually confined within nuclei and are unstable if isolated, e.g. a neutron has a lifetime of about 15 minutes in free space. The exception to this is the proton which is essentially stable in free space. The common material of the present universe is constituted from stable particles, i.e. the electrons e and the u and d quarks. The heavier quarks *s, c, b, t* also combine to form particles akin to, but much heavier than, the proton and neutron, but these are unstable and decay rapidly (in typically 10^{-13} s) to *u, d* combinations, just as the heavy leptons decay to electrons.

Conservation of the leptonic numbers means leptons and anti-leptons must be created in pairs of a single generation. However, neutrino oscillations are known to violate the conservation of the individual leptonic numbers.

Table 1.1: Fundamental forces with their properties.

Force	**Relative Strength**	**Gauge Boson**	**Mass (rel. to proton)**	**Charge**	**Spin**
Strong	1	Gluon (g)	0	0	1
Electromagnetic	1/137	Photon(γ)	0	0	1
Weak	10^{-9}	$W^{\pm}$, Z	86, 97	± 1, 0	1
Gravity	10^{-38}	Graviton	0	0	2

There are four types of fundamental interactions or fields; Strong, Electromagnetic, Weak and Gravitational interaction. Strong force binds quarks together because quarks have color charge but protons and neutrons are color-neutral. It is the strong force between the quarks in one proton and the quarks in another proton which is strong enough to overwhelm the repulsive electromagnetic force. This is called the *residual strong interaction*, and it is what glues the nucleus together. The inter-quark force is mediated by a massless particle, the gluon.

Electromagnetic interactions are responsible for virtually all the phenomena in extra-nuclear physics, in particular for the bound states of electrons with nuclei, i.e. atoms and molecules, and for the intermolecular forces in liquids and solids. These interactions are mediated by photon exchange. Weak interactions are typified by the slow process of nuclear, β-decay, involving the emission by a radioactive nucleus of an electron and neutrino. The mediators of the weak interactions are the W^+, W^- and Z^0 bosons, with masses of order 100 times the proton mass. It is theoretically believed that the *Higgs boson* is responsible for the creation of mass through Higgs mechanism for $W^{\pm}$ and Z^0 [8]. Weak interactions are responsible for the decay of massive quarks and leptons into lighter quarks and leptons. It has to be noted that only left-handed fermions participate in the weak interaction, while there are no right-handed neutrinos. This is an example of *parity violation*. Gravitational interactions act between all types of particle. On the scale of experiments in particle physics, gravity is by far the weakest of all the fundamental interactions, although of course it is dominant on the scale of the universe. It is supposedly mediated by exchange of a spin 2 boson, the graviton. Experiments to detect gravitons (as gravitational waves) are currently under way. Figure 1.2b lists intermediate particles (bosons) with their properties. Table 1.1 presents some of the properties of these interactions.

In Standard model elementary fermions are grouped into three generations as shown in figure 1.3, each comprising two leptons and two quarks. All searches for a fourth generation of quarks and other elementary fermions have failed[9, 10] and there is strong indirect evidence that no more than three generations exist[11, 12, 13]. Particles in higher generations generally have greater mass and less stability, causing them to decay into lower-generation particles by means of

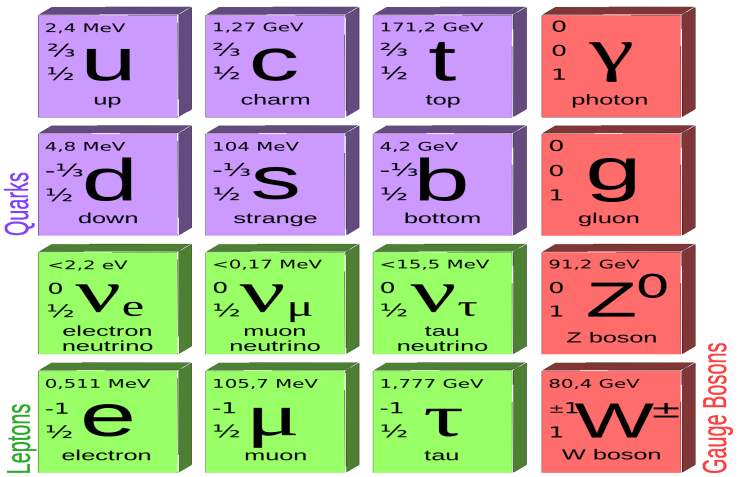

Figure 1.3: Standard Model[14]

weak interactions. Only first-generation (up and down) quarks occur commonly in nature. Heavier quarks can only be created in high-energy collisions (such as in those involving cosmic rays), and decay quickly; however, they are thought to have been present during the first fractions of a second after the Big Bang, when the universe was in an extremely hot and dense phase (the quark epoch). Studies of heavier quarks are conducted in artificially created conditions, such as in particle accelerators[15].

1.2 Quantum Chromo-Dynamics (QCD)

The field theory for the strong interaction, is formulated in the non-Abelian gauge theory with $SU(3)_c$ color symmetry and, is called quantum chromodynamics (QCD). The colors red, green, and blue are ascribed to quarks, and their opposites, minus-red, minus-green, and minus-blue, to anti-quarks. According to QCD, all combinations of quarks must contain equal mixtures of these imaginary colors so that they will cancel out one another, with the resulting particle having no net color. Color involves the exchange of massless particles called gluons among quarks. The coupling constant of QCD has conspicuous behavior for a variation of momentum transfer square Q^2. The strong coupling constant $\alpha_s(Q^2) = g_s/4\pi$ "runs" as Q^2 varies. So, physics of QCD can be divided into two regimes [7].

On one hand, $\alpha_s(Q^2)$ becomes small for large Q^2 region as realized in hard scattering such as deep inelastic scattering, where quarks and gluons behave as free particles, implied by the word "*asymptotic-freedom*", and in such regions the perturbation theory works well.

On the other hand, for small Q^2 region as realized in the static state of bound

quarks inside hadrons, $\alpha_s(Q^2)$ becomes large and in this region the perturbative treatment is not reliable, where quarks are confined inside hadrons (in color singlet states). This is called the "*confinement*" phase. Here the lattice QCD calculations are employed.

QCD must be the theory for describing the dynamics of quarks and gluons in all Q^2 regions from "asymptotic-freedom" to "confinement" phases[16] .

1.2.1 Confinement

Color confinement is the physics phenomenon that color charged particles (such as quarks) cannot be isolated singularly, and therefore cannot be directly observed [17] rather they clump together to form groups, or hadrons. The constituent quarks in a group cannot be separated from their parent hadron, and this is why quarks can never be studied or observed in any more direct way than at a hadron level [18].

As any two electrically-charged particles separate, the electric fields between them diminish quickly, allowing (for example) electrons to become unbound from atomic nuclei. However, as two quarks separate, the gluon fields form narrow tubes (or strings) of color charge, which tend to bring the quarks together as though they were some kind of rubber band. This is quite different in behavior from electrical charge. Because of this behavior, the color force experienced by the quarks in the direction to hold them together, remains constant, regardless of their distance from each other[19, 20].

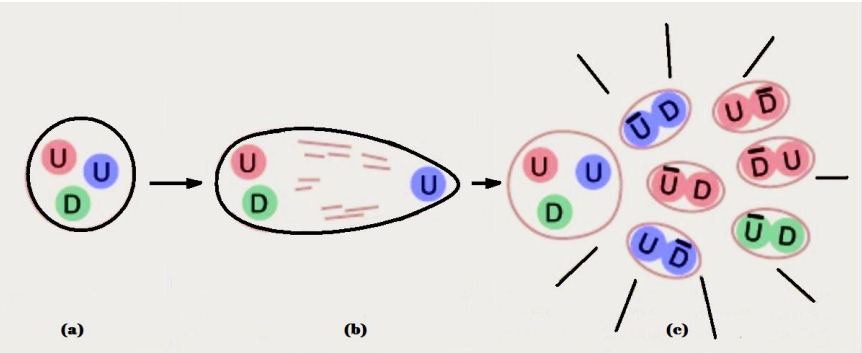

Figure 1.4: Quark confinement: (a) Quarks are free to move within the proton. (b) Energy required to pull quarks 1 fermi apart is of the order of 1 GeV, like stretching an elastic bag. (c) The energy required to isolated a quark far exceeds the pair production energy of a quark- antiquark pair, as a result producing mesons.

When two quarks become separated, as happens in particle accelerator collisions, at some point it is more energetically favorable for a new quark-antiquark pair to spontaneously appear, than to allow the tube (elastic bag) to extend

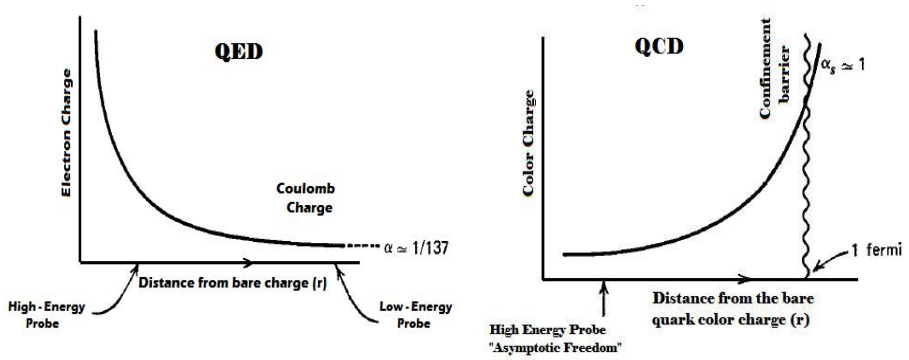

(a) (b)

Figure 1.5: (a)Screening of electric charge. (b) Screening of color charge

further as depicted by figure 1.4. As a result of this, when quarks are produced in particle accelerators, instead of seeing the individual quarks in detectors, scientists see "*jets*" of many color-neutral particles (mesons and baryons), clustered together. This process is called hadronization, fragmentation, or string breaking, and is one of the least understood processes in particle physics. It is a peculiarity of the strong forces between the quarks that they can be found only in combinations. So there is no way to observe the color of an individual quark. Inter-quark potential can be written as :

$$V = -\frac{\alpha_s}{4\pi r} + kr \tag{1.1}$$

where α_s is the strong coupling constant, k the string constant and r is inter-quark distance. It is clear from Eq. 1.1 that the strong coupling constant α_s tends to zero in such a manner so as to reduce the potential with decreasing distance.

1.2.2 Asymptotic freedom

Asymptotic freedom was discovered in 1973 by David Gross and Frank Wilczek, and by David Politzer and were awarded the Nobel Prize in Physics for this in 2004.

In QED, in the vicinity of a charge, the vacuum becomes polarized and virtual particles of opposing charge are attracted to the charge, and virtual particles of like charge are repelled. The net effect is to partially cancel out the field at any finite distance. Getting closer and closer to the central charge, one sees less and less of the effect of the vacuum, and the effective charge increases as depicted in figure 1.5a. This is known as charge "*screening*" effect.

In QCD, same thing happens with virtual quark-antiquark pairs; they tend to screen the color charge. However, each gluon carries both a color charge and an anti-color magnetic moment. The net effect of polarization of virtual gluons in the vacuum is not to screen the field, but to augment it and change its color. This is sometimes called "*antiscreening*". Getting closer to a quark diminishes the antiscreening effect of the surrounding virtual gluons, so the contribution of this effect would be to weaken the effective charge with decreasing distance as depicted in figure 1.5b.

It is obvious from the Eq. 1.1 that the quark-quark coupling strength, decreases for small values of r resulting from the penetration of the gluon cloud surrounding the quarks. The gluons carry "color charge" and therefore the penetration of the cloud would reduce the effective color charge of the quark known as "color screening" [5].

Strong force coupling constant α_s depends upon the wavelength of the quark as expressed as:

$$\alpha_s(E) = \frac{12\pi}{(33 - 2n_f)ln(\frac{E^2}{\Lambda^2})} \tag{1.2}$$

Where n_f is number of quarks active in pair production. Λ is wavelength of quark and experimentally determined value ≈ 0.2 GeV. Eq. 1.2 gives value of $\alpha_s \approx 1$ at the radius of a proton, this is the conventional value used to describe the strength of strong interaction within nuclei. When the proton is penetrated at a radius corresponding to an energy of 1 TeV, α_s is down to ≈ 0.1 which corresponds to asymptotic freedom[21].

1.3 Quark Gluon Plasma

As it is clear from the previous section that increasing the density of color charge reduces screening radius (r_D) and once the density of color charge is sufficient to make $r_D \lesssim r_H$(hadron radius), we expect for strongly interacting matter a transition from colour insulator (hadronic matter) to color conductor known as quark-gluon plasma (QGP).

A conduction electron in a metal generally has a different effective mass than that of an electron in vacuum or bound in an isolated hydrogen atom. This shift in mass is a collective effect due to the lattice and the other electrons in the conductor. Similarly, we expect that the quarks inside a hadron will have a different effective mass than they have in a plasma at high density. For the latter, asymptotic freedom leads eventually to a vanishing quark mass, while inside hadrons we have constituent quarks of effective mass $m_q^{eff} \approx 300$ MeV. A theory with massless quarks is chirally symmetric. At low density, this symmetry must thus be spontaneously broken; at high density, when $m_q^{eff} \to 0$,

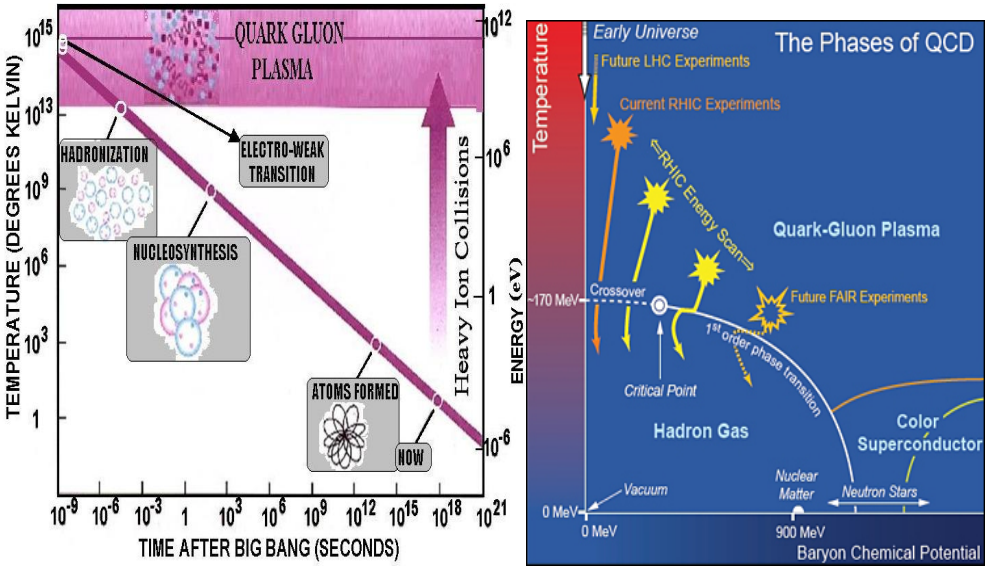

(a) (b)

Figure 1.6: **(a)**The transition from the primordial plasma of quarks and gluons to ordinary matter occurred some $10^{-5}s$ after the Big Bang when the temperature lowered to about $10^{12}K$. The inverse process is expected to occur nowadays at RHIC, LHC etc.**(b)** QCD phase diagram

chiral symmetry is restored [22, 23]. So, dense and hot medium entails a decrease in the mass value of vector mesons $(\rho, \omega, \phi, ..)$, may be accompanied by an increase in the width of the resonance peak[27].

QGP is supposed to be the primordial soup that originated the hadronic matter a few microseconds after the Big Bang, in the process of hadro-synthesis, as shown in the figure 1.6a. A dense state of matter is thought to exist also in the interior of Neutron stars [24].

Following the lattice-QCD predictions, the diagram for the envisaged phases of nuclear matter is shown in figure 1.6b. Computations with *three dynamical light quark flavours* on the lattice [26] revealed interesting insights into the behaviour of the hadronic matter under extreme conditions of density and indicated that a phase transition from a hadronic gas to a plasma of quarks and gluons(QGP), within which colour freely propagates, is expected at low quark chemical potential and at a temperature of $T_c \sim 170$ MeV which corresponds to an energy density $\epsilon_c = 0.6\ GeV/fm^3$. Colour superconductivity [25] and Color Flavor Locked (CFL) phase is expected at large baryonic chemical potentials and small temperature [27].

Heavy ion collisions are used, to generate high temperature and energy density, to recreate conditions that existed immediately after the Big Bang (a project affectionately known as the "Little Bang").

The *CERN* lead beam programme was opened in 1994. Seven large experiments were involved, measuring different aspects of lead-lead and also lead-gold collisions. They were code-named *NA44*, *NA45*, *NA49*, *NA50*, *NA52*, *NA57* and *WA98*. Modern Experiments to Study the QGP are *LHC* (Large Hadron Collider), *RHIC* (Relativistic Heavy Ion Collider) at Brookhaven, future *FAIR -CBM* Experiment at GSI Germany and so on..

1.4 Signatures of QGP

The problem is that the physicists can only see the particles that escape from the fireball and reach their detectors. From these signals they have to reconstruct what happened before, to work out whether the quarks and gluons were produced in a dense enough state to form a free plasma. QGP if formed will be of small size (5-10fm/c) and small life time ($\approx 10^{-23} sec$). The experiments were all optimised for measuring different signals which might indicate if and how a quark-gluon plasma was formed. Most prominent and theoretically predicted signatures are briefly discussed in following subsections.

1.4.1 Direct Photon Production

The only way to "see" the quarks directly is to detect the electromagnetic radiation which they emit in the form of photons. Quark pairs interact via real or virtual photon in QGP. Real photons have long mean free path because they interact via electro-magnetic interaction so they escape cleanly from the QGP to carry the information about the temperature of the state. Virtual photon decays via dilepton which carry the same message as that by the direct photon. There are two main processes of direct photon production in QGP:

1. *Annihilation Process:* The annihilation process involves the production of the gluon along with one γ

$$q \ + \ \bar{q} \ \longrightarrow \ \gamma \ + \ g \tag{1.3}$$

2. *Compton Process:* This process involves the scattering of a gluon off a quark (or antiquark).

$$g \ + \ q(\bar{q}) \ \longrightarrow \ \gamma \ + \ q(\bar{q}) \tag{1.4}$$

There are many other processes which can also produce photons called background noise. There are *hadronic processes* that mimic direct photon production in a QGP. One such set of processes is pion interactions as :

- *Pion Annihilation*

$$\pi^+ \quad + \quad \pi^- \quad \longrightarrow \quad \gamma \quad + \quad \rho^0 \tag{1.5}$$

- *Charged pion interaction with neutral pion*

$$\pi^\pm \quad + \quad \pi^0 \quad \longrightarrow \quad \gamma \quad + \quad \rho^\pm \tag{1.6}$$

- *Pion interaction with ρ mesons*

$$\pi^\pm \quad + \quad \rho^0 \quad \longrightarrow \quad \gamma \quad + \quad \pi^\pm \tag{1.7}$$

$$\pi^\pm \quad + \quad \rho^\mp \quad \longrightarrow \quad \gamma \quad + \quad \pi^0 \tag{1.8}$$

$$\pi^0 \quad + \quad \rho^\pm \quad \longrightarrow \quad \gamma \quad + \quad \pi^\pm \tag{1.9}$$

Since the hadronic interactions occur at a lower temperature than those found in a quark-gluon plasma, momentum distribution of the photons will reflect this. Momentum distributions of the quarks and anti-quarks will then tell us about the thermodynamical state of the QGP [23]. If QGP is formed then clear signals of photons from plasma could be visible by examining the photons with p_T range 2-3 GeV/c [28, 29].

1.4.2 Dilepton Production

In QGP, a quark q and an antiquark $\bar{q}$ can interact to form a virtual photon γ^*, which subsequently decays into a lepton l^- and an anti-lepton l^+ (a dilepton pair) as shown in figure 1.7.

After these dileptons form, they must pass through the collision region to the particle detectors. Since they interact only through the electromagnetic force, their free mean path is quite large. That means that the leptons are not likely to suffer further collisions after they are produced. On the other hand, the production rate and momentum distribution of the produced dilepton pair depends on the momentum distribution of the quarks and anti-quarks in the plasma, which is governed by the thermodynamic condition of the plasma. Therefore, the dilepton pairs carry information on the thermodynamical state of the medium at the moment of their production. One can conceivably use this to view the initial state of the collision [23] . One of the prominent decay channel of $q\bar{q}$ interaction is :

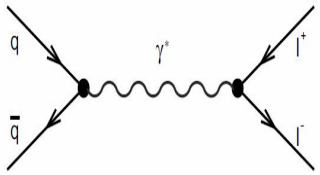

Figure 1.7: Reaction $q\bar{q} \longrightarrow l^- l^-$ in quark gluon plasma

$$q\bar{q} \quad \longrightarrow \quad \mu^+\mu^- \quad (Signal) \tag{1.10}$$

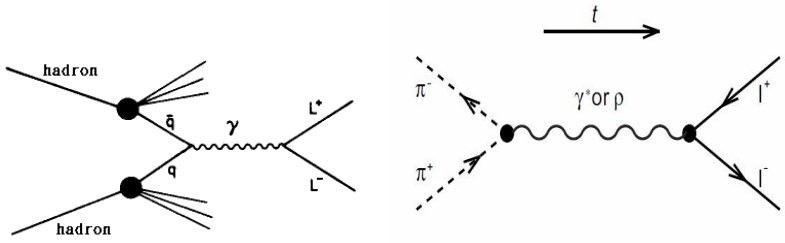

(a) Drell Yan Process (b) $\pi^+\pi^-$ annihilation

Figure 1.8: Dileptonic background

There are hadronic processes which could serve as background by increasing the dilepton yield. Important contributions include:

- **Drell-Yan Process:** The process caused by sea quarks, hadrons, and resonances, which produces a dilepton pair. A valence quark of a nucleon of one nucleus can interact with an antiquark of a nucleon of another nucleus [30]. They annihilate to form a virtual photon, which subsequently decays into a dilepton pair as shown in figure 1.8a.
- $\pi^+\pi^-$ **annihilation** and decay of hadron resonances (ρ, ω, ϕ and J/ψ) as shown in figure 1.8b.

The number of l^+l^- pairs from the Drell-Yan process for central collisions of two equal size nuclei scales as $A^{4/3}$. These pairs play important role as a background process on the upper edge of the low dimuon invariant mass region (about 1.5 GeV) [23]. One of the representative noise reaction can be given as:

$$\eta^+\pi^- \quad \longrightarrow \quad \mu^+\mu^- \quad (Background\ noise) \tag{1.11}$$

It has been suggested that a window for observing dileptons from the plasma phase exists in the invariant mass region between the ϕ and J/ψ [31]. Above the J/ψ mass, dominant contributions are from the Drell-Yan process and direct charm decay [32, 33], while below the ρ meson mass, radiative and direct decays, together with $\pi\pi$ annihilation, form the most important sources [34, 35, 36].

1.4.3 J/ψ Suppression

The J/ψ meson is the bound state of a charm quark c and a charm antiquark $\bar{c}$. Actually J/ψ, $\psi^{'}$, and $\chi_c(\chi_{c0}, \chi_{c1}$, and $\chi_{c2})$ are respective 1s ,2s, and 3p bound states of the c and $\bar{c}$. The radius of the bound state is the size of the J/ψ and is given by $r_{J/\psi} = \frac{1}{2m_c}$, where m_c= 1.5 GeV/c^2 is the mass of the charm quark. Since $r_{J/\psi} \simeq 0.20$ fm is so small, the bound state is tightly bound and hard to

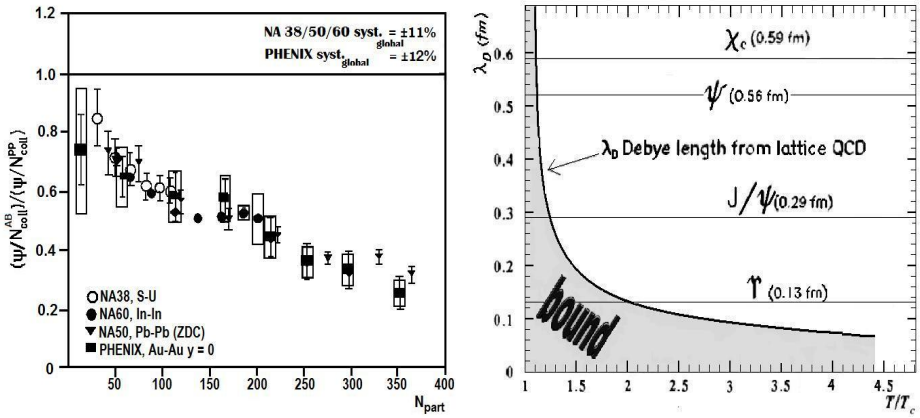

(a) J/ψ suppression at RHIC (b) Quarkonium bound state threshold

Figure 1.9: (a) J/ψ suppression in lead-lead (Pb-Pb) collisions at the SPS ($\sqrt{S_{NN}} = 17GeV$ and in gold-gold (Au-Au) at RHIC as a function of the reaction centrality (the number of participant nucleons). (b) Debye length as a function of the ratio between the melting temperature and the transition temperature. Small-size quarkonia break up at lower temperature.

break apart. If the J/ψ were broken apart, the charm quark would combine with an up or down antiquark to form a D^0(cu) or a D^+(cd) respectively and the charm antiquark would combine with an up or down quark to form a $\bar{D}^0$($\bar{c}$u) or a D^-($\bar{c}$d) respectively. Thus the binding energy of the J/ψ is:

$$\epsilon_{J/\psi} = m_{D\bar{D}} - m_{J/\psi} = 634 \;\; MeV \tag{1.12}$$

The combination of a large binding energy and small size makes the J/ψ hard to break apart. This long lived bound state of heavy quarks ($J/\psi, \chi, \psi', \Upsilon$) mainly originate from *gluon-gluon fusion*, generating either a c-$\bar{c}$ or a b-$\bar{b}$ pair that becomes a bound state at very early times in the collision, when the temperature is still a above the charm or bottom production threshold.

In 1986, Helmut Satz of Bielefeld University, together with Tetsuo Matsui [37], predicted that deconfinement would be signalled by the melting of heavy quarkonium states if the temperature of the formation of the QGP is greater than a critical deconfinement temperature T_c, there should be a distance *Debye colour screening*(λ_D) such that, for distances greater than λ_D the strong (colour) forces that bind the c-$\bar{c}$ or the b-$\bar{b}$ pair together become screened and therefore no bound state will be formed. J/ψ production suppressed due to color screening in QGP is recorded at small p_T(Transverse momentum) $\lesssim 1$ GeV.

Shortly after the initial proposal of J/ψ suppression as a signal of deconfine-

ment [37] in 1986, the NA38 Collaboration at CERN observed a suppression of J/ψ production relative to the dimuon continuum [38] in central collisions of ^{16}O projectiles on an ^{238}U target at 200 A GeV/c. NA38 actually measured the $N_{J/\psi}/N_{cont}$ and saw a decrease as predicted by Matsui and Satz. ($N_{J/\psi}$ is the number of dimuons with an invariant mass near the J/ψ mass and N_{cont} is the number of dimuons with an invariant mass away from the J/ψ mass). However to conclude with certainty that this indicates a QGP means that hadronic scenarios must be ruled out. J/ψ suppression concluded at RHIC is depicted in figure 1.9a.

Figure 1.9b shows how bound states with larger size (or equivalently less tight) first disappear, ones with smaller size disappear at higher T. The Υ ground state melts at a temperature around two times the transition temperature.

J/ψ has large branching ratios (6%) for decay into dileptons for both di-electrons($J/\psi \rightarrow e^- e^+$) and dimuons ($J/\psi \rightarrow \mu^- \mu^+$). The muons are heavier and thus almost go straight through matter. The signal to background ratio will be high for the muons, which makes them "*clean*" signal in the experiment. Dileptons carry the information about the J/ψ in the form of their invariant mass, m_{inv}, which for a lepton pair is given by:

$$m_{inv} = \sqrt{(E_1 + E_2)^2 - (\vec{P}_1 + \vec{P}_2)^2} \quad (for\ lepton\ pair) \tag{1.13}$$

Experimentally, J/ψ production is identified by the peak in the invariant mass distribution of lepton pairs for the value **3.1 GeV**.

There are other possible backgrounds that may mask a J/ψ suppression by giving a large contribution in the J/ψ region of the dilepton invariant mass spectrum. These processes include the *Drell-Yan (DY) process* and open charm (*D meson*) decay.

1.4.4 Low Mass Vector Meson Production

Low Mass Vector(LMV) mesons i.e ρ, ω, and ϕ represents an effective probe of QGP formation since their properties such as mass, width, and branching ratios are expected to be sensitive to strong *in-medium effects* and to changes in the quark masses, if *chiral symmetry* were partially restored. Like the J/ψ, they can decay into lepton pairs (for example an electron and a positron, or a muon and an anti-muon). If we draw a graph of the number of lepton pairs we see at different lepton pair masses, we end up with a peak for each different kind of vector meson. Usually the ρ form a wide peak, with a sharp peak from the ω meson on top. But in high energy collisions we see no ρ peak at all, only a broad smear. What the physicists think is happening here is that the ρ's are

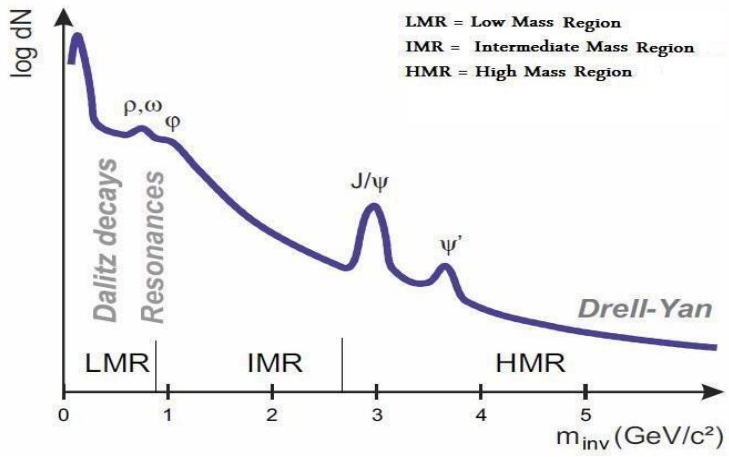

Figure 1.10: Invariant mass of lepton pairs

being formed and decay while the hadrons are still interacting with each other. The short time between collisions does not give them a chance to develop into a state with a well-defined mass, hence the smearing. In other words, the graph acts as a snapshot of the collision stage directly after the liberated quarks have condensed, but well before the hadrons have stopped interacting.

At larger invariant mass region there are two peaks at 3.1 GeV/c^2 and 3.7 GeV/c^2 caused by decays of J/ψ and ψ'-resonances as shown in figure 1.10. Further resonances are observed in the region of invariant masses smaller than 1 GeV/c^2 (low mass region, LMR) from the decay of ρ, ω, and ϕ -mesons. At even smaller masses the dileptons spectrum is dominated by *Dalitz* decays of π^0, η, η', and ω.

1.4.5 Strangeness Enhancement

Strangeness content is enhanced in hadron matter as the temperature increases, but the strangeness is enhanced to an even greater extent in a quark-gluon plasma [43]. For proton-proton or electron-positron collisions, the fraction of extra strange quarks made is **0.2** and remains the same even with increase the energy. But for the nucleus-nucleus collisions, the fraction is twice as high, at **0.4**. Thus we say "*global strangeness enhancement by a factor of two*" [44]. The point is that we know from detailed calculations that once hadrons have been formed, essentially no more strange quarks can be made. So most of these extra strange quarks must have been created before the hadrons were made, i.e. in a quark-gluon plasma.

Among particle species, strange particles freeze-out (chemically) at the early stage of system evolution, interacts with quarks of different flavour and eventually appear as a strange hadron in the final state. They provide information

on the high density stage of the collision, being the strangeness affected only by the annihilation process $s(\bar{s})$ that goes into $q(\bar{q})$ which happens in reactions of this type: $\Lambda + K^+ \longrightarrow n + \pi^+$.

The chemical equilibrium is expected to proceed much faster in the QGP rather than by rescattering in a hadron gas as a result of the equilibration of strange and light quark flavours. In fact, light hyperons, like the $\Lambda(uds)$, with a mass of 1115 MeV, are produced copiously than heavier hyperons like $\Xi(qss)$ with a mass 1315 MeV and $\Omega(sss)$ with a mass of 1672 MeV and their respective anti-particles due to higher threshold. So, in dense nuclear matter, the chemical equilibration times of strange quarks, through gluon fusion and light quark annihilation mechanism, will be very fast, of the order of 5-6 fm/c, which corresponds to the lifetime of QGP. Production of anti-hyperons is unlikely because incoming beam particles requires interactions involving anti-nucleons. The different behaviour of multi-strange anti-baryons in QGP *vs.* hadron gas is therefore a strong probe.

In hadronic matter, the ratio of $s\bar{s}$ pair production to non-strange $q\bar{q}$ pair production is about 0.1 ($q\bar{q}$ represents $u\bar{u}$ and $d\bar{d}$). One way to gauge an increase in the $(s\bar{s})/(u\bar{u})(d\bar{d})$ ratio is to measure the K^+/π^+ ratio, especially because the produced hadrons in the collisions consist mostly of pions and kaons. As the temperature of a hadron gas in thermal and chemical equilibrium increases, the pion and kaon densities rise as well. However, the kaon density increases at a rate faster than the pion density. Thus, some of the increase of the K^+/π^+ can be explained in a hadronic scenario. Thermal equilibrium is achieved when the momentum distributions of the particles reach a dynamic equilibrium.

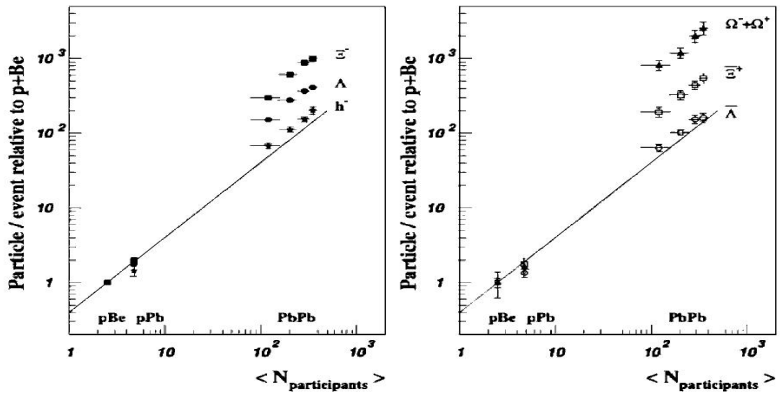

Figure 1.11: Strange particle production in Pb-Pb, p-Pb and p-Be as measured at the NA57 experiment at SPS. Hyperon and anti-hyperon yields as a function of participant nucleons, normalized to the corresponding yield in p-Be collisions.

In measurement of the WA97 Collaboration [38], the production of multi-

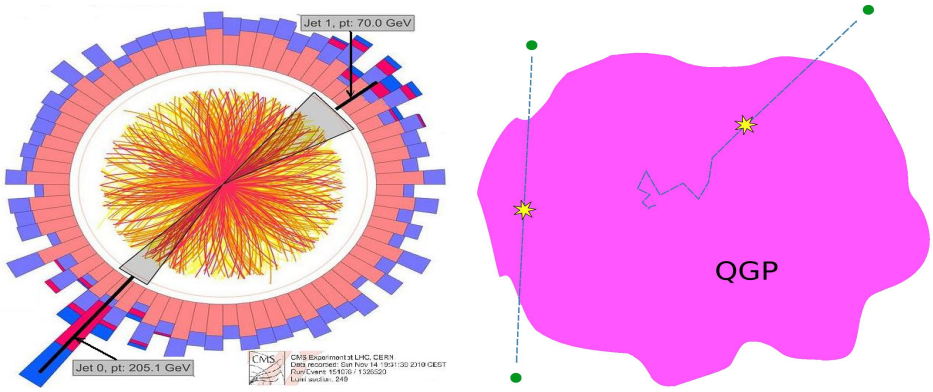

(a) Jet Quenching at CMS (b) Jet Quenching process

Figure 1.12: (a)Jet Quenching at CMS Experiment at RHIC (Copyright CERN). (b) Jet Quenching Mechanism inside QGP

strange hyperons is found to be substantially enhanced. In particular, the production of $\Omega^- + \bar{\Omega}^+$ in Pb+Pb collisions at 158A GeV is enhanced by up to a factor of 15 relative to that of p+Be. Figure 1.11 shows the enhancement in hyperon and anti-hyperon yields in NA57 experiment at SPS.

1.4.6 Jet Quenching

Jet Quenching is one of the signature of quark gluon plasma phase transition [45, 46, 49]. The event, shown in figure 1.12a, in the first lead-ion run of the LHC has two nearly back-to-back jets of particles from a single event. Their momenta should have about the same magnitude (by conservation laws) but the jet at the top right falls well short of the jet at the bottom left. The jet on the right seems to have interacted with the quark-gluon plasma and transferred some of its initial momentum to the particles which make up the plasma, resulting in a lower momentum measured in the calorimeter. This is "*jet-quenching*" [48]. When strongly interacting particle pairs (normally quarks, or possibly gluons) are produced at high momentum in the QGP, it is possible that one of the particles will lose energy in flight through the plasma and will not be detected, whereas the other particle will escape easily, as depicted in figure 1.12b.

Figure 1.12b shows two possible pair-production scenarios in the quark-gluon plasma. On the left, a particle antiparticle pair is produced having momentum roughly parallel to the nearest surface of the plasma, and therefore both particle and antiparticle escape without experiencing much drag. On the right, a particle-antiparticle pair is produced with momentum roughly normal to the surface, with the result that one particle escapes easily, but the other heads into the dense inner region of the plasma and loses much of its energy, probably

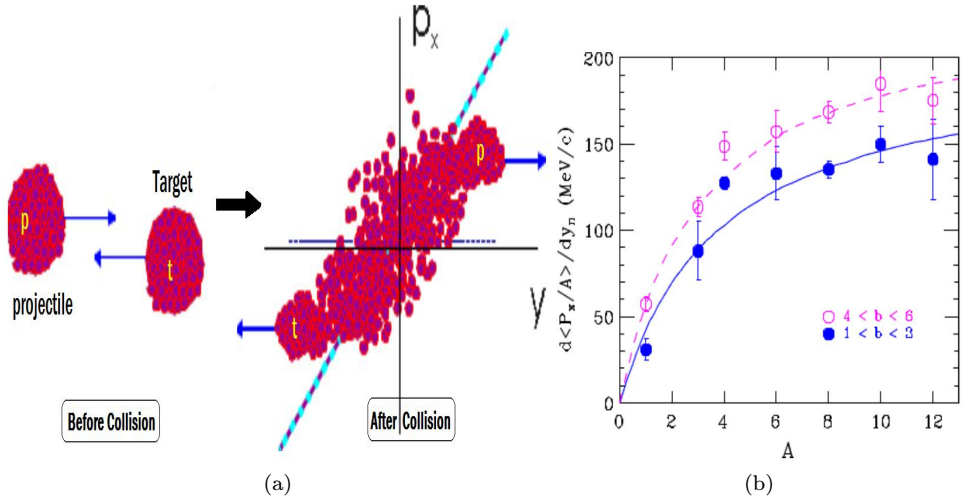

(a) (b)

Figure 1.13: (a) Distribution of nuclear matter before and after collision.(b) Sideward flow increase with fragment mass.

never making it out to any detector. Thus Jet Quenching could show up as a depletion in the yield of p_T hadrons making it a potential probe for the study of a high density deconfined phase transition [49, 50, 51].

1.4.7 Collective Flow

Collective flow is an important observable, being sensitive to the effective degrees of freedom in relativistic heavy ion collisions. Information about the Equation of State(EoS) can be extracted from the collective flow of nuclear matter deflected sidewards from the hot and dense region formed by the overlap of projectile and target nuclei. This flow reflects collective properties of the medium. In the hydrodynamical picture, the pressure gradient generates the collective flow. The schematic diagram in Fig. 1.13a illustrates the nuclear matter distributions for the projectile and target nuclei before the collision and a *sidewards deflection* of the nuclear matter after the collision which is frequently termed "*sidewards collective flow*". This flow reflects the interplay of collective and random motions. For a thermalized system, the random motions of emitted fragments are dictated by the thermal energy, which is independent of mass. Contributions to the fragment energy due to collective motion, on the other hand, increase linearly with mass, making the flow more easily observed for heavier fragments. The Fig. 1.13b illustrates how the sidewards flow increases with fragment mass (A). Model calculations denoted by the curves in the figure imply that the fragment flow provides an excellent indication of the underlying flow of nuclear matter and pressure that drives this flow. Comparisons between the flow for different projectile and target nuclei and different incident energies now permit

determinations of the incompressibility of nuclear matter.

In the almond shaped region of a non-central collision (with impact parameter b >0), the pressure gradient is expected to be larger in the direction of the impact parameter. Thus, the particle production will have an *elliptical* azimuthal distribution characterized by the second fourier coefficient (**v2**) of a fourier decomposition of these angular distributions. Since the pressure gradient is closely related to the EoS, it is important to measure the **elliptic flow** in order to detect the existence of the QGP pressure in the early stage. If the phase transition is of first order, the pressure remains constant during the phase transition. This results in a vanishing sound velocity, $c_s = \sqrt{\partial P/\partial \varepsilon}$, which is referred to as "*softening of the EoS*". The collective expansion velocity will be reduced significantly if softening occurs and the study of collective motion in the final state of the produced hadrons is expected to provide key information about the EoS [52].

1.4.8 Fluctuations

Several thermodynamic quantities show varying fluctuation patterns when the system undergoes a phase transition from hadronic matter to quark-gluon plasma (QGP). Event-by-event fluctuations of thermodynamic are used to study the nature of the QGP phase transition in the laboratory [53]. Large fluctuations in energy density are expected if the phase transition is of first order whereas specific heat diverges at second order phase transition. Furthermore, near the critical point of the QGP phase transition, fluctuations are predicted to be largely enhanced [54]. Fluctuations of *conserved quantities* like electric charge, baryon number or strangeness are predicted to be significantly reduced in a QGP scenario as they are generated in the early plasma stage of the system created in heavy-ion collisions with quark and gluon degrees of freedom [55, 56]. The fluctuation generated at the QGP stage will increase as the system evolves in time [57, 58]. Fluctuations usually studied in heavy ion collisions are:

- **Net charge fluctuations:** Net charge fluctuations have been measured by experiments at SPS and RHIC using different fluctuation measures.
- **Multiplicity fluctuations:** Multiplicity of produced particles characterizes the evolving system in a heavy-ion collision and its fluctuations is distinct signal of the QGP phase transition [53, 55].
- **Particle fluctuations:** Relative production of different types of particles produced in the hot and dense matter might be affected once the system goes through a phase transition. Of particular interest is the strangeness fluctuation in terms of the ratio of kaons to pions. Large broadening in the

yields of kaons to pions has long been predicted because of the differences in free enthalpy of the hadronic and QGP phase. This could be probed through the fluctuation in the K/π ratio.

- $< p_T >$ **fluctuations:** The $< p_T >$ of emitted particles in an event is related to the temperature of the system. Thus the event-by-event fluctuations of average p_T is sensitive to the temperature fluctuations predicted for the QGP phase transition $< p_T >$ can be measured experimentally with high precision.

1.5 Chiral Symmetry Restoration

Besides confinement, QCD has another important property, which is associated to the fact that the masses of the u- and d-quarks are small compared to the relevant scales of QCD. Thus, these masses can be taken as zero for many practical applications. The theory assumes that a massless quark with its spin pointing into the direction of the momentum preserves its helicity for all times in spite of the interaction with other quarks and likewise for a mass-less quark with its spin opposite to the direction of motion. This symmetry is called *chiral symmetry* because the conserved spin alignment with the quark's direction of motion can be associated with the right-, respectively left-handedness. They are so-called chiral partners under parity transformation. Chiral symmetry predicts for every particle the existence of a mirror reflected particle with same properties such as the mass. Hence, the spectrum of hadrons should group into parity partners with identical properties. This, however, is not observed in nature. Actually, the parity partners exhibit large differences in their masses. Hence, in nature chiral symmetry is observed to be *spontaneously broken*. If chiral symmetry is spontaneously broken, zero mass excitation modes have to exist. These particles, the so-called *Goldstone bosons*, can be associated with the pions. Their small masses (on the scale of hadron masses) are an indication of "*leftovers*" of chiral symmetry. Pions are the lightest hadrons and they indeed have proper chiral properties. Their masses are not quite vanishing which results from the small but finite masses of the u- and d-quarks. These finite masses explicitly break chiral symmetry just like an externally applied magnetic field breaks the spin symmetry in a ferromagnet. The concept of chiral symmetry has turned out to be very powerful for the understanding and interpretation of the light hadrons and their structure.

At high temperatures and/or densities a transition to the chirally restored phase is expected. This fact would imply dramatic changes in the properties of certain hadrons in the medium in the vicinity of the phase transition. In the

chirally restored phase each particle and its parity partner have to become alike. In particular, their masses have to become similar.

1.6 Relativistic Heavy Ion Collisions

Based on the two scenarios like high T(temperature) and high ρ(density), we expect QGPs in three places: (i) in the early Universe (ii) at the center of compact stars and (iii) in the initial stage of colliding heavy nuclei at high energies. The last possibility, which is currently being experimentally pursued. The different energy ranges involve different collision processes and physical phenomenon and these ranges are divided into three regions:

- *Intermediate heavy-ion collisions* (beam energy: 10 - 100 A MeV)
- *Relativistic heavy-ion collisions* (beam energy: 100 A MeV - 10 A GeV)
- *Ultra - relativistic heavy ion collisions* (beam energy: 10 A GeV onwards)

Ordinary nuclei are located in a region defined by a temperature much smaller than the proton and pion rest masses and a baryon density of about 0.14 nucleons/fm^3 corresponding to an energy density of 130 MeV/fm^3. This means that distances between nucleons are larger than their radius (≈ 0.8 fm), whereas the transformation of ordinary matter into QGP requires that the nucleon wave functions significantly overlap each other, condition likely reachable by smashing together, at relativistic energies, heavy nuclei. An energy density many times higher than that of ordinary nuclear matter is achieved so that nucleons loose their identity by melting into a soup of quarks and gluons through a process that reverses the early universe history.

Although the energy densities achieved in collision $e^+ - e^-$ or $p - p$ could be as high as in colliding heavy nuclei but overall size of the *interaction region is too small* to study the effects of deconfinement. Moreover, because of the short range of the strong interactions and subsequent evolution of the QGP, the relevant experimental observables come mainly from the interior of the dense energy region whilst background is essentially originated on the surface. Consequently the *signal over background ratio is proportional to the colliding object's volume over surface ratio*, thus favouring heavy nuclei collisions.

In high energy nucleus-nucleus collisions, nucleons are excited to short-lived states (baryon resonance), which decay by the emission of mesons. At higher temperatures also baryon-anti-baryon pairs can be created. This *mixture of mesons, baryons and anti-baryons is generally called* ***hadronic matter*** (occurs at high temperature), or ***baryonic matter*** *if baryons preponderate* (occurs at

high density). In accordance with QCD the strong force weakens with increasing energy and at sufficiently high temperatures and/or densities the hadrons overlap, and the partons may move freely forming the QGP state within which partons move freely.

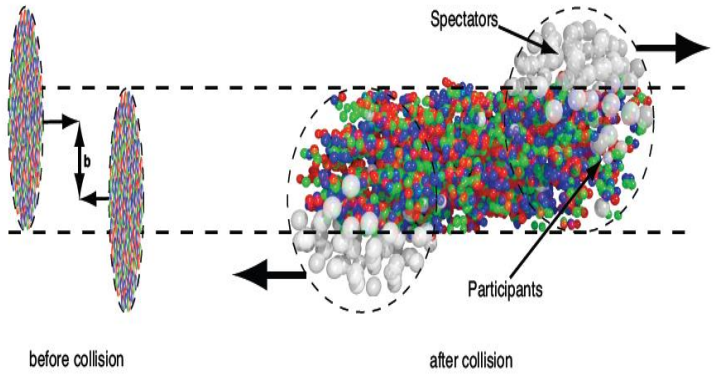

Figure 1.14: Relativistic Heavy ion Collision scenario for b>0

In Nucleus-Nucleus Collision the parts of the two nuclei which overlap/collide form the so-called *participant* region while the rest of the nuclei is called the *spectator* region as depicted in Fig. 1.14. At relativistic energies, the spectator parts of the nuclei move apart and fragment in a very narrow cone around their original direction. Properties of the created system are determined by the centrality of the collision which is described interms of impact parameter b (distance between the centers of two colliding nuclei). Central collision events ($b \sim 0$) are the best candidate for searching QGP because grazing or peripheral collisions at large b do not provide the geometrical overlap of enough nucleons mandatory to achieve a high energy density in a large volume [27].

One of the main goals of the heavy ion collision experiments at RHIC and LHC and future FAIR energies is the study of *quark gluon plasma* and the nuclear matter *phase diagram*.

1.6.1 Space Time Evolution

The space-time evolution of the system formed in the heavy-ion collisions is shown in Fig. 1.15. In high energy heavy ion collisions two accelerated nuclei approach each other with relativistic velocities and thus are lorentz contracted.

After the initial collision phase, two scenario are possible. First is formation of a hadron(mostly pion) gas, followed by freezout, linked to a superposition of many binary collisions of nucleons. In second scenario, the initial stage would be followed by an equilibrated plasma state, gradually becoming a mixed phase

of partons and hadrons as the plasma cools then chemical freezout of particles occur to form hadron gas and finally kinetic freezout occur as depicted by Fig. 1.16 and Fig. 1.15.

The participant region has a very different behaviour which is schematically illustrated in Fig. 1.16. There is not a clear delimitation for the steps in the evolution of the participant region from a nuclear collision but the figure gives at least a temporal hierarchy.

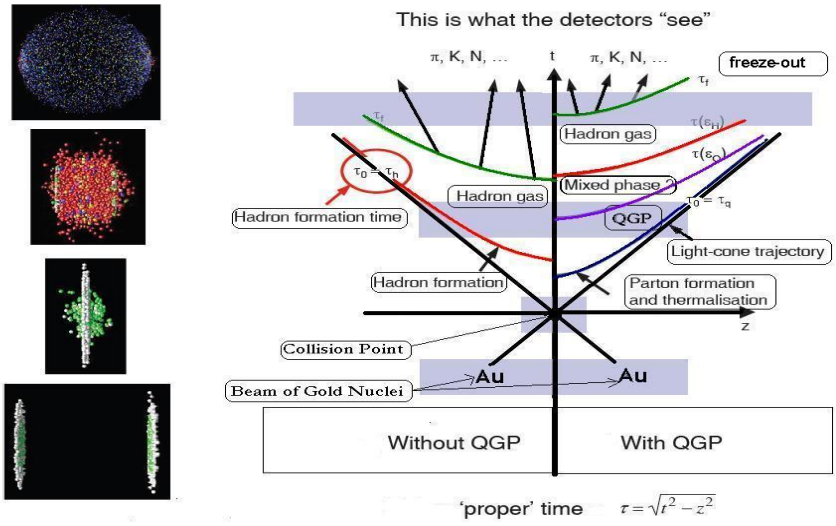

Figure 1.15: Space-time diagram of the evolution of an ultra-relativistic nuclear collision as viewed in the nucleon-nucleon center-of-mass system.

After the "*formation time*" (about 1 fm/c), quarks and gluons materialize out of the highly excited colour field and *thermal equilibrium* is approached via reaction between individual pairs leading to the creation of the so-called "*fireball*". At this point the system expands rapidly, mainly along the longitudinal direction, and cools down thus reaching the transition temperature T_c for the creation of QGP. If there is QGP formation and the system is in equilibrium state, then thermodynamics can be used to describe the system. In the subsequent mixed phase, hadronization starts in the "fireball" that still expands, likely in an ordered motion (large outward flow) through a hadron gas phase until the "*freeze out*" is achieved when interactions cease and particles freely leave the reaction region and eventually can be detected by the experimental instrumentation. Then associated signals with each phase are observed by experiments.

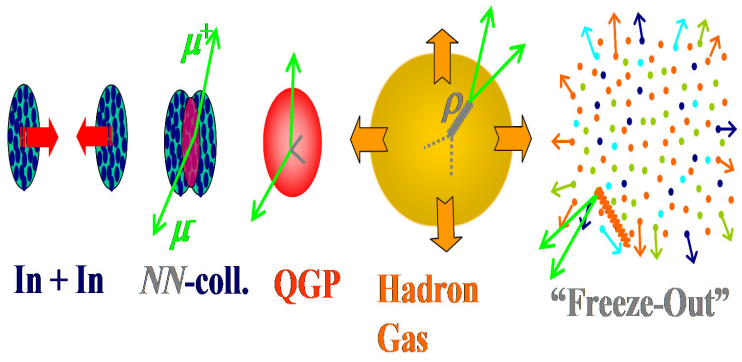

Figure 1.16: Time evolution of nuclear collisions

In ultra-relativistic nuclear collisions, baryons appear in the centre-of-mass, predominantly at the rapidities of the initial beams, while *in the central rapidity region one expects the bulk of created particles.*

As already mentioned, according to theoretical predictions, QGP may occur at about (0.6-1.0) GeV/fm^3 [27, 59](which is about 5-10 times the nucleus density) and temperature above $T_c \approx 170MeV$ [60]. The attained energy density ϵ, defined as the amount of the energy made available in the collision in the volume of interaction region, is experimentally estimated from the following equation based on Bjorken's model [61].

$$\epsilon = (\text{particle's average energy} \times \text{number of particles})/(\text{interaction volume})$$
$$= (1/c\tau_0\pi {r_0}^2 {A_P}^{2/3}).\frac{dE_T}{dy}$$

Here τ_0 is the formation time of the QGP state (typically ~1 fm/c) and $r_0 {A_P}^{1/3}$ is the projectile's nuclear radius. The transverse energy, E_T, is the energy lost by the incident baryons that is redistributed among many particles emitted at a polar angles θ_i. It is defined as:

$$E_T = \sum E_i \ sin\theta_i$$

where E_i is the kinetic energy for baryons and the total energy for all other particles. The highest transverse energies correspond to the most violent central collisions where the conditions to create the QGP are more likely to develop.

Achieving high energy/baryonic density

In the initial stage of the "*Little Bang*" by means of relativistic nucleus-nucleus collisions with heavy ion accelerators. Suppose we accelerate two heavy nuclei such as Au nuclei (A=197) up to relativistic/ultra-relativistic energies and cause a head-on collision. In such relativistic energies, the nuclei are Lorentz-contracted as "*pancakes*". When the center-of-mass energy per nucleon is more than about 100 GeV, the colliding nuclei tend to pass through each

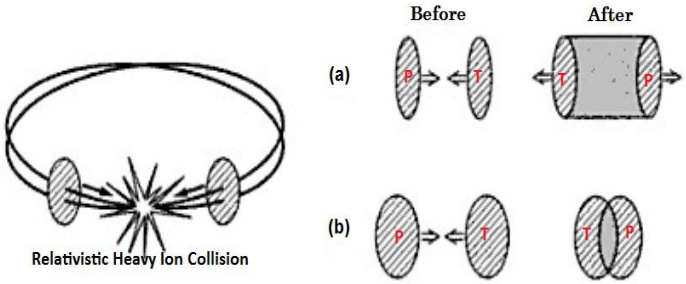

Figure 1.17: **(a)**Formation of QGP at high temperature by means of relativistic nucleus-nucleus collision with a collider-type accelerator. **(b)** Formation of QGP at high baryon density by means of less energetic collision than in (a)

other as depicted in Fig. 1.17(a), and the produced matter between the receding nuclei is high in energy density and temperature but low in baryon density. The Relativistic Heavy Ion Collider (RHIC) at Brookhaven National Laboratory (BNL) and the Large Hadron Collider (LHC) at CERN provide us with this situation. On the other hand, when the energy is at a few to a few tens of GeV per nucleon, the colliding nuclei tend to stay with each other as depicted in Fig. 1.17(b). In this case, not only high temperature but also high baryon density could be achieved [27]. SPS and future CBM experiment at FAIR provide this situation. Theoretically, we say when the incident beam energy that exceeds the velocity of sound in nuclear matter at ground state matter density ($\beta_s = 0.2$), nucleons in heavy ion collisions cannot escape fast enough and zone of high density is formed.

1.7 Kinematic Variables

1.7.1 Rapidity

The Rapidity of a particle is defined in terms of its energy-momentum components p_0 and p_z by

$$y = \frac{1}{2} ln(\frac{p_0 + p_z}{p_0 - p_z}) \tag{1.14}$$

It is a dimensionless quantity which can be either positive or negative. In the non-relativistic limit, the rapidity of a particle travelling in the longitudinal direction is equal to the velocity of the particle in units of the speed of light. The rapidity of the particle in one frame of reference is related to the rapidity in another Lorentz frame of reference by an additive constant. We can write y as:

$$p_0 = m_T \ cosh(y) \tag{1.15}$$

where m_T is the transverse mass of the particle:

$$m_T^2 = m^2 + p_T^2 \tag{1.16}$$

and relation between longitudinal momentum and y is :

$$p_z = m_T \ sinh(y) \tag{1.17}$$

under lorentz transformation from the laboratory frame to a new coordinate frame moving with a velocity β (v/c = v, in natural units)in the z-direction, the rapidity y' of the particle in the new frame is related to the rapidity y in the old frame by

$$y' = y - y_\beta \tag{1.18}$$

where y_β is

$$y_\beta = \frac{1}{2} ln(\frac{1+\beta}{1-\beta}) \tag{1.19}$$

y_β is just the rapidity of the moving frame. so,

(rapidity of a particle in moving frame) = (rapidity in the rest frame)-(rapidity of the moving frame)

In the collision of a beam particle b with momentum b_z on a target particle a with momentum a_z. We can show that initial rapidities of the particles are:

$$y_a = sinh^{-1}(a_z/m_a) \qquad (target) \tag{1.20}$$

$$y_b = sinh^{-1}(b_z/m_b) \qquad (beam) \tag{1.21}$$

where m_a and m_b are the rest masses of particles a and b respectively. For the case when the rest mass of the projectile and the rest mass of the target particle are the same, we can show that the rapidity of the center-of-mass frame is given by

$$y_{cm} = (y_a + y_b)/2$$

and, in the center-of-mass frame, the rapidities of a (target) and b (beam) are

$$y_a^* = \text{-}(y_a - y_b)/2$$

$$y_b^* = (y_b - y_a)/2$$

The greater the incident energy the greater is the separation between the projectile rapidity and the target rapidity.

Central rapidity

The region of the rapidity about midway between the projectile rapidity and the target rapidity is the central rapidity region. The rapidities of the produced particles lie mostly in this region. For example, in a *pp* collision at a laboratory momentum of 100 GeV/c, the beam rapidity y_b is 5.36 and the target rapidity y_a is 0. The central rapidity region is around $y \approx 2.7$ [23].

1.7.2 Pseudorapidity

To determine the rapidity of the particle, we need two quantities of the particle, such as its energy and its longitudinal momentum. In many experiments, it is only possible to measure the angle of the detected particle relative to the beam axis. In that case, it is convenient to utilize this information by using the *psuedorapidity variable* η to characterize the detected particle. the pseudorapidity variable of a particle is defined as:

$$\eta = -ln[tan(\theta/2)] \tag{1.22}$$

where θ is the angle between the particle momentum p and the beam axis. In terms of the momentum, η can be written as

$$\eta = \frac{1}{2} ln(\frac{|p| + p_z}{|p| - p_z}) \tag{1.23}$$

clearly at large momentum (relativistic energies) $y \approx \eta$. In hadron collider physics, the rapidity (or pseudorapidity) is preferred over the polar angle θ because, loosely speaking, particle production is constant as a function of rapidity. One speaks of the "*forward*" direction in a hadron collider experiment, which refers to regions of the detector that are close to the beam axis, at high η.

The difference in the rapidity of two particles is independent of Lorentz boosts along the beam axis.

We can express the rapidity variable (y) in terms of pseudorapidity (η) variable as

$$y = \frac{1}{2} ln[\frac{\sqrt{p_T^2 cosh^2(\eta) + m^2} + p_T sinh(\eta)}{\sqrt{p_T^2 cosh^2(\eta) + m^2} - p_T sinh(\eta)}] \tag{1.24}$$

where m is the rest mass of the particle. Conversely, the pseudorapidity variable η can be expressed in terms of the rapidity variable y by

$$\eta = \frac{1}{2} ln[\frac{\sqrt{m_T^2 cosh^2(\eta) - m^2} + m_T sinh(\eta)}{\sqrt{m_T^2 cosh^2(\eta) - m^2} - m_T sinh(\eta)}] \tag{1.25}$$

If the particle have a distribution $dN/dyd\vec{p}_T$ in terms of the rapidity, then the distribution in the pseudorapidity variable η is

$$\frac{dN}{d\eta d\vec{p}_T} = \sqrt{1 - \frac{m^2}{m_T^2 cosh^2(y)}} \frac{dN}{dyd\vec{p}_T} \tag{1.26}$$

Because the shape of the rapidity distribution dN/dy does not change when one goes from the center-of-mass to the laboratory frame, the peak value of the pseudorapidity distribution in the center-of-mass frame is lower than the peak value of the pseudorapidity distribution in the laboratory frame [23].

Conversion

Hadron colliders measure physical momenta in terms of transverse momentum p_T , polar angle in the transverse plane ϕ and pseudorapidity η. To obtain cartesian momenta (p_x, p_y, p_z) (with z being the beam axis)

$$p_x = p_T\ cos(\phi),\ \ p_y = p_T\ sin(\phi), \text{ and } p_z = p_T/tan(\theta)$$
$$\text{with} \quad \theta = 2\ tan^{-1}(e^{-\eta}),\ \ p_z = p_T\ sinh(\eta), \text{ and } \ |p| = p_T cosh(\eta)$$

1.8 Motivation and Plan of Present Work

The work presented in this dissertation is based on the Compressed Baryonic Matter (CBM) Experiment at FAIR, the primary motivation of which is to investigate highly compressed cold nuclear matter at very high densities and moderate temperatures. Matter in this form exists in the core of the neutron stars and in the core of supernova explosion. This approach is complementary to the studies of matter at high temperatures and low net densities performed at RHIC and LHC. In the present work, the simulated data generated for CBM Experiment is used for analysis. The generation of charmonia and their subsequent decay into muon pairs are done using PLUTO event generator. The mother particles are distributed thermally in p_T and Gaussian in rapidity. The multiplicities are taken from Hadron-String Dynamics (HSD) model. Background events are calculated with the UrQMD event generator. The work is based on the simulation of the physics performance of the muon chamber(MuCh) detector. This detector will measure the complete spectrum of low mass vector meson,i.e. ρ, ω, ϕ and charmonia(J/ψ) via their muonic decay in Au + Au (gold-gold) collisions at 25 AGeV. The dissociation of these resonances in a deconfined medium is one of the promising signatures of QGP formation and its investigation. For efficient reconstruction of charmonia, first Iron absorber of the detector will be analysed.

The present thesis is organized is as follows: The chapter-I describes the introduction of High Energy Physics and signature of QGP. In chapter-II, a brief description of the CBM experiment and various detectors used in this experiment are described. Chapter-III explains about the muon chamber used in the CBM detector setup. Chapter-IV describes the simulation tools and CBM feasibility studies. Chapter-V introduces the observables in CBM experiment and absorber system with the work done so far. In Chapter-VI, simulation analysis results for the optimisation of first absorber system of MuCh for the Au + Au collisions at 25 AGeV are presented.

Chapter 2

The CBM Experiment at FAIR

High-energy heavy-ion collision experiments worldwide are devoted to the investigation of strongly interacting matter under extreme conditions. Experiments at RHIC and LHC are to investigate the properties of deconfined QCD matter at very high temperatures and almost zero net baryon densities. In order to explore the QCD phase diagram at high net-baryon densities, several experimental programs are planned like STAR and PHENIX collaborations at RHIC to search for the QCD critical endpoint [64], CERN-SPS for the same reasons [65], Joint Institute for Nuclear Research (JINR) in Dubna, a heavy-ion collider project (NICA) to search for the coexistence phase of nuclear matter [66]. Due to luminosity limitations these experiments are constrained to the investigation of bulk observables which are - except for elliptic flow - predominantly sensitive to the late and dilute phase of the collision when most of the particles freeze out. In contrast, the research program of the Compressed Baryonic Matter (CBM) experiment at FAIR is focused on the measurement of diagnostic probes of the early and dense phase of the fireball evolution due to high beam luminosity and fast detector system. This approach offers the possibility to find signatures of partonic degrees-of-freedom, and to discover the conjectured first order deconfinement phase transition and its critical endpoint. Another important goal is the study of in-medium modifications of hadronic properties in order to shed light on the phenomenon of chiral symmetry restoration in dense hadronic and partonic matter, and study of the nuclear equation of state at high baryonic densities.

2.1 The Facility for Anti-proton and Ion Research (FAIR)

The FAIR accelerator facility comprises a multifaceted science program, with beams of stable and unstable nuclei as well as antiprotons in a wide range of intensities and energies and excellent beam qualities [63]. A sketch of the future FAIR together with the existing GSI facilities is presented in Figure 2.1.

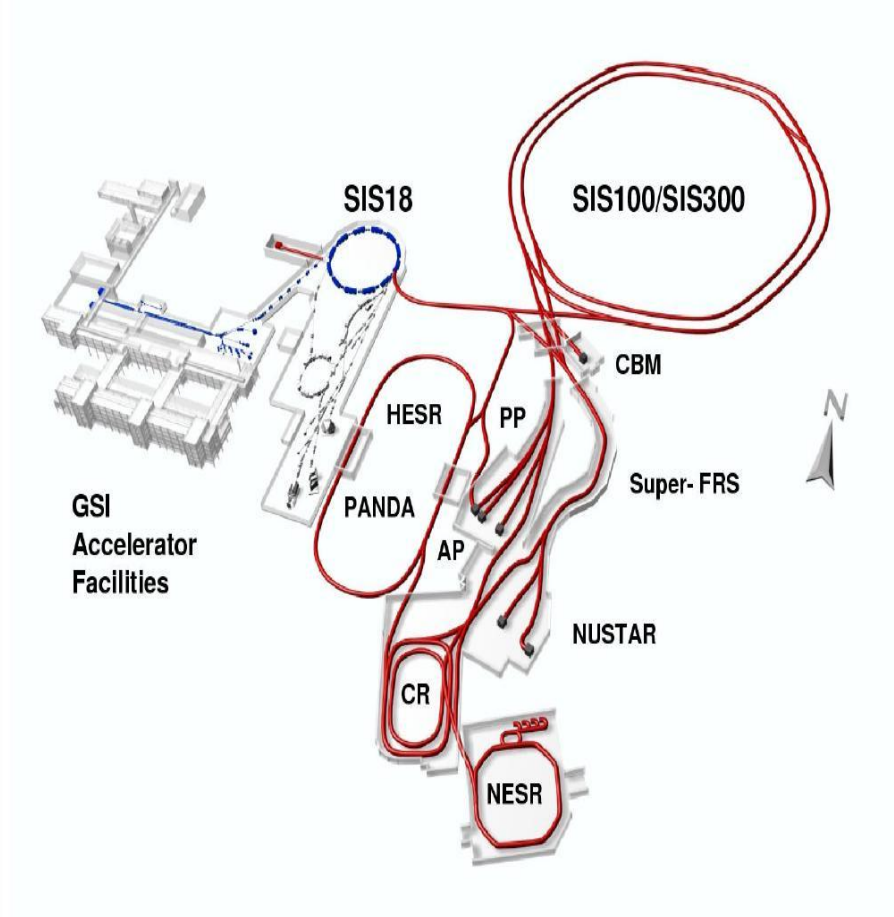

Figure 2.1: FAIR Layout at GSI, Germany.

FAIR comprises two synchrotrons (SIS 100/300) with a circumference of about 1000m and with magnetic rigidities of 100 Tm and 300 Tm, respectively. In conjunction with an upgrade for high intensities, the existing GSI accelerators UNILAC and SIS 18 serve as injectors for the new synchrotrons. Adjacent to the double-synchrotron is a complex system of storage-cooler rings and experiment stations, including a superconducting nuclear fragment separator (Super-FRS) and an antiproton production target. Beyond, there is the storage ring for

Table 2.1: Ion species and their kinetic energy per nucleon for a beam rigidity of 100 Tm at the SIS100 and 300 Tm at the SIS300 (E/A is in GeV)

Beam	**Z**	**A**	**E/A GeV (SIS100)**	**E/A GeV (SIS300)**
p	1	1	29	89
d	1	2	14	44
Ca	20	40	14	44
Ni	28	58	13.6	42
In	49	115	11.9	37
Au	79	197	11	35
U	92	238	10.7	34

antiprotons [high-energy storage ring (HESR)], the collector ring (CR), and the new experimental storage ring (NESR). SIS100 accelerator will deliver energies up to 11 AGeV for Au, 14 AGeV for Ca, and 29 GeV for protons. SIS300 will deliver energies up to 35 AGeV for Au and 89 GeV for protons which will be available hopefully two years later than SIS100 and full CBM detector system will be available thereafter. On one hand, FAIR provides beams of rare isotopes and antiprotons with an unparalleled intensity and quality and on the other hand, the facility is designed to provide particle energies twenty times higher than those achieved at GSI so far. Up to now, this energy regime has only been explored at the AGS up to about 14 AGeV. Due to the intrinsic cycle times of the accelerator and storage-cooler rings, up to multiple research programs can be run in parallel: (1) CBM experiment investigating nucleus-nucleus collisions at highest baryon densities, (2) PANDA detector for hadron physics experiments using cooled high-energy antiproton beams, (3) NUSTAR detectors used for experiments on the structure of unstable nuclei and on nuclear astrophysics as well as experimental setups for plasma physics and atomic physics. Beams to HADES and CBM will be delivered by the SIS100 and SIS300 synchrotrons. The available kinetic beam energy per nucleon depends essentially on the bending power **B.r** provided by the dipole magnets [$E/A = \sqrt{(0.3 \times B.r \times Z/A)^2 + m^2} - m$, with Z and A being the charge and atomic number of the ion, and m the mass of the nucleon]. The beam energies obtained for the maximum beam rigidity of SIS300 (**B.r** = 300 Tm) are listed in Table 2.1 for different ion species to have wide range of beam energies available. The minimal available ion beam energy is about 2 AGeV [62].

2.1.1 Experiments at SIS100 Accelerator

SIS100 accelerator will deliver energies up to 11 AGeV for Au, 14 AGeV for Ca, and 29 GeV for protons. Heavy-ion beams in the energy range between 2 and about 14 AGeV are ideally suited to explore the properties of dense baryonic matter. According to transport calculations, energy densities up to 2.5 GeV

fm^{-3} and baryon densities of 2-7 times saturation density ρ_0 are expected to be reached in the center of the reaction zone. Such conditions prevail in core collapse supernova and in the core of neutron stars. The following fundamental questions can be addressed experimentally with heavy-ion collisions at SIS100:

- What is the electromagnetic structure of dense baryonic matter?
- What are the properties of hadrons in dense baryonic matter?
- Is chiral symmetry restored at very high baryon densities?
- What is the equation-of-state of nuclear matter at neutron star core densities?
- What are the relevant degrees-of-freedom in the vicinity of the deconfinement phase transition?
- Does strange matter exist in the form of heavy multi-strange objects?
- How is charm produced at threshold beam energies?
- How does charm propagate in nuclear matter?

Measurements of dilepton pairs permit to investigate the in-medium spectral functions of low-mass vector mesons. Electron-positron pairs will be measured with the HADES setup.

PANDA research program will investigate production mechanism of charm-anticharm pairs at threshold energies, the properties of charmed particles in nuclear matter at saturation density by utilizing proton beam energies up to 29 GeV, and the propagation of charm in cold nuclear matter by varying the size of the target nucleus.

The yields, spectra and collective flow of (multi-) strange hyperons(Λ , Ξ , and Ω) at SIS100 can be identified via the topology of their weak decays ($\Lambda \longrightarrow p\pi$, $\Xi \longrightarrow \Lambda\pi$, $\Omega \longrightarrow \Lambda K$), as illustrated in Figure 2.2, requiring a tracking detector inside a magnetic field. Measurements of hadrons including multistrange hyperons will be performed with a start version of CBM comprising the dipole magnet, the silicon tracking system, and a time-of-flight wall.

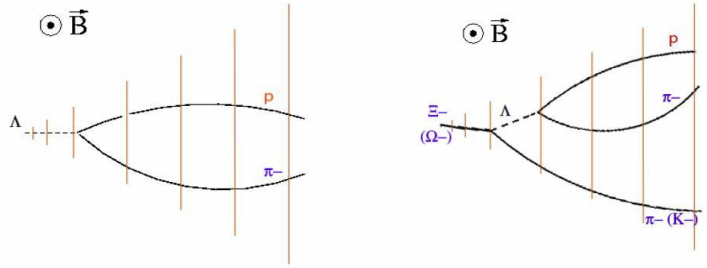

Figure 2.2: Decay topologies of hyperons. Detector planes are indicated as lines,the magnetic field is perpendicular to the plane.

The identification of particles with open charm requires the CBM start version equipped with an additional small micro-vertex detector for reconstruction of displaced vertices of D mesons. For the identification of charmonium in proton-nucleus collisions a reduced version of the planned CBM muon detection system has to be installed.

2.1.2 Experiments at SIS300 Accelerator

SIS300 accelerator will deliver energies up to 35 AGeV for Au and 89 GeV for protons which will be available after two years of SIS100. The most promising observables from nucleus-nucleus collisions in the SIS300 energy range are:

- Particles containing charm quarks (D-mesons and charmonium) to probe the highly compressed baryonic matter.
- Low-mass vector(ρ, ω and ϕ) mesons decaying into dilepton pairs carrying undisturbed information on hadron properties in the dense and hot fireball.
- The collective flow of identified hadrons carrying the information on the equation-of-state of dense matter.
- Kaons, hyperons (Λ, Ξ, Ω and their antiparticles) and hadronic resonances (as ϕ, K^*, Λ^*) carrying strange quarks which are sensitive to the fireball evolution.
- Event-wise dynamical fluctuations of particle multiplicities and momenta are expected to occur if the system passes a first order phase transition or the critical endpoint.
- Photons which could provide information on direct radiation from the early fireball.
- Two-particle correlations carrying information of the source size and time evolution of the fireball and particle production.

Key feature of the CBM experimental program is a systematic and comprehensive measurement of excitation functions and system size dependencies of all observables. Particular emphasis will be put on rare diagnostic probes which are not accessible by other experiments in this energy range. The identification of rare probes requires high beam intensities, a large duty cycle, excellent beam quality, and running times of several months per year. Observables like event-by-event fluctuations require full azimuthal coverage of the produced particles in a wide acceptance of rapidity and transverse momentum and excellent centrality determination [62].

2.2 CBM Detector Concepts

The goal of the experiment is to measure multiplicities, phase-space distributions and flow of protons, pions, kaons, hyperons, hadronic resonances, light vector mesons, charmonium and open charm including their correlations and event-by-event fluctuations in heavy-ion collisions. The technical challenge of the CBM experiment is to identify both, hadrons and leptons, and to filter out rare probes at reaction rates of up to 10 MHz [70] with charged particle multiplicities of up to 1000 per event. Measurements at these high rates cannot be performed with slow detectors like Time-Projection Chambers (TPC), but rather require extremely fast and radiation hard detector (and electronic) components. Moreover, the experiment has to provide lepton identification, high-resolution secondary vertex determination and a high speed trigger and data acquisition system. The CBM detector system will have the capability to measure both electrons and muons. This approach combines the advantages of both methods, and guarantees reliable results as in the end both data sets should agree to each other in spite of the very different background sources [63]. The layout of the CBM experimental setup is sketched in Fig. 2.3.

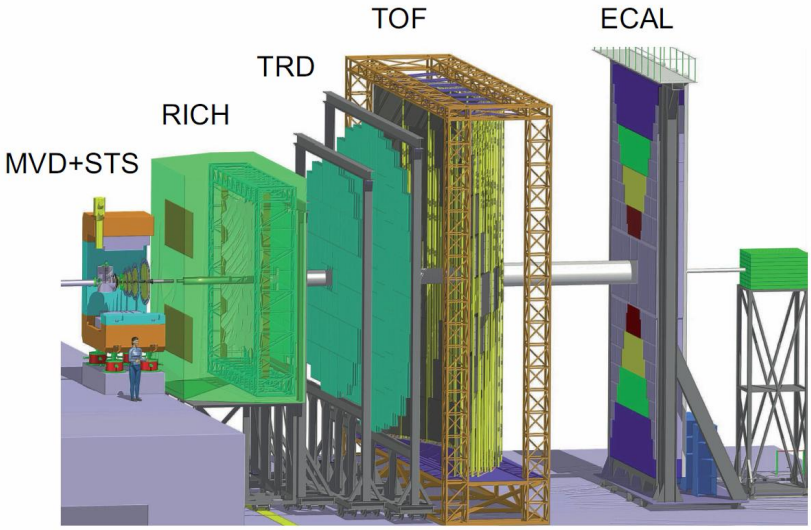

Figure 2.3: The CBM experiment setup consists of a large acceptance dipole magnet, radiation-hard Silicon pixel/strip detectors for tracking and vertex determination (STS, MVD), a Ring Imaging Cherenkov detector (RICH) and Transition Radiation Detectors (TRD) for electron identification, Resistive Plate Chambers (RPC) for time of flight measurement, an Electromagnetic Calorimeter (ECAL) for photon identification, and a Projectile Spectator Detector (PSD) for centrality and reaction plane determination.

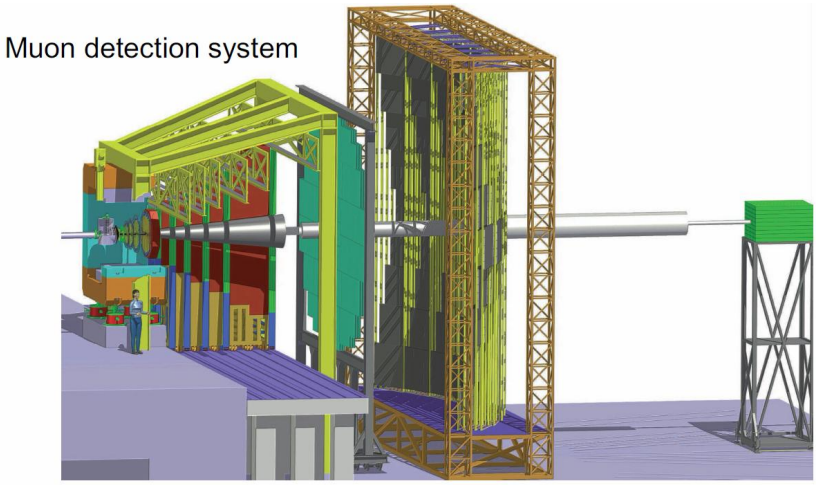

Figure 2.4: The Compressed Baryonic Matter (CBM) experiment set-up with a muon detection system (MuCh) with alternating absorber and detector layers instead of the RICH.

The heart of the experiment will be a silicon tracking and vertex detection system installed in a large acceptance dipole magnet. The STS allows for track reconstruction in a wide momentum range from about 100 MeV up to more than 10 GeV with a momentum resolution of about 1%. The Micro-Vertex Detector (MVD) is needed to determine secondary vertices with high precision for D-meson identification close to the target.

The measurement of electrons will be performed with a Ring Imaging Cherenkov (RICH) detector (for momenta below 8-10 GeV/c) together with Transition Radiation Detectors (TRD) for electrons with momenta above 1.5 GeV/c.

Muons will be measured with an active hadron absorber system consisting of iron layers and muon tracking chambers (MuCh). For muon measurements the MuCh will be moved to the position of the RICH as shown in Fig. 2.4.

Charged hadron identification will be performed by a time-of-flight (TOF) measurement with a wall of RPCs located at a distance of 10 m behind the target.

The setup is complemented by an Electromagnetic Calorimeter (ECAL) in selected regions of phase space providing information on photons and neutral particles, and by a Projectile Spectator Detector (PSD) needed for the determination of the collision centrality and the orientation of the reaction plane.

A key feature of the CBM experiment is online event selection which requires free streaming read-out electronics and fast algorithms running on computer farms based on future many-core architectures [62]. The CBM detector components required for the measurement of the different observables are listed in Table 2.2.

Table 2.2: Observables and required detectors. Detectors marked as (x) can be used to suppress background.

Observables	MVD	STS	RICH	MuCh	TRD	RPC	ECAL	PSD
π, K, p		x	(x)		(x)			x
Hyperons		x			(x)	(x)		x
Open Charm	x	x	(x)		(x)	(x)		x
Electrons	x	x	x		x	x		x
Muons		x		x		(x)		x
Photons							x	x
γ via $e^{\pm}$	x	x	x		x	x		x

2.2.1 Silicon Tracking System (STS) and Micro-Vertex Detector (MVD)

The task of the STS is to provide track reconstruction and momentum determination of charged particles. The multiplicity of charged particles is up to 600 per event within the detector acceptance. Between the target and the STS, a Micro-Vertex Detector (MVD) enables to distinguish particle decay vertices from the event vertex. A benchmark observable is the D meson (open charm), a rare probe that has to be identified via its hadronic decays $D^0 \rightarrow K^-\pi^+$ and $D^{\pm} \rightarrow K^{\mp}\pi^{\pm}\pi^{\pm}$ [9]. This challenging task requires a detector with high position resolution, very low material budget, high radiation tolerance and a fast self-triggered readout.

The STS-MVD layout is placed inside a magnetic dipole field, as shown in figure 2.6, which provides the bending power required for momentum determination with an accuracy of about $\Delta p/p = 1\%$.

The STS comprises 8 detector stations placed in 30, 35, 40, 50, 60, 75, 95, 100 cm distance from the target fully based on low-mass silicon micro-strip detectors for the track point measurement. The stations have ladder structure and are build of 300 μm thick double-sided silicon micro strip sensors and 60 μm strip pitch read-out electronics is placed at the perimeter of the STS. Signals from sectors are sent through thin capton micro-cables to the front-end boards.

The MVD comprises two detector stations. They are located at 5 and 10 cm (alternatively 10 and 20 cm) downstream of the target and will be installed in a vacuum vessel. Monolithic Active Pixel Sensors (MAPS) with a pixel size of 40 x 40 μm^2, yielding a high spatial resolution of 3 μm, and a thickness of 100 μm (very thin) would perfectly fulfill our requirements concerning vertex resolution which is needed to measure the displaced vertices of D mesons (open charm). Fig. 5.5 shows the simulated track multiplicity at STS and illustration of an open charm decay. The R&D on MAPS concentrates on the improvement of radiation hardness and readout speed is going on.

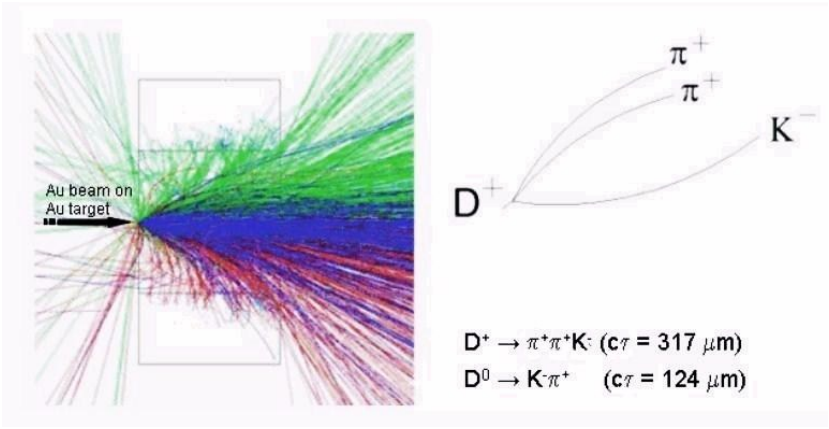

Figure 2.5: (Left) Simulation of a central Au+Au collision at 25 GeV/nucleon in the STS.(Right) Illustration of rare "open charm" decays to be identified as detached vertices in about 100 μm distance from the event vertex.

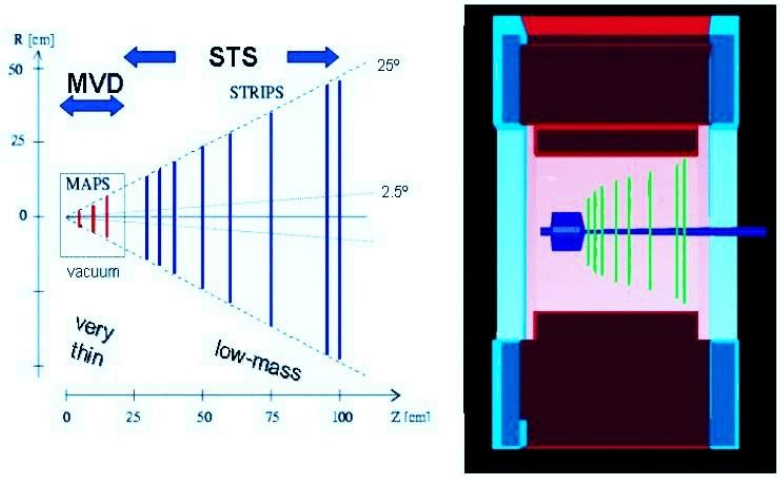

Figure 2.6: (Left) Schematical cross section of the detector concept. The target is on the left hand side. The first two (or three) stations from the target are the Micro Vertex Detector (MVD). They will be built from thin MAPS pixel detectors that may be installed in vacuum. The remaining stations form the Silicon Tracking System (STS) for the track and momentum reconstruction of all charged particles. They will be built from micro-strip detectors. (Right) View of the STS/MVD in the dipole magnet with the beam pipe and the vacuum section of the MVD shown [71].

Major Challenges are :

As an example for Au+Au collisions at 25 GeV/nucleon:

- *High track densities*: 600 charged particles in polar acceptance 2.5 - 25 ^{o}
- *High r/o speed, Radiation hardness*: 10 MHz interaction rate (10^9 ions/s on $1\%\lambda^{int}$ target), only high-level triggers.

2.2.2 Ring Imagining Cherenkov (RICH) Detector

The RICH detector will serve for electron identification from lowest momenta up to 10-12 GeV/c needed for the study of the dielectronic decay channel of vector mesons. In the current CBM detector layout the RICH would be positioned behind the magnet with the silicon tracking system (STS/MVD) and in front of the first transition radiation detector (TRD). Combined with particle identification information from the other detectors, a pion suppression of 10000 is required out of which a factor 100-1000 has to be provided by the RICH alone. High detection efficiency of electrons is also required which calls for 10-15 hits per electron ring at minimum. As global tracking has to connect tracks in the STS and TRD, therefore the RICH detector should not extend 3 m and and a material budget of 3-4 % radiation length in order to reduce multiple scattering. A large acceptance of 25^o in the laboratory has to be covered to identify the vector mesons in a wide range of rapidity and transverse momentum. The current detector concept foresees:

- ***Gaseous RICH detector*** *with vertically separated mirrors (R=450 cm), gas vessel (*$\sim (6-7)m \times 5m \times 3m$*))*

- ***Radiator****:* N_2 *(if needed with admixture of* CO_2 *for suppression of fluorescent light [72]):* Nitrogen would fulfill all requirements to radiate at lowest momentum, easy to handle, inflammable & easy way to separate pions almost 90 % from electrons. One concern of nitrogen might be its fluorescence which could be quenched by some addition of CO_2 [67]. For photo-multiplier tube detector, a lower wavelength cutoff of 175-150nm is fine which also avoid chromatic dispersion for ring resolution.

- ***Mirror****: glass or carbon substrate,* $Al+MgF_2$ *coating, surface* $\sim (5-6)m \times 4m$: Maximum allowable radiation length will determine whether glass mirrors can be used or a lightweight material such as carbon has to be used. The coating should provide highest reflection for the full range of photons not absorbed in the gas and detected by the photodetector, i.e. down to about 150nm. The choice will thus be a Al+MgF_2 coating.

- ***Photodetector*** *(shielded by magnet yoke, granularity* $\sim$ *6mm x 6mm):* Highly granulated PMTs(Photo Multiplier Tubes) are foreseen as photodetectors. While determining the final number of hits/ring, special care has to be taken to enhance the detection of photons from lower wavelengths. Basically two concepts are discussed currently:

  1. Development of small size PMTs (diameter 6-7mm) by IHEP Protvino with bialkali photocathode, glass window and a wave length-shifter

film (p-terphenyl) to enhance the sensitivity in the near UV.

2. MAPMTs, e.g. from Hamamatsu (H8500) with pixel sizes of 6mm x 6mm, bialkali photocathode and UV window to enhance the sensitivity in the near UV.

Simulations are being performed to optimize the size and geometry of the RICH with respect to performance and costs. The same performance can e.g. be kept when reducing the overall size by a factor 2-3 [72] by choosing CO_2 as radiator gas and a mirror of radius 3 m [62].

2.2.3 The Transition Radiation Detector (TRD)

Transition Radiation (TR) is X-rays of about 10 KeV produced when ultra relativistic particles cross the boundary between two media with different dielectric constants ϵ's. This phenomenon is used in the CBM experiment to separate pions from electrons as pions do not produce any TR. This is due to their large mass because the intensity of TR is proportional to Lorentz factor γ ($\gamma \simeq E/m$). The emission angle of TR is concentrated in a narrow cone of an angle $\theta \simeq 1/\gamma$. Electrons generated by gas ionization and by absorption of TR photons on the track as well as primary electrons, which come from the interaction of the charged particle with the atoms of gas, drift towards the anode wires where they trigger avalanches due to the ionization of atoms. The electrons travel to the anode while the positive ions give the signal on the pad plane.

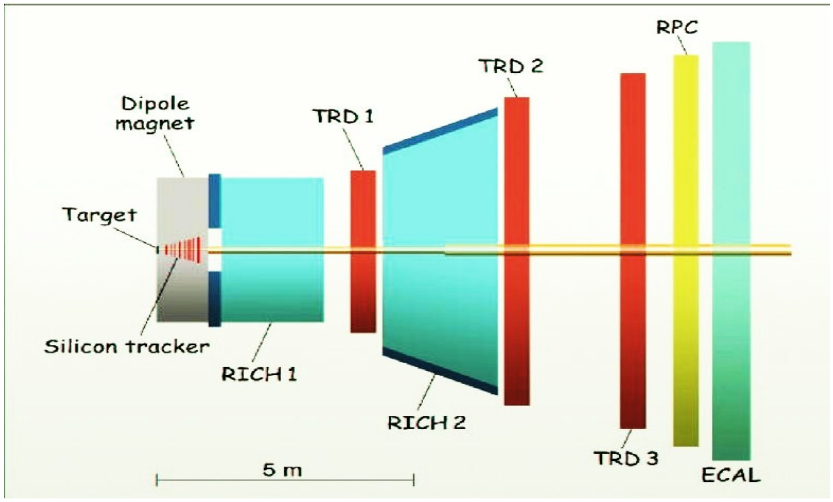

Figure 2.7: Proposed scheme of TRD sub-detector for CBM

Three Transition Radiation Detector stations each consisting of 3-4 detector layers will serve for particle tracking and for the identification of electrons and

positrons with $p > 1.5$ GeV/c ($\gamma > 1000$). The detector stations are located at approx. 5 m, 7.2 m and 9.5 m downstream the target, the total active detector area amounts to about 600 m^2 as shown in Fig. 2.7. The detector development concentrates on the improvement of the electron identification performance, and on the development of highly granular and fast gaseous detectors in particular for the inner part of the detector planes covering forward emission angles. For example, at small forward angles and at a distance of 5 m from the target, we expect particle rates on the order of 100 KHz/cm^2 for 10 MHz minimum bias Au+Au collisions at 25 AGeV. In a central collision, particle densities of about 0.05/cm^2 are reached. In order to keep the occupancy below 5% the minimum size of a single cell should be about 1 cm^2. The TRD detector readout will be realized in rectangular pads giving a resolution of 300-500 ìm across and 3-30 mm along the pad. Every second TR layer is rotated by 90^o [62]. Prototype gas detectors based on MWPC (Multi-Wire Proportional Chamber)and GEM (Gas Electron Multiplier) technology have been built and tested with particle rates of up to 400 KHz/cm^2 without deterioration of their performance. The pion suppression factor obtained with 12 TRD layers is estimated to be well above 100 at an electron efficiency of 90%.

2.2.4 The Muon Chamber system (MuCh)

The measurements of J/ψ and low mass vector meson (ρ, ω, ϕ) decay into $\mu^+\mu^-$ in heavy-ion collisions have been proposed as a key probe to indication of in-medium modification of hadrons, chiral symmetry restoration, and deconfinement at high ρ_b. The experimental challenge for muon measurements in heavy-ion collisions at FAIR energies is to identify low-momentum muons in an environment of high particle densities [69].

The CBM concept is to track the particles through a hadron absorber system, and to perform a momentum-dependent muon identification. This concept is realized by segmenting the hadron absorber in several layers, and placing triplets of tracking detector planes in the gaps between the absorber layers. The absorber/detector system is placed downstream of the STS which determines the particle momentum. In order to reduce meson decays into muons the absorber/detector system has to be as compact as possible. The actual design of the muon detector system consists of 6 hadron absorber layers and 15-18 gaseous tracking chambers located in triplets behind each iron slab as shown in Fig. 2.8. The definition of a muon depends on its momentum which varies with the mass of the vector mesons and with beam energy. For example, for beam energies above 15 AGeV muons from the decay of J/ψ mesons have to pass all 6 absorber layers with a total iron thickness of 225 cm corresponding

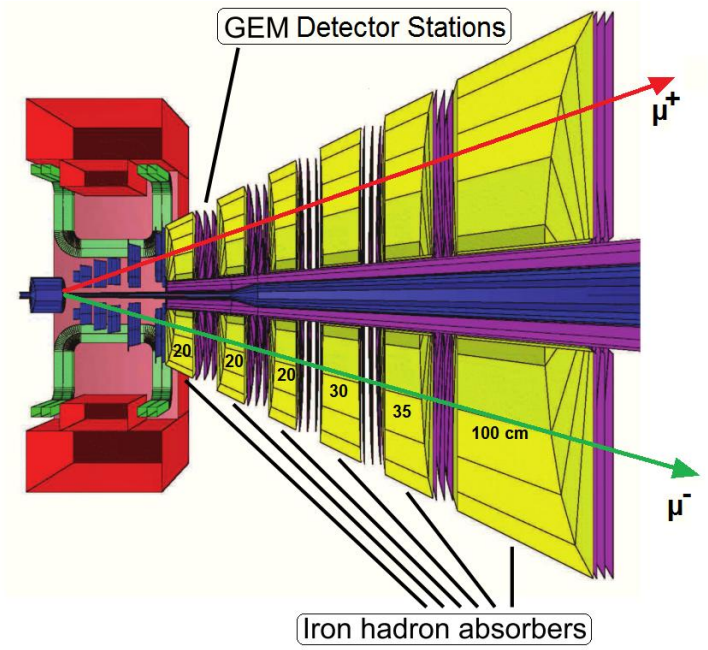

Figure 2.8: The CBM muon detection system consisting of alternating layers of iron hadron absorbers and detectors [70].

to 13.4 interaction length λ_I . The muons from the decay of low-mass vector mesons (ρ, ω, ϕ) only have to penetrate through 5 iron absorber layers with a total thickness of 125 cm (corresponding to 7.5 λ_I). The challenge for the muon chambers and for the track reconstruction algorithms is the huge particle density of up to 1 hit/cm^2 per event in the first detector layers. Therefore, the detector development concentrates on the design of fast and highly granulated gaseous detectors based on GEM(Gas Electron Multiplier) technology [73]. In total, the muon chambers cover an active area of about 70 m^2 subdivided into about half a million channels. Ongoing studies concentrate on the optimization of the muon absorber system in terms of absorber thicknesses, number of absorbers and tracking stations, and required hit resolution, i.e. pad size of the detector. The low particle multiplicities behind the muon absorber enables the implementation of a trigger on muon pairs. The trigger concept is based on the measurement of short track segments in the last tracking station triplet, and extrapolation of these tracks to the target. After selection of tracks with good vertices the event rate can be reduced already by a factor of about 600 for J/ψ measurements in minimum bias u+Au collisions [62].

2.2.5 The Time Of Flight Detector (TOF)

A time-of-flight (TOF) measurement can be used to identify charged particles mass, the particle momentum and the particle track length. The TOF wall consists of approximately 60,000 independent cells providing a resolution of $\sigma_{TOF} \leq 80$ ps [74]. The TOF stop detector of CBM has an active area of about 150m^2 located at a distance of 10 m from the target. A diamond pixel (or micro-strip) detector provides the start signal for the TOF measurement. It directly counts the beam particles at intensities of up to 10^9 ions/s. The requirements for the TOF detector can be satisfied by a tRPC (timing Resistive Plate Chamber) with 25-30^o coverage. In order to cope with the high beam luminosity, the tRPC must handle rates of up to 20 kHz/cm^2, while the FEE (Front End Electronics) must process the GHz signals from the tRPC at an interaction rate of up to 10 MHz. The current development of tRPCs shows very good performance in terms of high rate capability, low resistivity material, long term stability, and the possibility to build large arrays with sufficient timing performance. First prototypes with glass electrodes have already been built and tested. With an efficiency of 95% they showed a time resolution of 120 ps at rates of 18 kHz/cm^2 [75]. With an overall efficiency of 80% to 90%, a separation of kaons and pions can be achieved up to laboratory momenta of about 3.5GeV/c, while protons can be identified up to 7GeV/c.

2.2.6 The Projectile Spectator Detector (PSD)

The Projectile Spectator Detector (PSD) is a compensating, modular lead-scintillator calorimeter, which is used to determine the collision centrality. Good knowledge of the impact parameter is particularly important for analyzing event-by-event fluctuations, and in order to study collective effects like flow for which a well defined reaction plane is important [76]. The PSD will measure nucleons from the projectile nucleus which did not interact. It is composed of 12 $\times$ 9 modules, each consisting of 60 lead/scintillator layers with a surface of 10 x 10 cm^2. The photons produced in the scintillator are measured via wavelength shifting by Multi-Avalanche Photo-Diodes (MAPD) of the size of $3\times3\ mm^2$ and with a pixel density of 104/mm^2.

2.2.7 Data Acquisition System (DAQ)

In order to access very rare probes and to measure all particles with the required statistical accuracy, measurements at very high event rates are envisaged for CBM. At a beam intensity of 10^9 ions/s and an interaction probability of 1% in the target, event rates of 10 MHz will be reached. Assuming a bandwidth

of 1 GBytes/s and an average event volume of about 40 kByte for minimum bias Au+Au collisions, an event rate of 25 kHz will be accepted by the data acquisition. For this storage rate, online event selection systems are required which reject less interesting events. With event rates of 10 MHz, only one in 400 events can be archived, and online software and hardware selections have to be applied to ensure that none of the interesting rare events are lost and cross sections can be reliably extracted.

The event selection system will be based on a fast on-line event reconstruction running on a PC farm equipped with many-core CPUs and graphics cards. Different many-core architectures developed by Intel, IBM, NVIDIA and AMD are under investigation. Track reconstruction, which is the most time consuming combinatorial stage of the event reconstruction, will be based on parallel track finding and fitting algorithms, implementing the Cellular Automaton and Kalman Filter methods. Novel languages, such as CUDA, Ct and OpenCL, can be used for parallel programming on the heterogeneous CPU/GPU on-line event selection system.

For open charm production the trigger will be based on an online search for secondary vertices which requires high speed tracking and event reconstruction in the STS and MVD. The highest suppression factor has to be achieved for J/ψ mesons where a high-energetic pair of electrons or muons is required in the TRD or in the MuCh. For low-mass electron pairs no online selection is possible due to the large number of rings/event in the RICH caused by the material budget of the STS. In the case of low-mass muon pairs some background rejection on the trigger level seems to be feasible.

Chapter 3

Muon Chamber(MuCh)

Muon was discovered by Anderson and Nedermeir in 1936 in cosmic rays. It has mass 105.658389 MeV (in natural units), lifetime(τ) 2.19703 μs and it either decays via $[\mu^- \rightarrow e^- \ \overline{\nu}_e \ \nu_\mu]$ / $[\mu^+ \rightarrow e^+ \ \nu_e \ \overline{\nu}_\mu]$. There are mainly two muon sources: (a)`Cosmic`, approximately 10^2 muons/m^2.sec reach ground with energy E >1GeV. (b)*Accelerators*, where low p_T muons are products of mesonic decay and high p_T muons are products of heavy object decays like $J/\psi, \Upsilon, b(quark), W/Z$, etc.

Muons can be identified by the large penetrating power and the relevant parameters to be measured very precisely are energy and momentum. Energies of muons beyond the TeV range can be measured with calorimetric techniques. The momenta of muons, just as for all charged particles, are usually determined in magnetic spectrometers.

Muon detector consists of Absorber in between Tracking system (detector). They record "*prompt*" muons from the original reaction, decay products in flight, or simply "*punch through*" hadrons (i.e. showers created by hadrons in absorber which can "*leak*" through in case of thin absorber), so that charged particles are detected after absorber. We can improve momentum resolution detector by reducing multiple interaction by bending muon in air, not in iron after target in case of fixed target experiment, in the central tracker incase of collider experiment. Most common way is to install the thick absorber to absorb the background particles, created from accelerator beam losses, spectators interactions (showers) with accelerator and detector equipment and neutrons etc, made of *steel to catch hadrons*, *poly-materials to absorb neutrons* and *lead to reduce gamma fluxes.*

With the discoveries of J/ψ and $\Upsilon \rightarrow \mu^+ \ \mu^-$ as well as $Z \rightarrow \mu^+ \ \mu^-$ requiring accurate and complete muon detection by charge and momentum. Same is the case for Higgs searches, asymmetry measurements, B$\bar{\text{B}}$ -mixing, and new particle

searches. At future hadron colliders like LHC, FAIR etc. good momentum resolution must be reached under high rates.

3.1 Muon Chamber for CBM Experiment

The design criteria of CBM experiment are driven by the observables like open and hidden charm, short lived vector mesons, event by event fluctuation, strange and multi-strange particles, and collective flow.

The main tracking device in CBM is a set of silicon tracking stations (STS) placed inside a dipole magnet [77, 78, 53]. The tracks measured in STS are used for particle identification and momentum determination. The dilepton pairs will be measured either as electrons or muons. The experimental difficulty is to identify soft leptons from rare decays in the environment of heavy-ion collisions with up to 1000 charged particles. The electron measurement suffers from a large combinatorial background resulting in a moderate signal-to-background (S/B) ratio for vector mesons. The muon measurement seems to provide an excellent S/B ratio for charmonium, but poses the challenge to be efficient also for soft muons. CBM experiment will be a facility where both muons and electron channels will be measured with alternative methods like TRD (transition radiation detection) and Muon Chamber (MuCh) system. In both cases the Silicon Tracking System will provide track reconstruction and momentum determination.

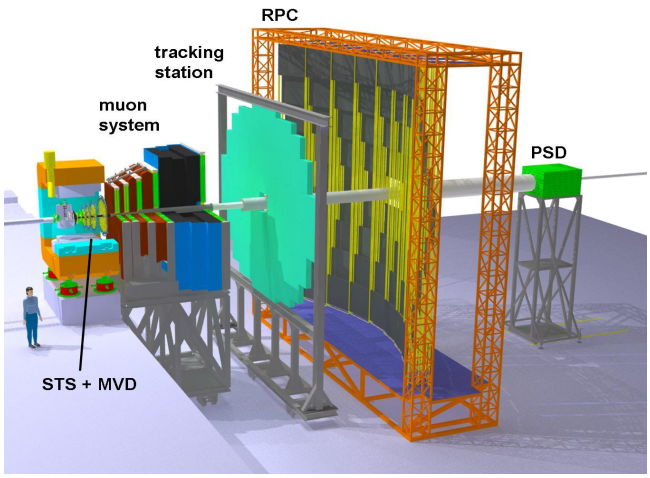

Figure 3.1: Dipole magnet, Silicon Tracking Stations and Muon detection system. D-mesons and hyperons can be identified via their decay topology with the STS only. Hadron identification (π, K, p, ...) is performed with tracking and time-of-flight detectors (not shown) downstream the muon detectors. In this case, the absorbers of the muon detection systems will be removed.

Fig. 3.1 shows a sketch of the muon detection system together with the STS inside the dipole magnet. The muon detection system consists of several absorbers with the tracking inside the absorber by several tracking stations. The muon detection system is followed by a TOF (Time Of Flight) system for background reduction in muon detection. For hadron runs in this setup, absorbers are to be removed.

India will simulate, design, fabricate and operate a large part of the muon detection system of CBM, infact 50% of the detector parts and 100% for its electronics will be contributed. The muon system is proposed to consist of *15-18 tracking chambers* sandwiched between absorbers of varying thickness and material. The chamber/absorber system will be placed downstream the STS. The uniqueness of this muon setup is the slicing of absorber and a series of muon chambers sandwiched between them is governed by the need of detecting very low momentum muons, which would otherwise be absorbed in conventional thick absorber setup. The absorber can be made of *iron or carbon*. Depending on the momentum resolution obtained with the configuration, one option is to go for magnetized iron absorber.

Indian-CBM collaboration is performing R&D work for detector options at various stations. Possible option is to use high resolution fast gas detectors (GEM or MICROMEGAS) at first few stations where particle density is very high and the use of pad chambers at later stages.

3.2 MuCh Detector Design

The experimental and the technical challenges are to design and to build a large area, high-position-resolution detector which has to be operated at a very high particle densities of up to 1 hit/cm^2 per event with an event rate of up to 10 MHz. Figure **??** shows the hit density (per cm^2 per event) at the surface of 16 chambers using two types of absorbers (Fe and Carbon). The optimization of absorber material and thickness is still ongoing, but this plot can be taken as guidance for the required performance of the detectors. Assuming the CBM design value for the interaction rate of 10MHz, the density will be as high as 16 MHz for the first layers of the detector setup. The hit density reduces for the detector stations further downstream. For the simulations shown above, a position resolution of $100\mu m$ has been assumed for hit reconstruction. This number imposes another constrain on the detector design. The numbers given in table 3.1 permits to compare the available gas detector technologies some of them are still in the R&D phase, while the MWPC(Multi-Wire Proportional Chamber) are widely used.

From the `Table 3.1` it appears that GEM or Micromegas are the most

Table 3.1: Various options for muon chambers

	MWPC	**GEM**	**Micromegas**
Rate capability	10^4 Hz/mm^2	>5x10^5 Hz/mm^2	10^6Hz/mm^2
Gain	High 10^6	Low 10^3 (single) >10^5(multi-GEM)	High 10^5
Gain Stability	Drops at 10^4 Hz/mm^2	Stable over 5x10^5 Hz/mm^2	Stable over 10^6Hz/mm^2
2D Readout	Yes	Yes	Yes
Position resolution	>200 μm	50 μm	Good <80 μm
Time resolution	$\sim$ 100 ns	<100 ns	<100 ns
Magnetic Field effect	High	Low	Low
Cost	Expensive fragile	Expensive robust	Cheap robust

suitable option at least for first few stations, whereas for the large detector stations located behind several absorber layers the standard MWPC could be an option.

3.2.1 Multi-Wire Proportional Chamber (MWPC)

Multi-Wire Proportional Chamber was invented by Georges Charpak at CERN in 1968 and was awarded by Nobel Prize in Physics in 1992 and was named an IEEE Milestone in 2005. MWPC is a proportional counter which uses a wire, under high voltage, which runs through a metal or conductive enclosure whose walls are held at ground potential. The enclosure is filled with carefully chosen gas, such as an argon/methane mixture, such that any ionizing particle that passes through the tube will ionize surrounding gaseous atoms. The resulting ions and electrons are accelerated by the electric field around the wire, causing a localised cascade of ionization which is collected on the wire and results in an electric current proportional to the energy of the detected particle. This allows the experimenter to count particles and importantly, in the case of the proportional counter, to determine their energy.

3.2.2 Gas Electron Multiplier (GEM)

The GEM technology, which has been introduced by F. Sauli in 1996, is used in high energy and medical physics detectors to amplify an electron signal in a gaseous detector. GEM consist of a thin Kapton(polyimide) foil(about 50 μm thick) which is coated on both sides with copper layers(about 5 μm). This structure is perforated with holes that typically have a diameter of 70 μm and

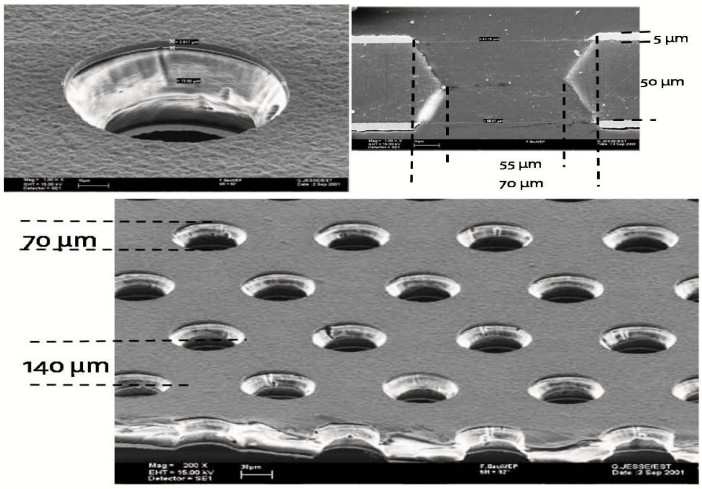

Figure 3.2: GEM structure when viewed in an electron microscope.

a pitch of 140 μm. The holes are arranged in a hexagonal pattern. Due to an chemical etching production process they have a double conical shape with an inner diameter of about 55 μ [79]. Fig. 3.2 shows a picture of a GEM that has been taken with an electron microscope. The working principle of a GEM is illustrated in Fig. 3.3. Between the two copper coatings a voltage of a few 100 V is applied. Since the field lines are focused in the holes, there the resulting electric field strength is in the order of some 10 kV/cm, the electrons which were released on the top side drift into the hole and multiply in avalanche and transfer to the other side, which is high enough for the gas amplification to happen. Hence, each hole represents an independent proportional counter. An appreciable fraction of electrons of the avalanche may emerge from the hole to the gas gap. This effect can be used for amplification in the subsequent stages or for detection at the anode (read-out) electrode. It is possible to achieve amplification up to 10^3 in a single GEM. But usually, a setup consists of two or three successive GEMs, with a lower amplification per GEM but the same or higher amplification in the hole system. The single GEM is operated at a lower voltage, which lowers the probability of sparking in the GEM holes. In this way the setup can be operated very stably.

The field configuration is usually chosen in a way that most electric field lines end on the side towards the cathode, while on the other side most lines go into the direction of the anode. Then, most of the ions from the gas amplification are pulled to and collected on the GEM surface while most of the electrons are extracted out of the GEM holes towards the anode. The electron extraction can be intensified if additionally a magnetic field is applied perpendicular to the GEM plane - as it is the case in Time Projection Chambers. The electrons

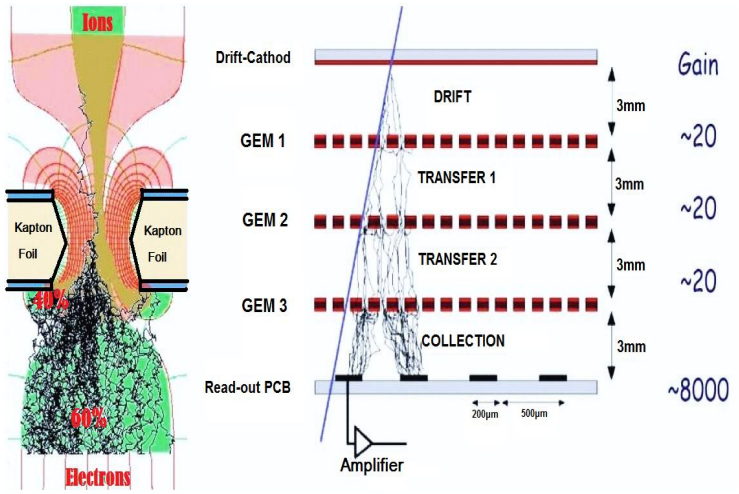

Figure 3.3: (left) pictorial representation of amplification inside the detector under high field inside the hole. (right) working of triple GEM detector.

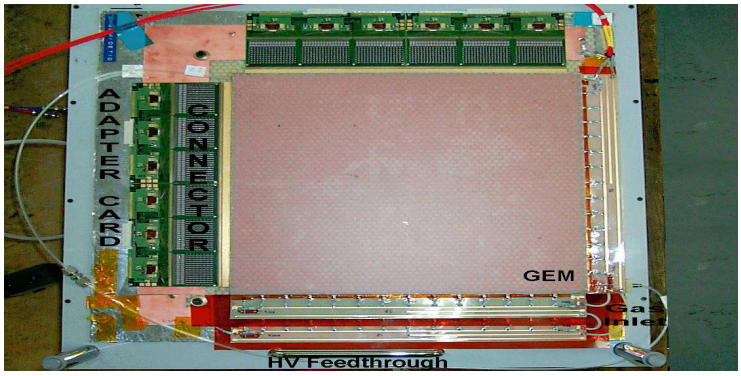

Figure 3.4: GEM prototype.

tend to follow rather the magnetic field lines while the ions -due to their higher mass- still rather follow the electric field lines.

Fig. 3.4 shows a photograph of the inside of this detector. It supports GEM-foils with an active area of $32 \times 32\ cm^2$ and suitable readout structures. Such a setup allows a variation of the number of the GEM-foils, the gap size and the powering scheme. Around the readout structure a Stesalite-frame is glued. Below this frame high voltage connections for the powering of the GEM-foils and the drift field are glued to the support. Additionally a gas inlet is foreseen. A suitable cap with the gas outlet and an exchangeable entrance window (Quartz, Kapton or Mylar) can be put on the bottom frame to close the detector. Gas tightness is provided by O-rings between the frame and the cap. The GEM-foils and the drift cathode are mounted on frames with four drilled holes in the corners of the frame.

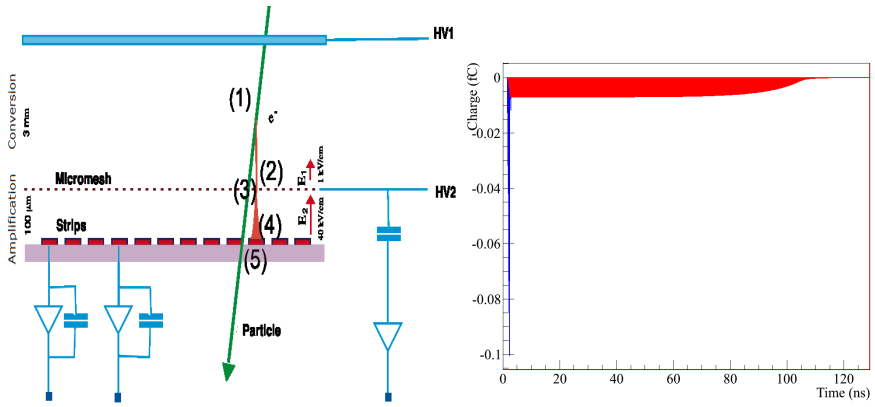

(a) (b)

Figure 3.5: Micromegas(a)Working principle of a Micromegas detector(b)Signal induced on the readout electrode of a Micromegas detector (Simulation). The blue curve shows the part of the signal induced by electrons and the red one by ions.

3.2.3 Micromegas

The Micromegas (Micro-Mesh Gaseous Structure) detector is a gaseous particle detector coming from the development of wire chamber. Invented in 1992 [80] by Georges Charpak and Ioannis Giomataris, the Micromegas detectors are mainly used in high energy experimental physics. From their small amplification gap, they have fast signals in the order of 100 ns with high gain of 10^4. They are precise detectors with a spatial resolution below one hundred of micrometer [81]. The Micromegas detector, as every gaseous detector, detects particles by amplifying the charges that have been created by ionisation in the gas volume divided in two by a metallic micro-mesh placed between 25μm and 150μm of the readout electrode. While passing through the detector, a particle will ionise the gas atoms by pulling up an electron creating an electron/ion pair [80]. Electric field of the order of 400V.cm^{-1} is applied so that electrons drift [81] toward the amplification electrode (the mesh) and the ion toward the cathode. When the electron arrives closed to the mesh [82], it enters an intense electric field (typically in the order of 4kV.cm^{-1}) in the amplification gap. Accelerated by this field, the electron reaches enough energy to produce ion/electron pairs that will also ionise the gas, creating several thousand of pairs known as avalanche effect [83] to create a significant signal. At last, we read the electronic signal on the readout electrode [84] by a charge amplifier. The readout electrode is usually segmented in strips and/or pixels in order to obtain the position of the impinging particle in the detector. The amplitude and the shape of the signal, read via the electronic on the readout electrode, gives information on the time and energy of the particle.

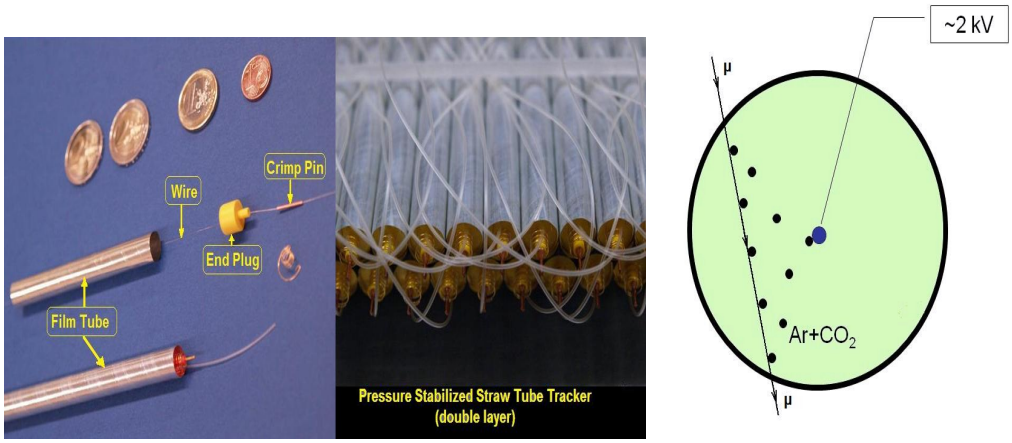

(a) (b)

Figure 3.6: (b)Straw tube parts (b)Working of Straw tube proportional gas detector

The signal is induced by the movement of charges between the micro-mesh and the readout electrode (this volume is called the *amplification gap*). The 100 nanoseconds signal consists of an electron peak (blue in above figure) and an ion tail (red)[see fig 3.5b]. Since the electron mobility in gas is over 1000 times faster than the ion mobility, the electronic signal is much shorter (below 3ns) than the ionic one. That is why it is used to measure precisely the time. The ionic signal caries more than half of the signal and is used to reconstruct the energy of the particle.

3.2.4 Straw Tube Tracking Detector

Straw Tube detector can be used with a spatial resolution of about 200 mm in a large volume operating under vacuum conditions. Mainly it can reduce the mass of detector and inactive parts in order to decrease straggling and interactions of the particles before they reach further surrounding detectors. The straw tube is a proportional counter. Gas-filled cylindrical tube made of aluminized Mylar as a cathode and 20 μm gold-plated tungsten wire stretched along the cylinder axis as an anode [see figure 3.6a].

When charged particle track passes through the tube ionizes the gas (Ar: Co2) molecules and electrons stripped off drifts towards the wire (anode) as depicted in the figure 3.6b. In the detector excess pressure of 1 bar inside the tubes is used to create the necessary wire tension and mechanical stability. This excess pressure creates an axial force of 7.85 N which is enough to tense the wire and make the tubes self-supporting. This means, that massive frame constructions [86, 87] are no longer necessary to hold the wire tension or to

Table 3.2: Comparison of some material properties of Mylar and Kapton.

	Mylar	**Kapton**
Young's modulus	4.5 N/mm^2	2.4 N/mm^2
Tensile Strength	100 N/mm^2	69 N/mm^2
Permeability Ar	25 cm^3	
Permeability CO_2	240 cm^3	684 cm^3

stretch the straw tubes. Each straw has a mass of less than 2.5 g. The full detector consisting of 3000 straws will have a mass of about 7.5 kg. Tests have showed that the detector is able to work either under vacuum or atmospheric conditions [88]. A further modularity of the detector system allows defective components to be repaired and enable different detector geometry setups like planes, barrels, etc.

The straw tubes consist of long Mylar tubes with a diameter of ∼10mm aluminized on the inner surface. Mylar is the preferred because of its higher Young's modulus and a higher tensile strength compared with Kapton as shown in table 3.2. The endcap holds and centers the anode wire and includes the gas connector. PVC can be used as the endcap material because of its low-density and good gluing properties. The wire is centered with a 1mm thick copper sleeve with an inner hole of 100 mm glued into the endcap.

One problem is the bending of the straws due to the gravitation. One solution is to glue all straws of one double plane together with low viscosity cyanoacrylate glue (Loctite 408). A detector setup made of straw tubes must integrate the gas distributor to provide the straw tubes with the counting gas that will cause the necessary excess pressure and because of the elongation of the straws under excess pressure; a fixed connection is not possible and must be formed as flexible. The detector when put under test has showed that at voltage 2KeV gas amplification of 10^4 is achieved using Fe-55 as source with gas $ArCo_2$ (80:20) [88].

Gas gain in the straw tube can deteriorate and dark current (noise) can increase with a time due to aging effects, namely:

- Deposit of the conductive polymers on the wire surface
- Formation of an insulation coating on the cathode (Malter effect)
- Anode wire swelling by the free radicals
- Oxidation of the conductive layer on the cathode surface

These aging phenomena are typically observed for the accumulated charge values $>$ 1-3 C/cm, depending on the gas mixture. Also, overpressure gives the stability and rigidity to the straw tube, but it also change straw tube dimensions to be taken into account in the tracker design.

3.2.5 Straw Tube Tracker for CBM

The possibility of the Straw tube tracking detector inside MuCh is being explored at GSI Germany and JINR Dubna Russia. A prototype with 360 active anode channels has been developed and tested. The prototype contains two planes of straws glued between themselves. Each plane consists of 48 straws each 400mm long. Each straw contains fourfold- segmented anodes of 100mm length. The anode voltage on each segment and the information read-out were carried out via the segment contacts going through the straw wall. Fig. 3.7 shows the general layout of the prototype with a fragment of the straw plane with the installed flat transmission lines (TL) of about 50 cm length. Each line has 8 buses and is used for 8 segments of two neighbouring straws.

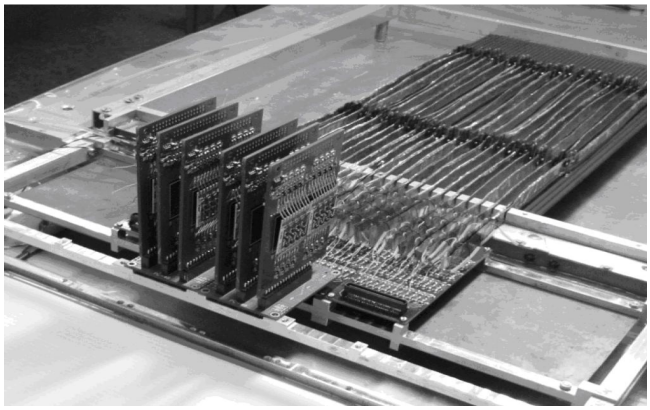

Figure 3.7: General layout of the straw tube tracker prototype with 96 fourfold segmented straws in two layers, the new developed very thin flat flexible cables and FEE-cards

The prototype has been tested with a Fe-55 source at gas gains of up to 10^5. The gas mixture Ar:CO2 (70/30) was used. The leakage current in each channel did not exceed 1 nA. Measurements of the spatial resolution value of the prototype were performed on the SPS test beam H6 at CERN using beam telescope EUDET [89] as track detector and for the prototype spatial resolution of 200 μm was measured [90]. In 2009 straw tube option was added in the present CBM simulation framework which includes integration of the straw tube option in the MuCh library, implementation of the manual segmentation, new features like timing and track matching algorithms, etc [91].

3.3 Large-area GEM at VECC for CBM

As a part of the development effort for building a muon detection system in the CBM experiment in the upcoming FAIR facility at GSI-Germany, VECC group is involved in R&D work on GEM as tracking chambers. In CBM muon

chambers, where tracking will be done inside absorbers, the chambers should cover an area of $20m^2$ working at a rate up to 16 MHz/cm^2. Main goal of this R&D is therefore to develop highly efficient large-size GEM modules to be readout by self-triggered readout system with highly granular pad readout. At VECC so far, several triple GEM modules each of 10cm x 10cm dimensions have been made and tested using radioactive source (Ru-90 and Fe-55), proton beam and cosmic rays. A multi-GEM stack contains a drift meshes and pad readout where GEM foil is stretched using double layer Perspex jigs which on heating foil is stretched and sandwiched between the two layers. Two G10 frames cut to size were glued on wither side of the foil thus producing a framed and stretched GEM mesh ready for testing. For 10cm x 10cm GEM module with a gas mixture Ar:Co_2 (70:30) 90% efficiency was achieved [85] and 8mm x 3.5mm readout pad. The picture of the detector under test is shown Fig. **??**. All the foils were obtained from CERN fabricated by both types of technology e.g. conventional single-mask and recently developed single-mask. Recently GEM-chambers have been tested at CERN with secondaries produced by proton beams hitting a 10-cm iron converter and the response of the detector to charged particles has been studied using 2.3 GeV/c proton beams at GSI and at varying GEM voltages. Main goal is to optimize the granularity of the detector and to determine the operating conditions.

However, based on the simulations and investigations done so far, it appears that the combination of GEM in first few stations and Micromegas/MWPC at the stations with low hit density will be a good choice.

Thick GEM (THGEM)

VECC group has locally fabricated a THGEM (Thick GEM) element using conventional PCB technology involving mechanical drilling of holes. The hole

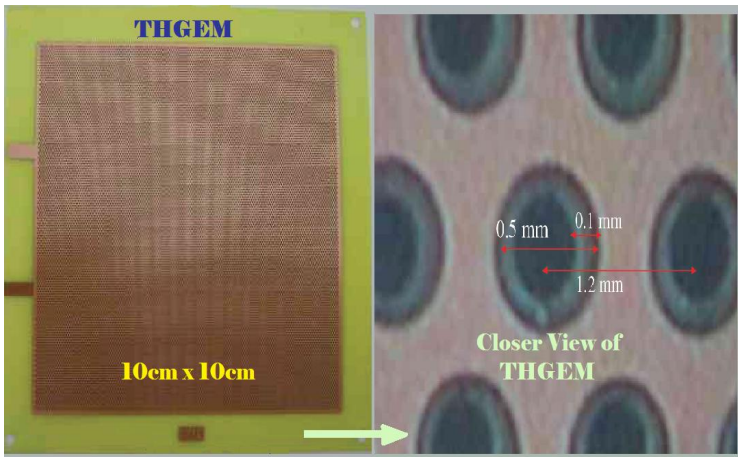

Figure 3.8: (left)THGEM 0.5mm thick double sided copper clad FR4 material hole size is 0.3mm and the pitch is 1.2mm. (right) Closer view of the holes.

has a diameter of 0.3mm while the copper rim around it has a diameter of 0.5 mm, a 10 cm x 10 cm. G10 based PCB was used to drill such holes at a pitch of 1.2 mm. Figure 3.8 shows the close-up of holes in thick GEM.

Extensive studies of thick GEM is to be performed to study the performance of the detector in high density environment i.e. behind an absorber and detector is to be tested using proton beam at GSI so as to study their characteristics with minimum ionizing particles (MIP).

3.4 Geometry and Segmentation

Simulation has been performed on muon detection for different geometries and segmentation schemes and results are discussed in this section. The simulations were performed with the CBM software package *cbmroot*, using *GEANT3* as transport engine and the *UrQMD* model for the generation of background events and *Pluto* for generation of signal events.

3.4.1 Different Geometries

Simulation have been performed for geometries like:

- **Standard (18 layer) geometry :** The Standard geometry consists of 6 iron absorbers and 18 detector layers (possibly made of GEM). The total absorber length in the current design amounts to 2.25 m of iron. The detection procedure is to continuously track all charged particles through the complete absorber, starting with the tracks measured by the Silicon tracker (which defines the momentum). An additional shielding is used around the beam pipe in order to reduce the background of secondary electrons produced in the beam pipe [93].
- **Intermediate(12 layer) geometry :** The intermediate geometry consists of 4 hadron absorber layers (iron plates of thickness 30cm, 30cm, 65cm, and 100cm) and 12 detector layers made of a micro-pattern detector technology known as GEM and is located in triplets behind each absorber. Here the definition of LMVM track is that it should pass through 3 layers of absorber (125cm).
- **Reduced (9 layer) geometry :** The reduced geometry consists of 3 hadron absorber layers (iron plates of thickness 30cm, 95cm, and 100cm) and 9 layers (made of GEM) located in triplets behind each absorber. Here the definition of LMVM track is that it should pass through 2 layers of absorber (125cm).

The signal to background(S/B) and reconstruction efficiency for three geometries was calculated as shown in Table 3.3. It is evident from the tables that

Table 3.3: Reconstruction Efficiency and Signal to Background ratio of ω in central Au-Au collision at 8, 25 and 35 AGeV beam energies (Input events: 10k UrQMD+PLUTO)

E (AGeV)	**Efficiency**			**S/B Ratio**		
	9	**12**	**18**	**9**	**8**	**12**
8	0.94	0.91	0.86	0.05	0.088	1.41
25	1.77	1.95	0.58	0.00098	0.0003	0.49
35	1.85	2.13	1.82	0.00059	0.00162	0.34

different geometries with same absorber thickness but varying number of detector layers give comparable values for the reconstruction efficiency. The S/B ratio, however, is drastically different for the different geometries. Reduction in the number of stations results in a huge reduction of the S/B ratio for ω mesons, even at the lowest energy. Thus simulation studies indicate that as far as the measurement of low-mass vector mesons is concerned, there is practically no cheaper version of the muon detection system other than the standard geometry, which effectively comprises 15 layers for LMVM detection [92].

3.4.2 Segmentation

Each station of the detector is segmented (divided) into smaller detection elements called as '***Pads***'. The study of segmentation is important for
a) The determination of occupancy, which eventually determines the feasibility of tracking and the efficiency of muon measurements
b) The total number of pads, which influences the cost; and
c) The smallest pad size, important from the point of view of fabrication and signal strength.

Minimal (first station) and maximal (last station) pad sizes are listed in Table 3.4. Detector is segmented into pads of varying size from 4×4 mm^2 to 3.2×3.2 cm^2 depending on the radial distribution of particle density.

Reconstructed efficiency and signal to background ratio were calculated for ω (low vector meson) in central Au-Au Collision at different energies as shown in table 3.5. The efficiency does not change significantly for the three different segmentation options, whereas the S/B is reduced by 10% to 40% when going from segmentation option 1 to 3. The increase in S/B from option 1 to option 2, however, is marginal and even reversed at 8A GeV beam energy. It was concluded that a minimal pad size of $4{\times}4$ mm^2 is the preferable option, given the fact that pads of this size are relatively easy to fabricate [94].

Table 3.4: Detector is segmented into pads of varying size depending on the radial distribution of particle density.

Scheme	**min. size(mm^2)**	**max. size(cm^2)**	N_{pads}
1	4×4	3.2×3.2	791,040
2	2×4	3.2×3.2	989,184
3	5×5	3.2×3.2	567,559

Table 3.5: Reconstruction efficiency for ω in central Au+Au collisions at 8A, 25A and 35A GeV beam energies for different segmentations.

E (AGeV)	**Efficiency(%)**			**S/B Ratio**		
	Seg-I	**Seg-II**	**Seg-III**	**Seg-I**	**Seg-II**	**Seg-III**
8	0.86	0.86	0.78	1.41	1.03	0.94
25	1.58	1.61	1.43	0.49	0.497	0.3
35	1.81	1.82	1.7	0.31	0.34	0.28

3.5 Electronics for MuCh

Working with the high-rate front-end electronics is a challenge and the integration of these electronics without large dead space and heat dissipation being worked out. The electronics will have to be radiation hard, and the FEE(Front End Electronics) has to be highly integrated for cost reasons. The general plan in CBM is to design fast Application Specific Integrated Circuits (ASICs) to be used in most of the CBM detectors. CBM collaboration has come up with a *self-triggered* ASIC version of chip having both *analog and digital readout*, named **"n-XYTER"** which has been used for readout as shown Fig. 3.9. n-XYTER is a 128 channel integrated mixed signal front-end ASIC [95, 96]. Every channel is equipped with charge sensitive pre-amplifier and shaper circuitry to asynchronously capture incoming signals of either preset polarity. For every channel, both, analogue pulse height and a digital time stamp are stored in a short *fifo* (first in first out), where it will remain until read out. Data is read out of the *fifos* through a token ring structure, that un-prejudicedly reads out whichever channel has data and skips non-hit channels. It has a fast channel of 20-ns trigger time for time-stamp determination and a slow channel for charge measurement and can readout data with 32MHz rate [97].

The n-XYTER receives analogue data directly from the sensors and detects the value and the exact time of a signal peak. It provides the time stamp digitally and the peak value in analog form. For further processing the analog data has to be converted by an ADC (Analog to Digital converter) into digital data. Since the conversion needs time, the correlation between time stamp and signal value is lost. The correlation needs to be recombined. This, the transfer of the measured data and the controlling of the functional behavior of

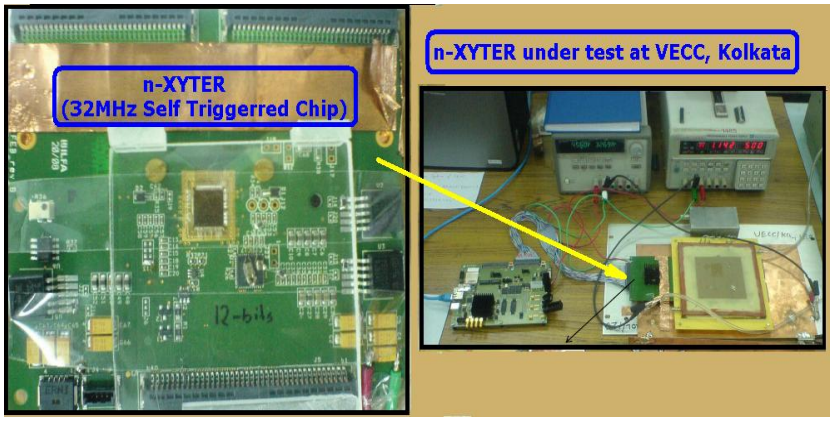

Figure 3.9: (left)n-XYTER for CBM. (right) n-XYTER under test at VECC

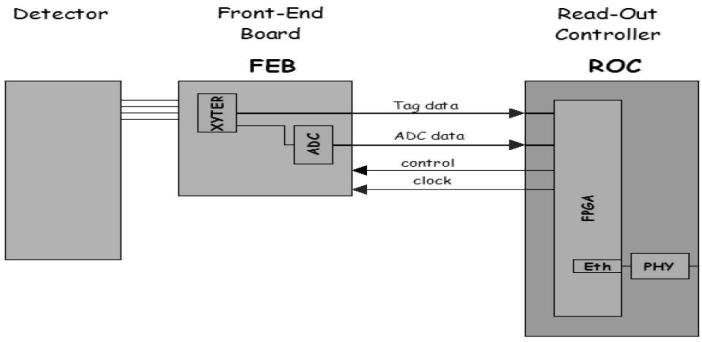

Figure 3.10: The FEE with ROC

the n-XYTER and the ADC is done by the ROC (Read out Controller) Board developed as shown in Fig. 3.10.

One major task of the ROC is the preparation of clock signals for the n-XYTER and the ADC with well defined frequencies and phase relations to each other. This is a very sensitive point, since the ADC converts the data exactly at the rising edge of its clock and the time slot for the conversion is just about 3 ns. At the moment it is possible to change the delay at runtime from 0 ns to 31 ns (full clock cycle is 32 ns) in steps of 1 ns manually [98].

3.6 MuCh Start Version for SIS100

The basis version of the CBM detector system at SIS-100 is designed to perform comprehensive and precise measurements of diagnostic probes of dense matter like multi-strange particles, lepton pairs, charmed hadrons, and their correlations with the bulk particles. The muon detector system can be set up in three

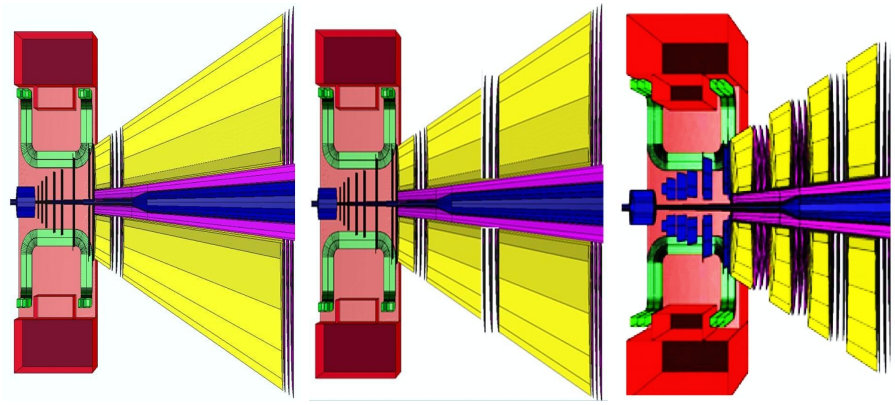

(a) I (b) II (c) III

Figure 3.11: MuCh Start Version for SIS100

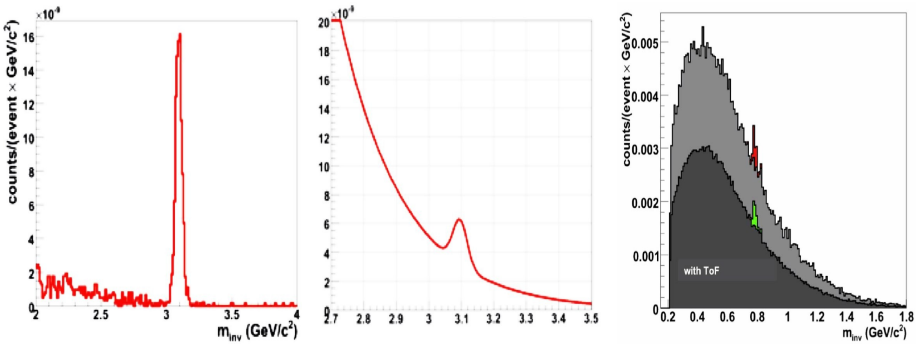

(a) I (b) II (c) III

Figure 3.12: simulated invariant mass spectrum of muon pairs for: (a) p+Au collisions at 25 GeV. (b)Au+Au collisions at 10A GeV. (c) Au+Au collisions at 8A GeV

stages for SIS100 accelerator providing beam energy up to 11 GeV for Au and 29 GeV for protons [62].

3.6.1 MuCh Start Version I

For the detection of charmonium in p+A collisions at SIS-100, two detector triplets are needed (fig. 3.11a). The first station will be constructed from *GEM* detectors; for the last one, the TRD made of *straw tubes* can be used. Simulations of p+Au collisions, with J/ψ decays inserted according to the multiplicity as predicted by the HSD (Hadron-String Dynamics) model, shows that a clean signal can be obtained with this setup. Fig. 3.12a shows the simulated invariant mass of muon pairs in proton(p)- gold (Au) collision at 25 GeV for this geometry [99, 100].

3.6.2 MuCh Start Version II

Setup for the measurement of charmonium in A+A collisions at SIS-100 three detector triplet (see fig. 3.11b) are needed because of high track density environment. The first station will be constructed from *GEM*, second possibly from *Micromegas* and third detector triplet is realised with *straw tubes*. Extra detector triplet is needed in order to correctly match the signals after the absorber with tracks reconstructed in the STS. Simulations of the system Au+Au at 10A GeV demonstrate that even at this sub-threshold energy, the J/ψ is visible above the combinatorial background. Fig. 3.12b shows the simulated invariant mass of muon pairs in Au-Au collision at 10 GeV for this geometry [99, 100].

3.6.3 MuCh Start Version III

Fig. 3.11c shows a muon setup with four detector triplets and 90 cm of iron absorber. This system will be capable to measure low-mass vector mesons through their decay in muon pairs as demonstrated in Fig. 3.12c for Au+Au collisions at 8A GeV. It constitutes a subset of the full detector system to be operated at SIS-300 for the measurement of charmonium and low-mass vector mesons in Au+Au collisions up to 35 AGeV. Fig. 3.12c shows the simulated invariant mass of muon pairs in Au-Au collision at 8 GeV for this geometry[100].

3.7 MuCh Full Version for SIS300

The heavy-ion beams from SIS300 are required for the CBM core research program which is the search for the most prominent landmarks of the QCD phase diagram at high net baryon densities: the first order deconfinement phase tran-

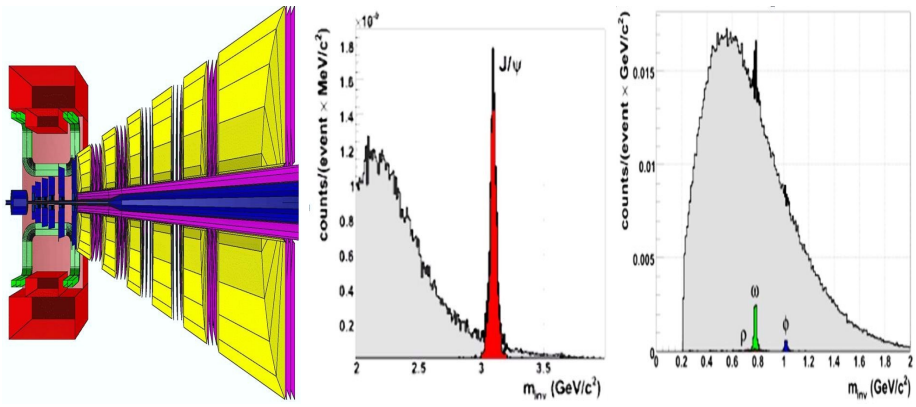

(a) (b) (c)

Figure 3.13: (a) MuCh Full Version for SIS300 (b) & (c) simulated invariant mass spectrum of muon pairs for Au+Au collisions at 25 A GeV

sition, the critical endpoint, equation-of-state of high-density baryonic matter, and the search for modifications of hadronic properties in the dense baryonic medium as signatures for chiral symmetry restoration[62].

Fig. 3.13a shows a muon setup for SIS300 which includes six detector triplets with total iron absorber thickness of 225cm in which first three absorbers have been assumed to have 20cm thickness and fourth, fifth and six absorber with thickness 30cm, 35cm, 100cm respectively. The first two station will be constructed from *GEM*, third and fourth possibly from *Micromegas* and fifth and sixth detector triplet is realised with *straw tubes.* This system will be capable to measure J/ψ (charmonium) and low-mass vector mesons through their decay in muon pairs as demonstrated in Fig. 3.13b & 3.13c for Au+Au collisions at 25A GeV[99].

Chapter 4

Observables in CBM Experiment and Optimisation of Absorber Thickness

The focal point of the proposed Compressed Baryonic Matter (CBM) experiment is to produce and study the super-dense nuclear matter in the reaction volume of the relativistic heavy-ion collisions. The energy range up to 15 GeV/u was pioneered at AGS in BNL. In CBM (second generation fixed target experiment) the energy range from 10 to 40 GeV/u will be scanned for studying observables to explore the QGP.

In this unit I will discuss some of the observables in CBM experiment for exploring QGP. In particular j/ψ as an signature of QGP will be discussed and proposed MuCh(muon chamber) detector for efficient reconstruction of the charmonium via their di-muon decay channel. MuCh consists of several Iron absorber layers sandwiching detector stations, made of `GEM / Micromegas / Straw tubes`, in between and I will present my research work towards the Optimisation of the first absorber thickness.

4.1 Observables in CBM Experiment

In CBM the energy range from 10 to 40 GeV/u will be scanned for studying following observables:

- The equation-of-state(EOS) of strongly interacting matter at high temperatures and high net-baryon densities.

- In-medium modification of hadrons in dense nuclear matter, predicted to be related to the signature of the chiral phase transition.
- Indications of de-confinement phase transition at high baryon densities
- The critical end point providing direct evidence for the phase boundary
- Exotic states of matter such as condensates of strange particles

The approach towards these goals is to measure simultaneously observables which are sensitive to high density effects and phase transitions. In particular, we plan to focus on the investigations of:

4.1.1 In-medium-modifications of low mass vector mesons and open charm

In medium mass modification of low-mass vector mesons(LMVs), i.e. ρ, ω, and ϕ, and of D-mesons (open charm) are expected to occur if chiral symmetry is restored at high baryon density. So, important tool to understand properties of the QGP is study of the spectral shapes of low-mass which can be modified in the medium by partial restoration of chiral symmetry. As a result low mass vector mesons may become lighter and the width may become wider in the hot medium. Fig. 4.1 shows the modifications of the ρ mass distribution at various baryon densities (ρ_B) [77]. According to the calculations shown in the figure, ρ will melt at the highest baryon density. Similar changes in mass or width of the spectral functions are expected for vector mesons, other vector mesons e.g.

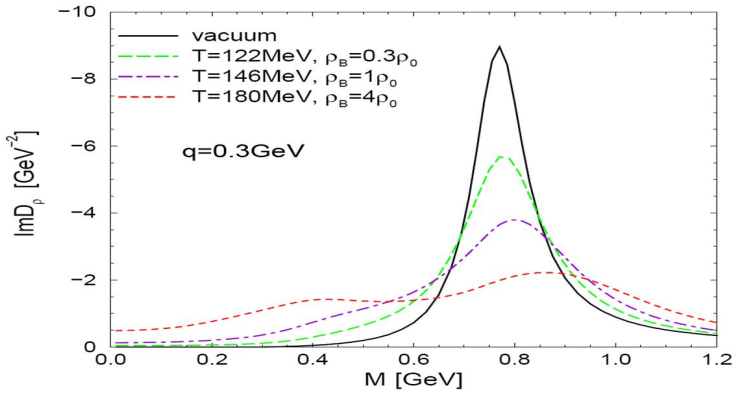

Figure 4.1: Melting of meson in high baryon density matter.

ω. These mesons decay via di-lepton channels, and, therefore, it is absolutely necessary to measure the muons and/or electrons in CBM with large efficiency and with a large signal-to background ratio. Since leptons are not subject to the strong interaction, they do not rescatter on their way out of the medium, which

serve as penetrating probes [77, 103, 104, 105]. The calculations presented in Fig. 4.1 have been performed for conditions which are expected for FAIR and SPS energies. It is found that the mass peak almost vanishes indicating the complete melting of ρ mesons at high baryon densities [172].

A modified in-medium mass of D-mesons (open charm) will influence strongly their production cross section, in particular at threshold beam energies. The in-medium modification of the $D(\bar{D})$ mesons may explain the J/ψ suppression [37] in an hadronic environment, based on the mass reduction of $D(\bar{D})$ in the nuclear medium [106, 107, 108, 109]. As a result modified production cross-section of D mesons will modify the ratio of charmonia/D-mesons, suggesting this to be an important signal [172].

4.1.2 Strange particles and charmonium

In CBM one of the important observable will be baryons (anti-baryons) containing more than one strange (anti-strange) quark, so called multi-strange hyperons. And to search for non-monotonic behaviour of abundance of (multi-) strange particles and charmonium $(J/\psi, \psi')$ as function of beam energy and/or size of the fireball. Such effects are expected when crossing a first order phase transition. Charmonium is suppressed due to the `sequential melting` of charmonium states $(\chi_c, \psi', J/\psi$)in an expanding medium after the deconfinement phase at high baryonic density [102].

4.1.3 Collective flow of all observed particles

Information about the equation of state can be extracted from the collective flow of nuclear matter deflected sidewards from the hot and dense region formed by the overlap of projectile and target nuclei. We will study collective phenomena like `elliptic flow`, both of bulk particles (K, π, p) and of rare probes $(\Lambda, \Xi, \Omega, D, J/\psi)$ as a function of beam energy in CBM experiment. Elliptic flow is regarded as an observable which is sensitive to the very early (possibly partonic) stage of the collision.

It has been predicted using the AMPT (A Multi-Phase Transport Model) transport code that the elliptic flow of hadrons (v2 coefficient) at FAIR energy carries direct information on the partonic phase. The existence of free partons in the initial stage of the collision will enhance the pressure, and, hence, the flow (v2) will be significantly modified as function of the transverse momentum. Fig. 4.2 shows that the inclusion of string melting, which introduces partonic scattering enhances the elliptic flow significantly. The CBM experiment is designed for very high beam intensities in order to measure rare probes such as the

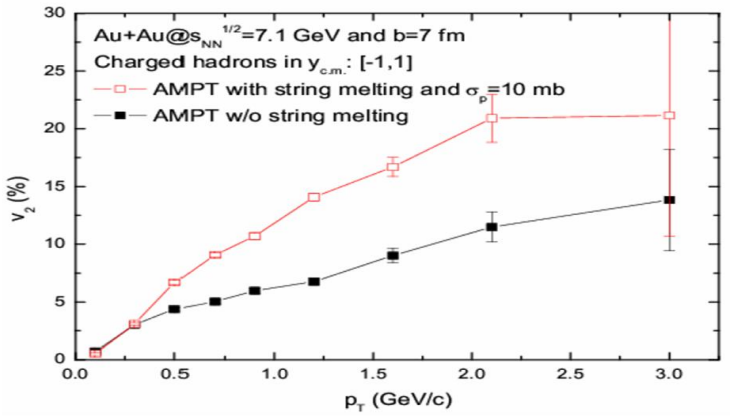

Figure 4.2: Elliptic flow calculated by the AMPT model for semi-central Au+Au collisions at FAIR energies. Open symbols: with string melting. Full symbols: without string melting.

elliptic flow of D-meson and charmonium. These measurements will open a new avenue to explore the details of the initial stage of the fireball evolution [172].

4.1.4 Fluctuations

Lattice QCD calculations predict a smooth crossover transition from hadronic to partonic matter at very low baryon chemical potentials. It is expected that at higher net baryon densities a *critical end point* exist, followed by a first order phase transition [78]. A signature for the critical point in classical systems is *critical opalescence*. In heavy-ion collisions, this phenomenon is expected to cause *fluctuations* in density, various particle yields, charge, transverse momentum, or strangeness in the vicinity of the QCD *critical end point*. Therefore, the most promising signatures are fluctuations in these observables measured event-by-event [53].

The 1st order phase transition is associated with the latent heat, while the cross-over suggests a continuous change in thermodynamic variables. Therefore, the first order phase transition are expected to lead to large fluctuations due to the formation of droplet or more generally density or temperature fluctuations. A large mismatch in baryon density and temperature seems to be a robust prediction for a first-order transition at large baryon density [110].

The CBM experiment will be able to measure a large variety of particles over full phase space which permits to study the fluctuations in detail and with fine binning of beam energy. This capability is necessary for a successful search for the QCD critical endpoint and the first order phase transition.

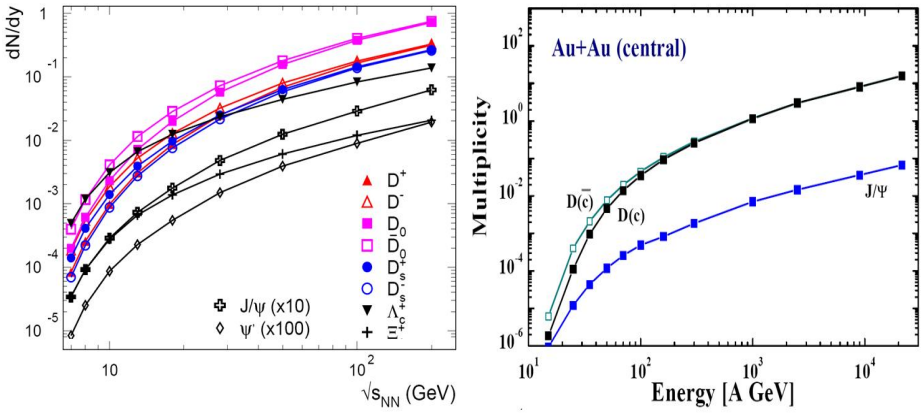

(a) (b)

Figure 4.3: (a) Yields of charm particles as function of beam energy produced by statistical hadronization in the deconfined phase, and (b)produced in a hadronic scenario as predicted by the HSD transport code

4.2 J/ψ as a probe in CBM Experiment

The suppression of charmonium in central nucleus-nucleus(A-A) collisions compared to proton-proton(p-p) or peripheral A-A collisions was predicted to be a signature of the deconfinement as a result of the Debye screening in the quark-gluon plasma [37]. However, it turned out that hadronic models also (e.g the co-mover model) could explain a substantial part of the observed suppression. Lattice QCD calculations predict that different charmonium states dissociate at different temperatures above T_c, leading to sequential melting of J/ψ and ψ' and so on [102].

Recently it was predicted that the relative yields of D-mesons, charmed lambdas(Λ_c) and charmonia depend sensitively on the state of the matter they are produced in. Figure 4.3a depicts the yields of charmed hadrons as function of beam energy as predicted by a statistical hadronization model. In this case the charm(c)- anticharm($\bar{c}$) quark pairs were produced by hard processes in the quark-gluon phase. In Figure 4.3b the excitation function of D-mesons and charmonium is shown as predicted by a hadronic transport code (HSD). In both models the premordial yield of charm-anticharm quarks is identical.

However, the relative yield of charmonium and D-mesons is very different for the two scenarios shown in Figure 4.4. The difference is demonstrated in Figure 4.4a which shows the ratio of J/ψ over D-mesons for the two models. The ratio is clearly reduced for statistical hadronization, indicating a complete melting of the primordially produced charmonium states. Figure 4.4a suggests that the experimental signature for the deconfinement phase transition would be a sudden drop of the J/ψ to D-ratio when increasing the beam energy [111].

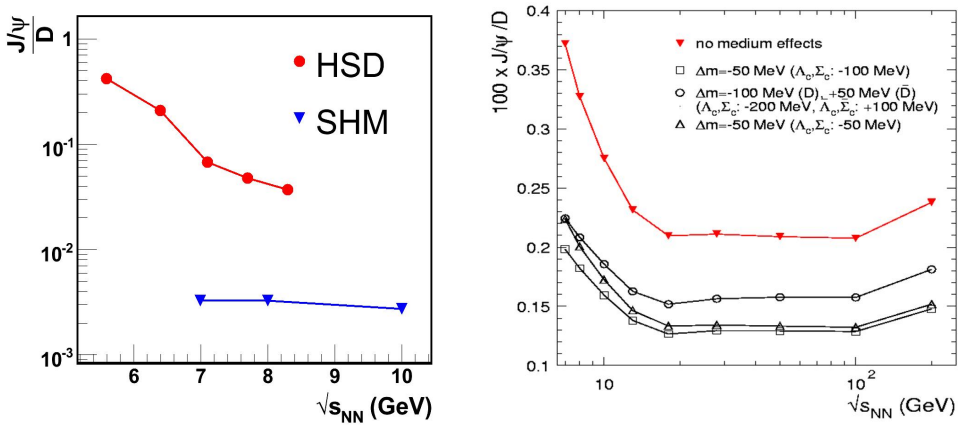

(a) (b)

Figure 4.4: (a) J/ψ to D-ratio as calculated with a statistical hadronization model(SHM) and with a hadronic transport model (HSD) for central Au+Au collisions as function of beam energy. (b)Effect of melting of D-meson on ratio of (J/ψ)/D

At large baryon densities the mass of D-meson is expected to get modified which will result in a change of their yield. This effect has been calculated in the statistical hadronization model and is illustrated in Figure 4.4b. The in-medium modification of the D-meson leads to a further measurable reduction of the J/ψ to D-ratio. At FAIR energies, the production of charmonia is near-threshold which results in very low production cross-sections. In order to obtain charm hadron data with excellent statistics, the CBM experiment will make use of the very intensive heavy ion beams of the FAIR accelerators.

Charmonia as well as low mass vector mesons (ρ, ω, ϕ) can be measured via their *decay in di-muons*. No measurements have been performed so far on dilepton production in heavy-ion collisions in the beam energy range between 2 to 35 AGeV. Thus dilepton data from CBM will be highly welcomed. The production and propagation of charm in heavy-ion collisions is expected to be a particularly sensitive probe of the hot and dense medium. The '*anomalous suppression*' in charmonium production (in addition to '*normal nuclear absorption*' also present in p+A collisions), in heavy-ion collisions, has long been predicted as a 'smoking gun signature' for the formation of color deconfined medium [102]. No data on J/ψ production are available in nucleus-nucleus collisions at beam energies below 158 AGeV. At FAIR charm production will be studied at beam energies close to the kinematic threshold and the production mechanisms of charmonium are expected to be sensitive to the conditions inside the early fireball [172].

4.3 Detection of J/ψ in CBM Experiment

CBM is the only experiment for high energy heavy ion collisions at FAIR, it has been decided to have both electron and muon setup in position to look for the charmonia and low mass vector mesons via dileptonic decay. Electrons will be detected using Ring Imagining Cherenkov(RICH) detection system and muons will be tracked using muon detection system called as Muon Chamber(MuCh). In both cases the Silicon Tracking System will provide track reconstruction and

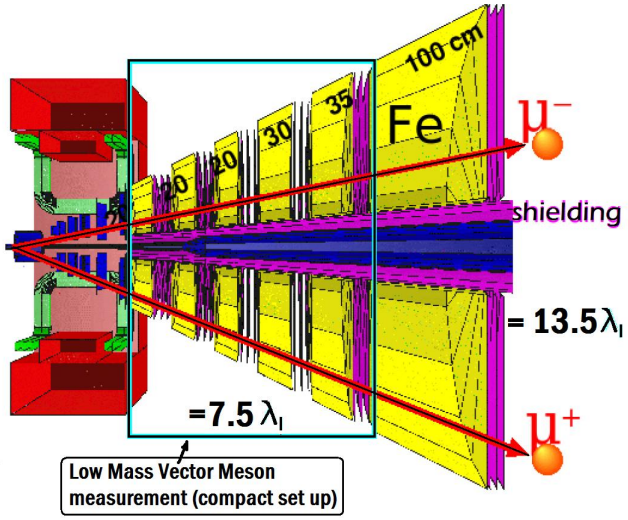

Figure 4.5: CBM muon system (MuCh) configuration with options: (I) 15 stations of total iron thickness 125cm $\sim 7.5\lambda_I$ (interaction length of iron) for LMVM di-muon detection (II) 18 station of total iron thickness 225cm $\sim 13.5\lambda_I$ for charmonium di-muon detection

momentum determination. The muon detection system in CBM experiment consists of several absorbers with the tracking inside the absorber by several tracking stations. The muon detection system is followed by a TOF system for background reduction in muon detection. For hadron runs in this setup, absorbers are to be removed. The muon detection system which will track the particles after STS will consist of series of iron absorbers, for hadron absorption and a number of tracking detectors sandwiched between them. The standard optimized design includes `6 iron absorbers and 18 detector layers` (3 behind each absorber) as shown in Fig. 4.5. The total absorber length in the current design amounts to `2.25 m of iron`. An additional shielding is used around the beam pipe in order to reduce the background of secondary muons produced in the beam pipe.

Simulations are being performed for the optimization of the detector design and to study the feasibility of the di-muon measurement. The feasibility studies are done within the CBM simulation framework [117] which allows full event

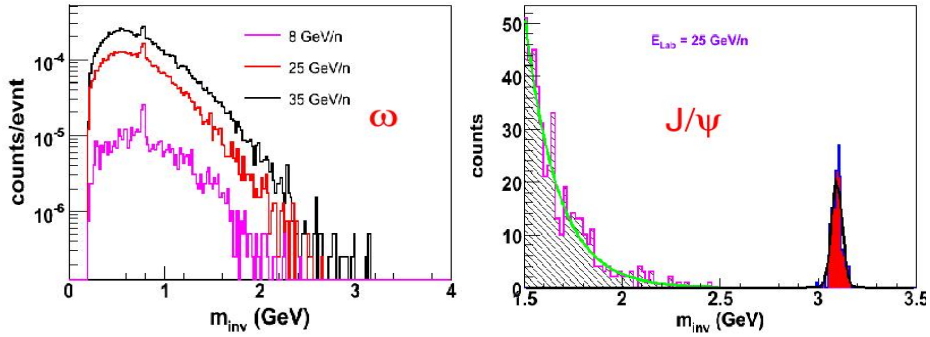

(a) (b)

Figure 4.6: (a) Invariant mass spectrum of ω for central Au+Au collisions at 8, 25 and 35 AGeV beam energy (b) Invariant mass spectrum of J/ψ for central Au+Au collisions at 25 AGeV beam energy

simulation and reconstruction. The ingredients used for the simulation are :

1. PLUTO [101] event generator for phase space decay of the vector mesons taking multiplicities from HSD [113].
2. UrQMD [118] event generator for background particles.
3. GEANT3 [120] for transport of the particles through the setup.
4. Kalman Fitter (KF) for tracking.

LMVM muons travel shorter distances [= 125 cm of total iron thickness ~7.5 λ_I(interaction length)], J/ψ muons cross the thick absorber(= 225 cm of total iron thickness ~13.5 λ_I) and reach till the end as depicted by Fig. 4.5. We can therefore take tracks travelling through 15 layers and 18 layers as valid muon candidates from LMVM and charmonia respectively.

In simulation detector has been segmented into pads of varying size from 4mm×4mm to 3.2cm×3.2cm depending upon the radial distribution of particle density. The reconstruction efficiency and signal to background ratio of ω and J/ψ for central Au-Au collisions at 8, 25 and 35 AGeV beam energies were calculated. Figure 4.6 shows the invariant mass spectra of ω and J/ψ via di-muon channel. The combinatorial background is calculated using Super Event (SE) Analysis technique where tracks having opposite charges from different UrQMD events are combined. Studies indicate that both low mass vector mesons and charmonia can be identified above the combinatorial background which is dominated by muons from weak pion decays. Tungsten shielding is used around the beam pipe in order to reduce the background of secondary muons produced in the beam pipe [114, 115].

4.4 Absorber System

J/ψ has a very low multiplicity at central Au+Au collisions at CBM energy. For example, at 25 AGeV beam energy, the multiplicity is 1.95 $\times 10^{-5}$. And the branching ratio of J/ψ decaying into dimuon channel is $\sim$5%. So, their detection requires an extreme interaction rate. For example, to detect one J/ψ through its decay into di-muons it requires around 10^8 collisions. Our detector should be able to detect the charmonium with maximum efficiency. In muon detection system, hadron absorbers(iron) with intermediate detector layers for momentum dependant muon detection. Momentum is measured at STS only. Space coordinates are matched before and after each absorber and with reconstructed track in STS. Absorber is considered with two contradictory requirement:(I) *absorption of pions, kaons etc. and secondary electrons and minimizing probability of production of hadron-shower.*(II) signal muons pass through and get detected after absorber. Hadron *punch-through* contribution can be minimized by *tracking before and after absorber* and *momentum measurement before and after absorber* (as done in NA60 experiment). To reduce the effect of secondary electrons in tracking signal muon, air gap is employed between absorber and detector and number of detectors planes after absorber are increased. Main purpose of the absorber system is to suppress the background particles (esp. hadrons etc.). Material and thickness of the absorber is investigated for their optimisation. Tungsten, Iron, Carbon are tried in simulation for absorber.

Hadrons travelling Iron modules continuously looses its energy. In case of low energy muons , the energy loss has two components: one which is fairly constant (i.e. ionisation) and one which has large fluctuations (bremsstrahlung and pair creation) called as stochastic fluctuations represented by poisson distribution. The later has negligible contribution for muons below 10 GeV. As the result of constant energy loss muon track curves more in a given field, hence the *sagitta* of a track with a given momentum becomes larger. Radiative energy loss leads to infrequent, but large deposits along the muon track which is to be taken account in the track fitting algorithm. The radiative energy losses are of electromagnetic nature, their typical values will be up to 1-5 GeV. For CBM energy range, muons loose energy mainly via ionisation.

The Absorber is itself an important source of fake muons, produced by decaying pions and (most importantly) kaons generated in hadronic shower development in the absorber material. Apart from the heavy flavour(charmonium), three main *background sources* are contributing to the single-muon p_T distribution:

1. Muons from the decay-in-flight of light hadrons produced at the interaction point called decay muons.

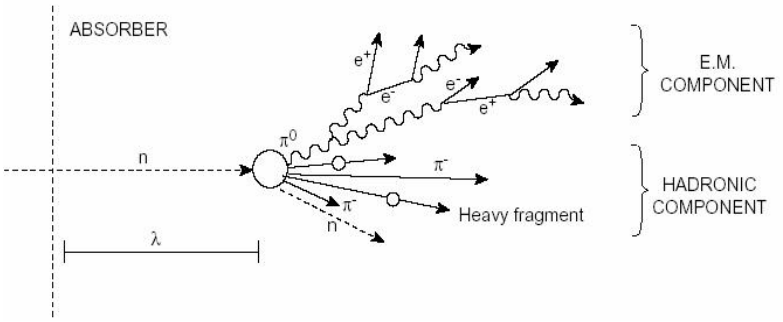

Figure 4.7: Hadronic and Electromagnetic shower inside the absorber.

2. Muons from the decay of hadrons produced in the interaction with the front absorber, called secondary muons.
3. The last source of background are the punch-through hadrons arriving at the tracking chambers without being stopped in the absorber.

This last contribution can be rejected by requiring that the reconstructed track reaches the trigger stations placed behind the iron wall, leaving hits in at least three chambers out of four. In the analysis, muons are required to have p_T greater than 2 GeV/c thus removing most of the background which has a softer p_T distributions. With such a cut, the contribution from secondary muons is reduced to about 3%. About 25% of the remaining background originates from decaying muons and can be subtracted by means of simulations.

In passing through matter(absorber), a hadron can build up a shower through multiple interactions, in a similar way as electrons, fast neutral pions and their subsequent rapid decay into energetic photons do in *electromagnetic shower* inside the absorber as depicted by figure 4.7. The shower can be parameterised by a nuclear interaction length, similar to the radiation length for electromagnetic showers. For the inelastic cross section, nuclear interaction length, is a function of both the energy and type of incoming particle. The interaction length of dense materials is much greater than the radiation length, for iron it is about 17 cm.

Muon traversing iron absorber will undergo multiple `Coulomb scattering` and it will deviate from its initial trajectory. These deviations will induce a contribution to the track curvature. The fake curvature due to multiple scattering is inversely proportional to the muon momentum, there fore its contribution to the momentum resolution is independent of the track momentum. Multiple scattering also introduces correlations between measurements. Proper treatment of these correlations in the fit is necessary to attain optimal momentum resolution by using a total measured track length and to reduce non-gaussian

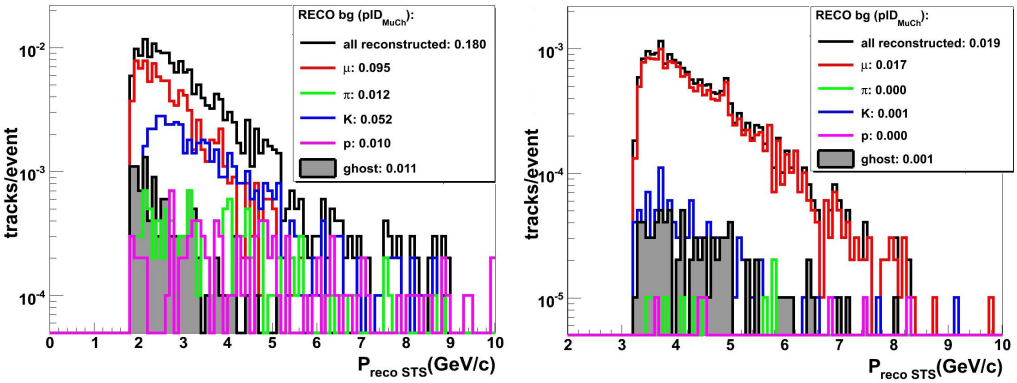

(a) (b)

Figure 4.8: Reconstructed background tracks per event simulated for central Au+Au collision at a beam energy of 25 AGeV. The integrated yields of the different background contributions are given. The calculations are performed for a total iron absorber thickness of (a) **1.25 m** and (b) for a thickness of **2.25 m**.

tail in the momentum resolution.

4.5 Optimisation Of Absorber thickness for MuCh

The experimental challenge for muon measurements in heavy-ion collisions at FAIR energies is to *identify low momentum muons* in an environment of high particle densities. *The CBM concept is to track the particles through a hadron absorber system, and to perform a momentum dependent muon identification.* This concept is realized by *segmenting the hadron absorber in several layers*, and *placing triplets of tracking detector planes in the gaps between the absorber layers.*

Performance of the CBM muon detection system have been studied by analysing the reconstructed particle tracks which pass the absorbers. The simulations were performed for a total iron absorber thickness of *1.25 m of iron* which is used for the measurement of muons from low-mass vector mesons, and for a thickness of *2.25 m of iron* used for charmonium measurements. The results are presented in Fig. 4.8 which depicts the composition of reconstructed particles per central Au+Au collision. For the thin absorber in total about 0.2 tracks are reconstructed per event, the dominating contribution (about 50%) are muons from weak decays which are wrongly matched to the tracks of their mother particles. For an absorber thickness of 2.25 m only 0.02 tracks are reconstructed per event, 90% of them being muons.

The results for survival probability of muons from vector meson decays in comparison to hadrons is presented in Fig. 4.9a shows that high energetic muons from decay of J/ψ mesons penetrate the absorber almost without any losses.

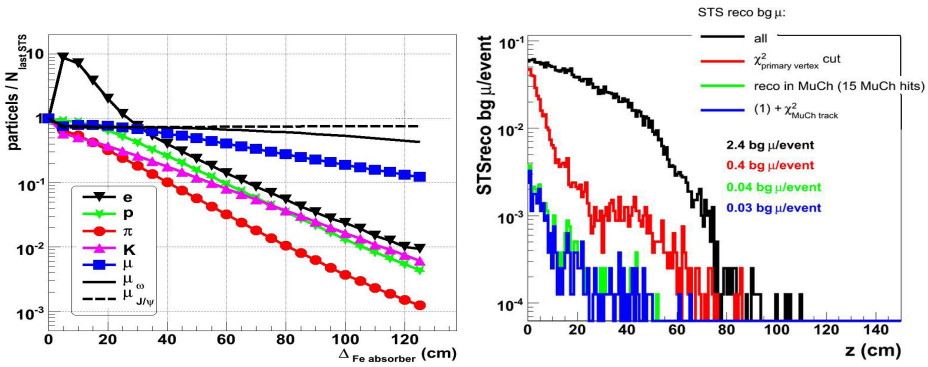

(a) (b)

Figure 4.9: (a) Particle multiplicity behind an iron absorber as function of absorber thickness simulated for central Au+Au collisions at 25 AGeV. The muons from weak decays are labelled as μ. and number of particles are normalized to their respective yield in front of the absorber. (b)Production vertex in z-direction of secondary muons reconstructed in the STS (central Au+Au collision, 25 AGeV); from top to bottom: all (black), muons surviving the χ_2 cut for selecting those from the target (red), muons reconstructed in the muon detector (green) and surviving a χ_2 cut on the track quality in the MuCh detector (blue).

The muons from ω meson decays are absorbed stronger, but still not as much as the hadrons. The simulations demonstrate that for *absorber layers thicker than 1 m the remaining background is completely dominated by muons from weak meson decays.* In order to suppress this contribution, the muon detection system should be as close to the target and as compact as possible. The particle multiplicity is dominated by the yield of secondary electrons, which rises steeply up to an absorber thickness of about 5 cm and then drops with increasing material thickness.

The background contribution from muons from weak decay is surprisingly small as compared to the 800 charged pions produced in the collision. The reason is that most of the weak pion and kaon decays are recognized (and rejected) by the track reconstruction routines of the STS. This is illustrated in Fig. 4.9b where the number of muons from weak decays is shown as function of the z-position of the decay vertex. It turns out that in average 2.4 muons from weak decays are reconstructed per event in the STS, and only 0.4 muons survive the cut on the primary vertex. These muons stem from decays which happen shortly downstream of the target, and, hence, their tracks are perfectly reconstructible in the STS. The first STS station is located 30 cm downstream of the target. as possible.

The kaons and protons with punch through the absorber can by further rejected by a condition on their time of flight. This information can be obtained from the TOF wall for the J/ψ analysis where the full absorber (2.25 m iron) is required. For the detection of muons from low-mass vector mesons an addi-

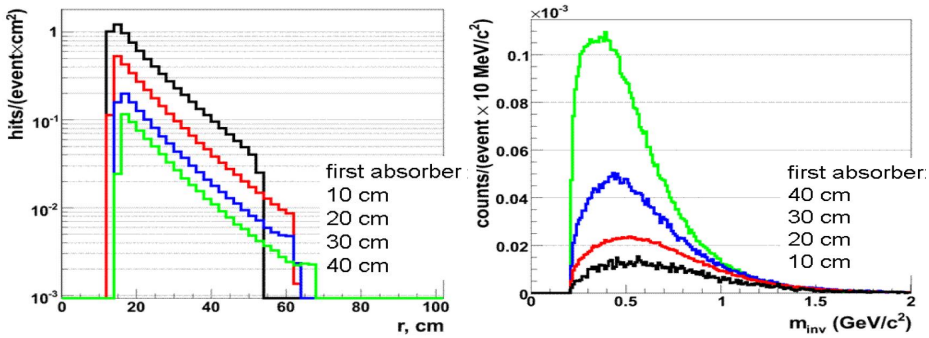

(a) (b)

Figure 4.10: (a) Number of hits per event radially for different thicknesses of the first absorber.(b) Invariant-mass spectra of reconstructed background tracks.

tional RPC-TOF detector can be installed in front of the last iron block of 1 m thickness. The additional condition on time-of-flight reduces the efficiency for the signal, but increases the signal-to-background ratio [62, 116].

The particle multiplicity varies also strongly with the radial distance from the beam as shown in Fig. 4.10a for different absorber thicknesses. This effect is important for the segmentation of the tracking chambers into pads, which may vary in size by more than one order of magnitude from the inner to the outer area of the detector.

In simulation, influence of the thickness of the first iron absorber on the track reconstruction performance have been analysed. The results are shown in Fig. 4.10b for different thicknesses of the first absorber layer. It turns out that the background increases by almost one order of magnitude when increasing the thickness of the first absorber layer from 10 cm to 40 cm. In summary, a first iron absorber of 20 - 30 cm thickness seems to be the best compromise between hit density and background tracks [116].

Chapter 5

CBM Simulation tools and feasibility studies

The framework for simulation in CBM (cbmroot) is based on ROOT, the object-oriented framework developed at CERN(European Organization for Nuclear Research) to meet challenges in data analysis for High-Energy Physics Experiments. The cbmRoot simulation framework [117] has been developed for feasibility studies and optimization of the detector layout. As an event generator, UrQMD(ultra-relativistic quantum molecular dynamics) [118] code is used. This code does not include rare probes as e.g. the vector mesons and charmed hadrons, therefore their multiplicities are implemented using the HSD(Hadron-String Dynamics) [119] model. For feasibility studies the rare probes are then added on top of the UrQMD events with kinematic distributions also guided by HSD. Vector mesons decaying into dileptons are embedded using the PLUTO generator [101]. Particles are propagated through a CBM detector using the transport code GEANT [120]. VMC (Virtual Monte Carlo) is included in the framework which allows running different simulation Monte Carlo without changing the user code and therefore the input and output format as well as the geometry and detector response definition. Simulated events are reconstructed using different track and ring reconstruction routines as well as secondary vertex finding algorithms. For particle identification RICH, TRD and TOF information is combined for the single tracks. The schematic design of CbmRoot is shown in Fig. 5.1.

In this Chapter we will give brief introduction about the different simulation tools used in the CBMRoot framework and then we will present some feasibility studies based on the simulation.

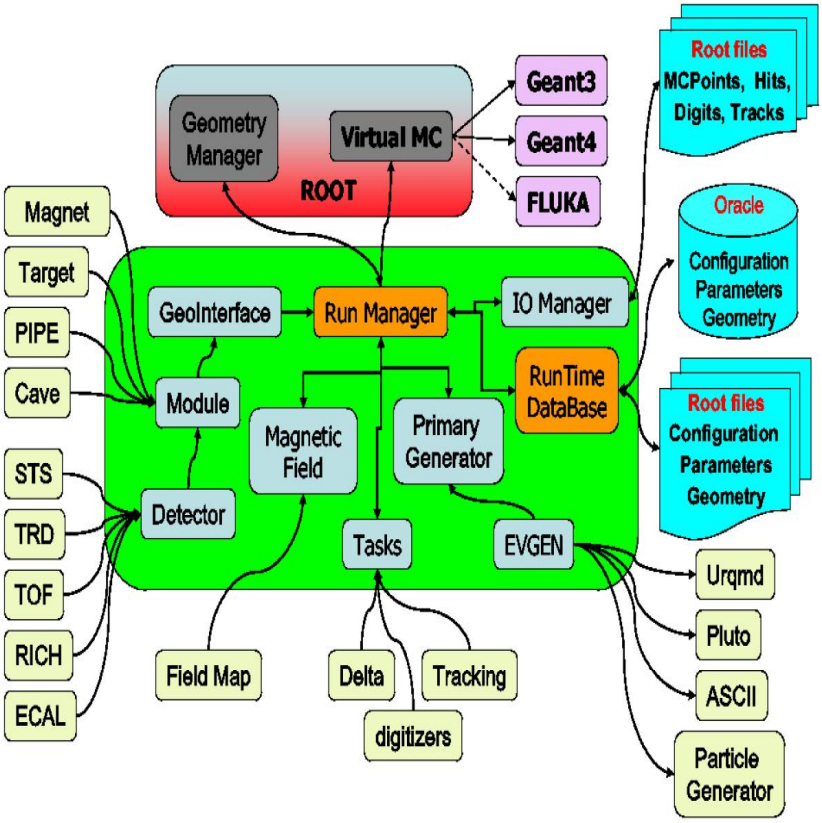

Figure 5.1: CBM Simulation Frame Work

5.1 Basic Functionality of CBM simulation framework

The CBM simulation framework, shown in Fig. 5.1, delivers a set of base classes which enable the users to construct their detectors and/or analysis tasks in a simple way. The main class is the `run manager` class. Using standard ROOT macros, users can control the run manager class to define global steering parameters controlling the functionality of tasks and also the functionality of the whole framework. These input parameters are set before runtime. The run manager includes methods to set the different:

- input/output files
- primary event generators
- monte carlo transport engines
- material and geometry definition
- magnetic field map definition

- active and inactive detectors
- tasks configuration parameters

and also delivers some general functionality like track visualization.

The monte carlo application class in FairRoot uses the services of the ROOT virtual Monte Carlo Application interface (class TVirtualMCApplication) to define the actions at each stage of the simulation run [122]. These actions are:

- geometry construction
- geometry initialization
- storage of primary track in an external stack container
- pre-tracking action
- stepping action and dispatching the hit processing to individual sensitive detectors.
- post-tracking action

5.1.1 Input/Output Procedures

The storage of all information collected by the different sensitive detectors is done on event by event basis (an event means in this context one interaction between one beam particle and the target). All persistent objects are serialized and stored into binary ROOT files. The ROOT file structure is then used as a transient data storage where objects are referred with unique keys. An interface class *MCPoint* is provided to define the structure of a registered hit in a detector. Each detector can then provide a more specific implementation following the MCPoint API (application program interface). All registered hits will be collected into dedicated lists, one list corresponding to one detector entity. The ROOT class *TTree* is used to organize the output data into a *ntuple*-like data structure. In the event reconstruction case the *IOManager* provides methods to read this information. A partial input/output mechanism is also supported. It enables the user to switch on/off the streaming of subset of the ntuple data structure when reading the files. The functionality is particularly relevant when dealing with huge ntuples [121, 122].

5.1.2 Parameter handling

Several numerical parameters are needed while analysing the simulated data. So, it is necessary to have a parameter repository with a well-defined versioning system. The runtime database (*RuntimeDb* class) is such a repository. The runtime database is not a database but a parameter manager. It knows the inputs/outputs (I/Os) defined by the user in the steering macro and all parameter containers needed for the actual event reconstruction. It manages the

automatic initialization and saving to an output and contains a complete list of runs and related parameter input and output versions. It is represented by the class *RuntimeDb* and instantiated in the constructor of the *run manager* class [121, 122]. It holds two lists: the list of parameter containers, and the list of runs and related parameter versions. The containers can be initialized automatically from one or two inputs, and written out to one output. Possible inputs/output are:

- Oracle Database
- Root file
- ascii file

In the ROOT, file parameter containers are stored as *objects*. Every time an object is written it gets automatically a new version incrementing the former version by 1. By default the *Read()* or *Find()* functions provided by ROOT read the object with the highest version. A retrieval of another version is possible by adding version number to the name of the parameter container. The information which run corresponds to which version of each parameter container must be stored in the ROOT file together with the data [122].

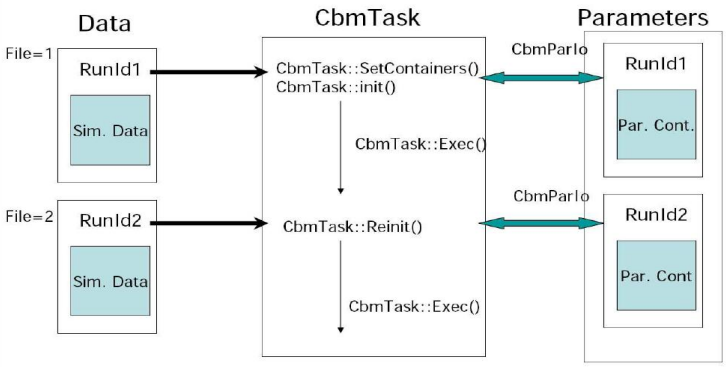

Figure 5.2: Initialization schema.

While the event reconstruction, parameters are initialized. Each task needs special sets of parameters which are stored in container classes. Some tasks might share the same container. The parameters are valid for very different time scales. Once a detector is built, some parameters are fixed for the whole lifetime of this detector (e.g. number of wires in a given layer of a drift chamber). Containers holding such data must be initialized only once for the event reconstruction. Some parameters might change seldom, others quite often. In these cases, a re-initialization might be needed during the analysis of several event files. A task might change parameters during the reconstruction of an

event file and it is then necessary to save these data before a reinitialization. All initialization data are managed by the runtime database which can be saved in a ROOT file for further use. Figure 5.2 shows the initialization schema used to connect the different parameters with data [121, 122].

5.1.3 Algorithm implementation

In event reconstruction, for each event we need to accomplish various tasks or reconstruction algorithms. The *Task class* is an abstract class defining a generic API (application program interface) allowing to execute one task and to navigate through a list of tasks. The user can create his own algorithm inheriting from Task. Each task defines the relevant input data and parameter and creates its particular output data during the initialization phase. During the execution phase, the relevant input data and parameters are retrieved from the input file and the output data objects are stored in the output file [121, 122].

5.1.4 Testing and Configuration

CMake/CTest is used for configuration and automatic testing in CBM framework [123]. *CMake* is a cross-platform, open-source make system used to control the software compilation process. It generates native *makefiles* and *workspaces* that can be used in the compiler environment of user choice. The testing system (*CTest*) creates information on client machines, which defines a build snapshot of the software at a given time, then sent to a central server using standard internet protocols. The server produces concise dashboards that link to detailed reports on inter- and intra- configuration results, summarizing the current state of a software system. Testing results are tracked over time, allowing developers to trace the history of development. Moreover, CTest also provides the way to share build results with other developers before committing [122].

5.2 ROOT

The ROOT system provides a set of object oriented(OO)frameworks with all the functionality needed to handle and analyze large amounts of data in a very efficient way. Having the data defined as a set of objects, specialized storage methods are used to get direct access to the separate attributes of the selected objects, without having to touch the bulk of the data. Included are histograming methods in an arbitrary number of dimensions, curve fitting, function evaluation, minimization, graphics and visualization classes to allow the easy setup of an analysis system that can query and process the data interactively or in

batch mode, as well as a general parallel processing framework, PROOF, that can considerably speed up an analysis.

ROOT has built-in CINT C++ interpreter the command language, the scripting, or macro, language and the programming language are all C++. The interpreter allows for fast prototyping of the macros since it removes the, time consuming, compile/link cycle. It also provides a good environment to learn C++. If more performance is needed the interactively developed macros can be compiled using a C++ compiler via a machine independent transparent compiler interface called ACliC.

The system has been designed in such a way that it can query its databases in parallel on clusters of workstations or many-core machines. ROOT is an open system that can be dynamically extended by linking external libraries. This makes ROOT a premier platform on which to build data acquisition, simulation and data analysis systems. ROOT can handle large scale data analysis and simulation and at the same time had incorporated progress made in computer science over the past 15 to 20 years. Especially in the area of Object-Oriented design and development. ROOT is available under the LGPL(Lesser General Public License) license

ROOT was first used project in the context of the NA49 experiment at CERN which generates about 10 Terabytes of raw data per run (same rate as expected in LHC experiment). Currently the emphasis of ROOT is on the data analysis domain and incorporates approach of loosely coupled object-oriented framework so that system can easily be extended to other domains, like simulation, reconstruction, event displays and DAQ.

5.3 GEANT

Geant is a toolkit for simulating the passage of particles through matter (detector). It includes a complete range of functionality including *tracking, geometry, physics models* and *hits*. The physics processes offered cover a comprehensive range, including *electromagnetic, hadronic* and *optical processes, a large set of long lived particles, materials* and *elements*, over *wide energy range*. It has been designed and constructed to expose the

physics *models utilised*, to handle *complex geometries*, and to enable its easy adaptation for *optimal use* in different sets of applications. It was designed and developed under the CERN R&D project (RD44) [124, 125, 126, 127] from the end of 1994 through 1998. Figure 5.3 shows the top level categories and illustrates flow of dependencies. Categories at the bottom are used by virtually all higher categories and provide the foundation of the toolkit which include the category. *global* covering the system of units, constants, numerics and

random number handling. *Materials, particles, representation, geometry* including the volumes for detector description and the navigation in the geometry model. *Intercoms* provides both a means of interacting with GEANT4 through the user interface, interface between the independent modules and repository of abstract interfaces for plug-ins. The *track* category contains classes for tracks and steps, used by *processes* which contains implementations of models of physical interactions. One such processes called *transportation* handles the transport of particles in the geometry model and allows the triggering of parameterisations of processes. All these processes can be invoked by the '*tracking*' category which manages their contribution to the evolution of a tracks's state and undertakes to provide information in sensitive volumes for *hits* and *digitisation*. *Event* category manages events in terms of their tracks and *run* manages collections of events that share a common beam and detector implementation. A *readout* category allows the handling of "*pile-up*". Finally capabilities that use all of the above and connect to facilities outside the toolkit are provided by the *visualisation, persistency* and (user) *interface* category [128].

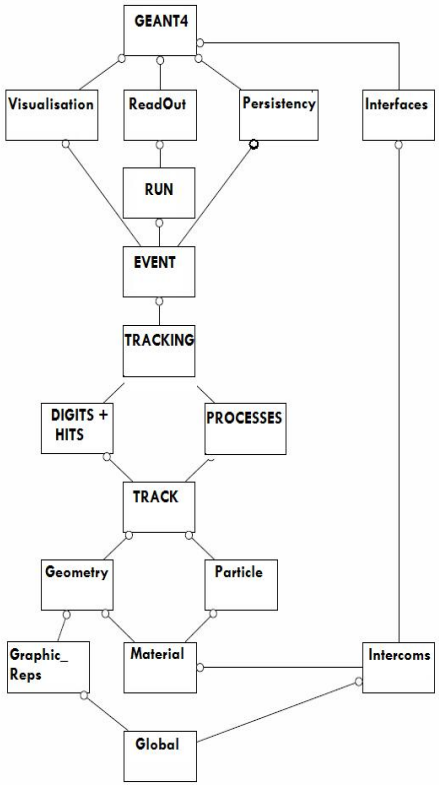

Figure 5.3: Top Level Category Diagram of GEANT4 toolkit.

First production version of GEANT was released in December of 1998. After this release, major HEP laboratories and experiments over the world formed a new international collaboration Geant4, which is based on the Memorandum of Understanding (MoU). This new Geant4 collaboration has a responsibility to maintain the production phase of the toolkit [128].

5.4 UrQMD event generator

Perturbative quantum chromodynamics (pQCD) can be applied to describe hard processes, i.e. processes with large four-momentum, Q^2, transfer. But pQCD is formally inappropriate for the description of the soft interactions because of the absence of the large Q^2-scale. Therefore, low-p_T collisions are described in terms of phenomenological models. A vast variety of models for hadronic- and

nuclear collisions have been developed which can be subdivided into:

- **Macroscopic models:** In the hydrodynamical (thermal) model one assumes local (global) equilibrium - the dynamics is characterized by the equation of state employed. Examples include *statistical* and *hydrodynamical* models [149, 150, 151, 152, 153].
- **Microscopic models:** The microscopic models describe subsequent individual hadron-hadron collisions which include *string-, transport-, cascade-*, etc. models like UrQMD [118], FRITIOF [154], VENUS [155], QGSM [156], RQMD [157] and others [158, 159, 160, 161, 162, 163] including the parton cascade approach [135].

UrQMD is a microscopic many body approach to p+p (proton-proton), p+A (proton - nucleus) and A+A (nucleus - nucleus) interactions at relativistic energies and is based on the covariant propagation of color strings, constituent quarks and diquarks accompanied by mesonic and baryonic degrees of freedom. Furthermore it includes rescattering of particles, the excitation and fragmentation of color strings and the formation and decay of hadronic resonances. Moving to higher energies more sub-hadronic degrees of freedom are available and the treatment of these is of prime importance. In the current version of UrQMD this is taken into account via the introduction of a formation time for hadrons produced in the fragmentation of strings [131, 132, 133] and by hard (pQCD) scattering via an embedding of the PYTHIA model. This microscopic transport model describes the phenomenology of hadronic interactions at low and intermediate energies ($\sqrt{s} < 5$ GeV) in terms of interactions between known hadrons and their resonances. At higher energies,$\sqrt{s} > 5$ GeV, the excitation of color strings and their subsequent fragmentation into hadrons dominates the multiple production of particles in the UrQMD model. The leading hadrons of the fragmenting strings contain the valence-quarks of the original excited hadron. In UrQMD they are allowed to interact even during their formation time, with a reduced cross section where the reduction factor is defined by the additive quark model, thus accounting for the original valence quarks contained in that hadron [129, 118]. Those leading hadrons therefore represent a simplified picture of the leading (di)quarks of the fragmenting string. Newly produced (di)quarks do, in the present model, not interact until they have coalesced into hadrons however, they contribute to the energy density of the system. A more advanced treatment of the partonic degrees of freedom during the formation time ought to include soft and hard parton scattering [134, 135, 136, 137, 138] and the explicit time-dependence of the color interaction between the expanding quantum wave-packets [139].

The UrQMD model has been applied successfully to explore heavy ion reactions from BNL-AGS energies ((E_{lab} = 1A-10A GeV), over CERN-SPS energies (E_{lab} = 20A-160A GeV) up to the full BNL-RHIC energy ($\sqrt{s_{NN}}$ = 200 GeV). This includes detailed studies of thermalization [140, 141], particle abundances and spectra [142, 143], strangeness production [144], photonic and leptonic probes [145], J/ψs [146] and event-by-event fluctuations [147, 148].

5.5 PLUTO event generator

The package "*Pluto*" [164, 101] is geared towards elementary hadronic as well as heavy-ion induced reactions at intermediate to moderately high energies, mainly motivated by the physics program of the HADES [165] experiment, which is installed at the SIS synchrotron of the GSI. It has been used for the simulations in the context of the planned CBM experiment [166] which is going to be operated at the new FAIR facility.

Pluto is a Monte-Carlo event generator designed for hadronic interactions from Pion production threshold to intermediate energies of a few GeV per nucleon, as well as for studies of heavy ion reactions. The package is entirely based on ROOT, without the need of additional packages, and uses the embedded C++ interpreter of ROOT to control the event production. The generation of events based on a single reaction chain and the storage of the resulting particle objects can be done with a few lines of a ROOT-macro. Multi-reaction '*cocktails*' can be facilitated as well using either mass-dependent or user-defined static branching ratios. The included physics uses resonance production with mass-dependent Breit-Wigner sampling. The calculation of partial and total widths for resonances producing unstable particles is performed recursively in a coupled-channel approach. Here, particular attention is paid to the electromagnetic decays, motivated by the physics program of HADES. The thermal model supports 2-component thermal distributions, longitudinal broadening, radial blast, direct and elliptic flow, and impact-parameter sampled multiplicities. The interface allows angular distribution models (e.g. for the primary meson emission) to be attached by the user as well as descriptions of multi-particle correlations using decay chain templates. The exchange of mass sampling or momentum generation models is also possible.

A set of five classes comprise the framework of an event-generator package (Fig. 5.4), and provide additional tools to facilitate principle simulations, such as the possibility to input simple detector geometries and impose geometrical and kinematical acceptance cuts.

A data base of particles at intermediate energies is contained in the class *PData*. It also provides the way for the calculation of spectral functions,

branching ratios of hadronic resonances, the random sampling of masses, total and partial widths, branching ratios, and lifetimes. The *PParticle* class defines "particle" objects and contains functions for handling particle observables. Particle interaction models are implemented in the *PChannel* class. A channel "*object*" represents any single step in a reaction chain, comprising of a parent, a decay model, and the decay products. A succession of channels adds up to a full reaction chain, handled by the *PReaction* class. Through *PFilter* class detector-specific acceptance filters may be imposed. Last, multi-reaction "*cocktail*" calculations are facilitated via the *PDecayManage*r class. A number of basic utility functions are supplied by the *PUtils* class, for elementary operations such as angular-momentum algebra , array sorting, and random-number generation from standard distributions.

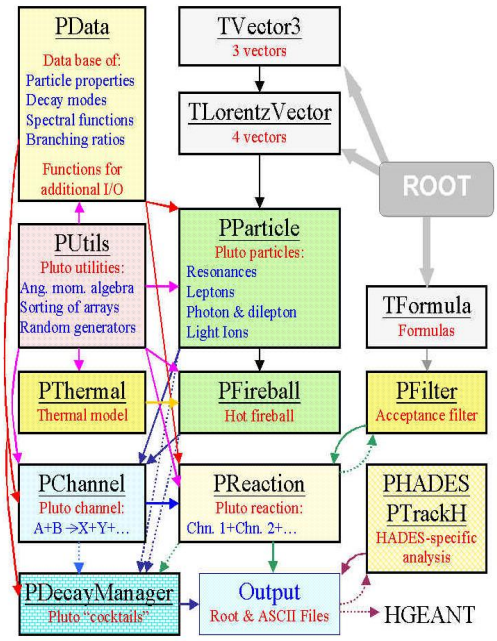

Figure 5.4: PLUTO Class Structure

Software structure of the Pluto event generator [167] originally developed for the HADES experiment [165] but successfully used by other collaborations in the hadronic physics field like new FAIR experiments PANDA [168] and CBM [169, 171]. In CBM The PLUTO event generator model will be generate the signal particles such as the generation of J/ψ , and low mass vector meson as ρ, ω and ϕ and their decays into muon pairs.

5.6 CBM detector feasibility studies

The CBMRoot simulation framework has been developed for feasibility studies and optimization of the detector layout. The UrQMD code is used an event generator which does not include rare probes. Rare probes are implement by using their multiplicities from the HSD model which are then added on top of the UrQMD events with kinematic distributions also guided by HSD. Vector mesons decaying into dileptons are embedded using the PLUTO generator. Particles are propagated through a CBM detector model using the transport code GEANT. For particle identification RICH, TRD and TOF information is combined for

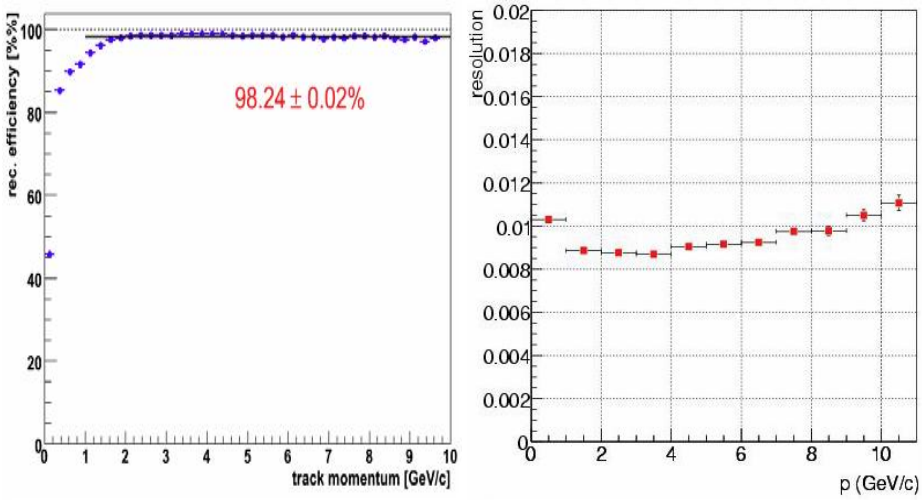

(a) (b)

Figure 5.6: (a) Reconstruction efficiency and (b) relative momentum resolution in the STS obtained for central Au+Au collisions at 25 AGeV with the CA track finder

the single tracks. The feasible measurements of different reconstructed particles are discussed in the following subsections.

5.6.1 Hyperons At STS

The central tracking detector in the CBM experiment is the STS. In order to optimize the STS layout, simulations of central Au+Au collisions have been performed to produce the highest track densities envisaged for the experiment. The simulated tracks of a central Au+Au collision at 25 AGeV are shown in Fig. 5.5. The simulated tracks are reconstructed with a Cellular Automaton algorithm and a Kalman Filter. The resulting track reconstruction efficiencies and the momentum resolution are shown in Fig. 5.6. About *95% of all primary tracks are reconstructed*. The relative *momentum resolution [Fig. 5.6b] is about 1%*, slightly dependant on momentum. This performance fulfills the requirements imposed by the observables to be covered by CBM. Even without hadron identification, the measurement of hyperons via

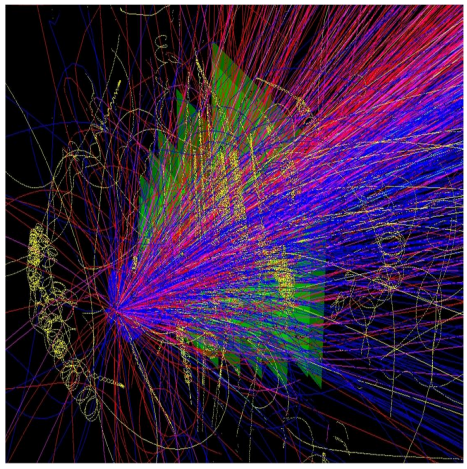

Figure 5.5: Particle tracks in the STS simulated for a central Au+Au collision at a beam energy of 25 AGeV.

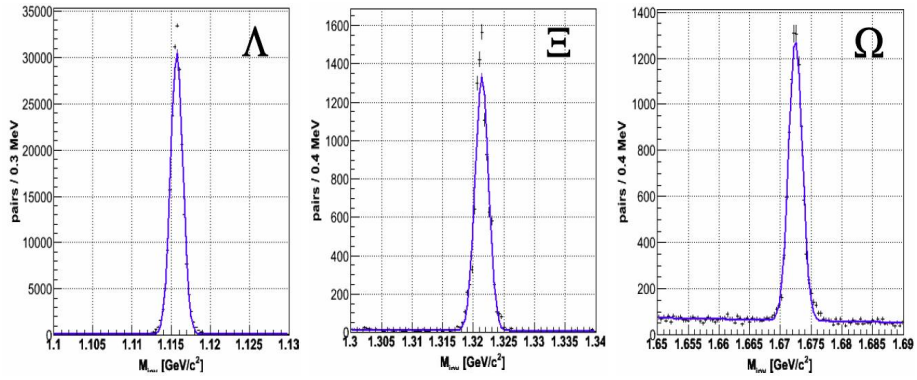

(a) (b) (c)

Figure 5.7: Invariant-mass signals for Λ, Ξ and Ω baryons reconstructed in STS simulated at central Au+Au events on 25 AGeV.

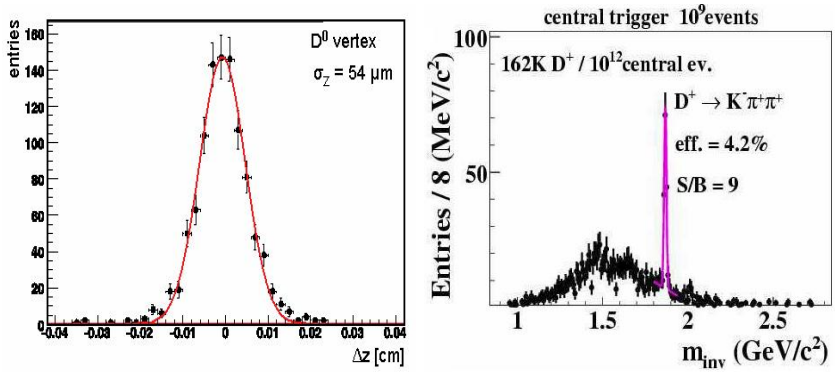

(a) (b)

Figure 5.8: (a) Distance between reconstructed and true vertex of $D^0 \to \pi^+ K^-$ embedded into simulated central Au+Au events at 25 AGeV. (b) Reconstructed invariant-mass spectrum for the decay $D^+ \to \pi^+ \pi^+ K^-$

their weak decay topology is possible with STS information only, as shown in Fig. 5.7. By reconstruction of the decay vertex, Λ, Ξ *and* Ω *baryons* are detected almost background free with good acceptance and efficiency [62, 171].

5.6.2 Open Charm At MVD

Charm production and propagation is expected to be sensitive to the conditions in the early stage of the collision. The experimental challenge is to identify the very rare D -mesons or even Λ_c -baryons via their hadronic decay modes. Micro-Vertex Detector (MVD) is used to precisely determine the secondary decay vertex of particles with open charm. The obtained secondary vertex resolution of 50-60 μm enables the detection of D^0 ($c\tau$ =123 μm) and $D^{\pm}$ ($c\tau$ = 312 μm) as shown in Fig. 5.8 for the latter case. The measurement of Λ_c,

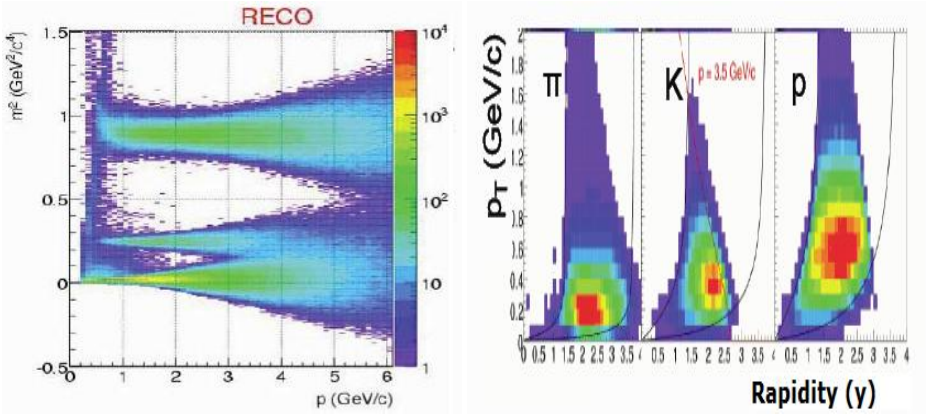

(a) (b)

Figure 5.9: (a) Reconstructed squared mass of primary hadrons in the TOF acceptance as function of momentum. (b) Distribution of TOF-identified primary hadrons in rapidity and transverse momentum in central Au+Au collisions at 25 AGeV. Mid-rapidity is 1.98.

recently proposed as sensitive probe for the dense medium [170] is of particular challenge due to its short life time (60 μm) and surely requires the applications of latest technologies [62, 171].

5.6.3 Hadrons at TOF

Fluctuation and correlation measurements require that CBM detector should be able to identify hadrons with good precision. The identification of pions, kaons and protons emerging from close to the interaction point will be accomplished by a time-of-flight (TOF) system located about 10 m downstream of the target. The CBM detector accepts charged particles emitted at polar angles between 2.5 and 25 degrees in the laboratory. The resulting phase-space coverage for reconstructed pions, kaons and protons produced in Au+Au collisions at 25 AGeV is illustrated in Fig. 5.9 as function of transverse momentum and rapidity. Clearly, Kaons can be separated from pions for momenta up to 4 GeV, while protons can be identified up to 8 GeV. The acceptance for identified hadrons, shown in figure 5.9b, covers the bulk of the production for all three particle species. The measurement of event-by-event particle ratio fluctuations requires kaon identication with high purity. Simulation results shows that pions and kaons are separated by 2σ of the mass resolution up to laboratory momenta of 3.2 GeV/c. The requirement of a kaon purity of 99% restricts the efficiency to laboratory momenta below to about 3.5 GeV. Depending upon the required koan purity we can introduce the momentum cut accordingly to the selected sample of kaons.

Hadron identication is performed in several steps. First, track reconstruc-

tion and momentum determination in the Silicon Tracking System is performed (no MVD required). These tracks are extrapolated to the Transition Radiation Detector (TRD) stations where the TRD hits are included in the track reconstruction, and finally these reconstructed tracks are matched to the nearest hit in the RPC-TOF detector [62, 171].

5.6.4 Electrons at RICH and TRD

In the CBM experiment the electrons and positrons are identified by combination of RICH(ring imagining cherenkov) detector and TRD(transition radiation detector). Electrons are identified via their Cherenkov radiation at RICH de-

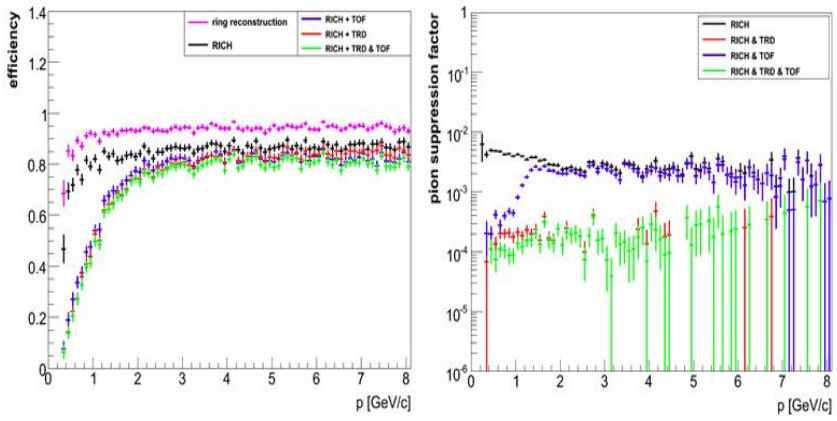

(a) (b)

Figure 5.10: (a) Electron efficiency and (b) pion suppression obtained with combined RICH, TRD and TOF information in central Au+Au collisions at 25 AGeV

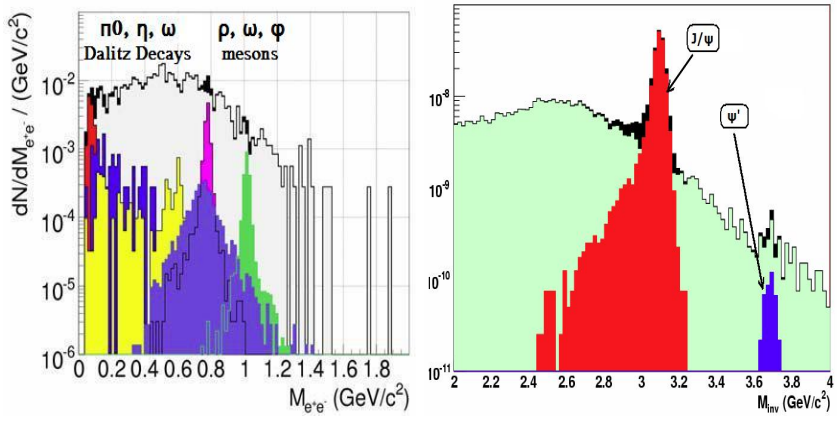

(a) (b)

Figure 5.11: Invariant-mass spectra for pairs of identified electrons in the (a) low-mass vector meson region and (b) in the charmonium mass region (J/ψ, ψ'). No transverse momentum cut was applied on the electrons from low-mass vector mesons.

tector and via their transition radiation at TRD. Cherenkov photons produced in the radiator are focussed into rings on two vertically separated planes, which are shielded from direct tracks by the magnet yokes. Simulation shows that electrons can be separated from pions up to a momentum of 12 GeV at RICH detector [Fig. 5.10b]. The main source of background in the electron sample at low momenta is a mismatch of soft pion tracks from the primary vertex, and *rings* from secondary electrons. Most of the *electron rings* measured in the RICH are not produced by electrons emitted from the primary vertex, but rather stem from secondary electrons which are produced by gamma conversion in the detector material or in the magnet yoke. As their tracks cannot be reconstructed, there is a certain probability of matching these background electron rings to pion, kaon or proton tracks from the primary vertex.

The combined performance of RICH and TRD is shown in Fig. 5.10. A pion suppression of about 10^4 is reached at electron efficiencies of about 70-80% for momenta above 1 GeV. At lower momenta, the additional use of TOF information still improves on the rejection of pions.

Having rejected the vast majority of hadrons, the low-mass di-electron measurements still suffer from physical background originating from Dalitz decays of π^0 and η as well as from photon conversion in the target. Target thickness was limited to 25 μm to suppress γ-conversion. Figure 5.11 shows the simulated CBM performance with dielectrons for low-mass vector mesons and charmonium in central Au+Au events at 25 AGeV beam energy, using fully reconstructed and identified electrons. The measurement of both light and heavy vector mesons appears feasible [171].

5.6.5 Muons at MuCh

Muon Chamber (MuCh) in CBM is designed to measure muon pairs from the decay of vector mesons (ρ, ω, ϕ, J/ψ) produced in heavy-ion collisions. At *FAIR* energies the muon momenta can be low, so, muon detection concept with a dynamical absorber thickness is considered. The definition of a muon depends on its momentum which varies with the mass of the vector mesons and with beam energy. For example, muons from the decay of J/ψ mesons have to pass all 6 absorber layers with a total iron thickness of *225 cm* corresponding to $13.4\lambda_I$ (interaction length). The muons from the decay of low-mass vector mesons (ρ, ω, ϕ) only have to penetrate through 5 iron absorber layers with a total thickness of *125 cm* ($= 7.5\ \lambda_I$) [62].

Fig 5.12 displays the invariant mass spectra of muon pairs in the region of low-mass vector mesons [Fig.5.12a] and for charmonium [Fig.5.12b] simulated for central Au+Au collisions at a beam energy of 25 AGeV. As in the electron

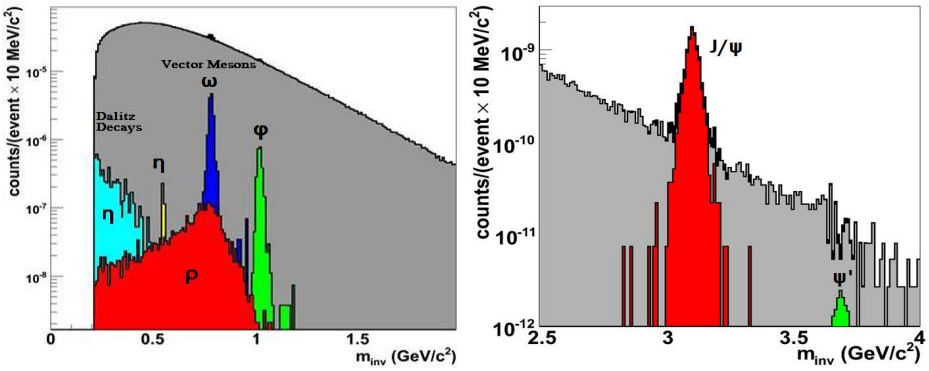

(a) (b)

Figure 5.12: Invariant-mass spectra for pairs of identified muons in the (a) low-mass vector meson region and (b) in the charmonium mass region .

case, the peaks of ω, ϕ and J/ψ are clearly visible above the combinatorial background made up of muons from *pion* and *kaon* decay before the absorber, *punch-through hadrons*, and track mis-matches between STS and muon system. In the analysis of low-mass vector mesons not only pairs of "*hard*" muons, which pass *1.25 m* of iron and have laboratory momenta of more than $p_{lab} = 1.5$ GeV/c, are included but also pairs of "`soft`" muons, which only passes *0.9 m* of iron and have laboratory momenta around $1.2 < p_{lab} < 1.5$ GeV/c. In this way the reconstruction efficiency for low-mass vector mesons is increased, with only little effect on the signal-to-background ratio. For the analysis of charmonium only pairs of "`hard`" muons (penetrating *2.25 m* of iron) are considered, no cut on transverse momentum is applied. A minimal transverse momentum of $p_T > 1$ GeV/c is required for single muons. The signal-to-background ratio is of the order of 10 for J/ψ mesons, and about 0.1 for ψ' mesons.

Simulation also shows that acceptance for ρ-mesons is slightly shifted to *forward rapidities* (midrapidity is at *y=2* for 25 AGeV) due to the absorption of muons of laboratory momenta below 1.2 GeV/c. In contrast, the acceptance for charmonium does not suffer from the momentum cutoff which is at $p_{lab} = 2.8$ GeV/c for an iron absorber of 2.25 m thickness. The performance of the CBM muon detection system for low-mass vector mesons can be considerably improved when installing a time-of-flight detector between the second last and the last absorber of 1 m thickness [62, 171].

5.6.6 Direct photons at ECAL

Transverse momentum spectra of single photons are suggested to provide information on the (highest) temperature of the early created dense medium (QGP).

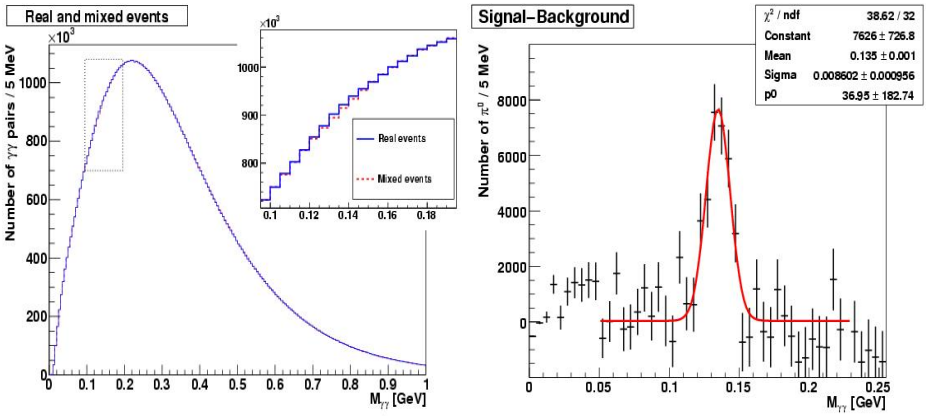

(a) (b)

Figure 5.13: Invariant mass spectra for momentum integrated $\pi 0$ mesons for 5000 central Au+Au collisions at 25 AGeV: (a)Full spectrum with combinatorial background (b) Background subtracted spectrum.

One way of direct photon measurements is using the *electromagnetic calorimeter(ECAL)*, and other possibility is to reconstruct, in particular the low momentum, photons by γ-conversion in the target and measuring the resulting electrons.

The ECAL provides photon identification via an energy loss measurement from electron-photon showers in the sampling scintillator-lead structures of the ECAL modules. With one setup approximately 80 photons are detected per central Au+Au collision at 25 AGeV beam energy out of which 90% are from π^0 decays but also 3% from η-decay. Invariant mass spectra for the extraction of π^0 mesons from the combination of two photons are shown in Fig. 5.13a. The huge combinatorial background is still a lower estimate as not all background sources are included yet. With a signal-to-background ratio on the order of 0.01 the background can be well estimated by even-mixing methods and subtracted. The reconstruction probabilities depending on energy cutoffs are on the order of (1-2)%. Similar conditions concerning signal-to-background ratios and efficiencies are expected for the reconstruction of the η-meson.

A detection of low momentum photons(< 5 GeV) by the conversion into an $e^{\pm}$ pair might be favorable as the momentum resolution from tracking is at a 1% level down to momenta of 0.5 GeV/c. Electrons are identified for the di-electron measurements, only pairs from conversion in the target are selected for this analysis. For the combined pairs the momentum resolution is about 2 %. A cut on the opening angle of the di-lepton pair is done ($\theta < 1^0$) in order to enhance di-electrons from conversion above those from π^0-Dalitz decay. The resulting transverse momentum spectrum of the photons is shown in Fig. 5.14. Dominant

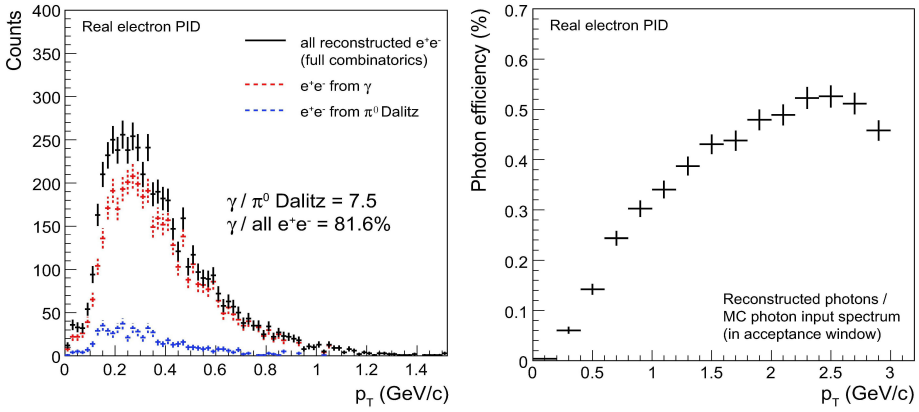

(a) (b)

Figure 5.14: (a)Transverse momentum spectrum of reconstructed photons from the target identified by their conversion into di-electrons at central Au+Au collisions at 25 AGeV for 20000 events. An opening angle cut of $\theta < 1^o$ is applied. The contributions of the two main sources are γ-conversion (red)and π^0-Dalitz decay (blue)), shown separately. (b)Combined reconstruction and identification efficiency of photons in the acceptance window of CBM ($2.5^o < \theta < 25^o$ for embedded π^0).

contributions clearly come from photons and π^0 decays, mis-identifications play a minor role. The overall identification probability of photons via conversion in the target is on the order of 0.5 % [Fig. 5.14] [62].

Chapter 6

Analysis and Results

Preliminary analysis has been carried for the optimisation of the first absorber thickness of the MuCh(muon chamber) for CBM experiment. Purpose is to allow the absorber to suppress background particles including muons decaying from pions and kaons so that MuCh can efficiently reconstruct the charmonium and LMV mesons via di-muon decay channel. Multiplicity of the particles have been studied at different absorber thickness. Backscattering effects of the absorber have been primarily analysed. Magnetic effects on the particle multiplicity as well as other sources have been included in the analysis. Various observations and analysis results are discussed in this chapter.

6.1 Analysis tools used

Tools that have been used for analysis include:

1. Linux based *CBM Frame work* for simulation

   (a) **FairSoft:** July'09 version [174] (external packages)

   (b) **ROOT:** DEC'09 version of cbmRoot [117]

2. Different *event generators* for embedded data set of signal and background

   (a) **PLUTO:** PLUTO generated 1000 events for `signal particles` (charmonium and low mass vector mesons) i.e $J/\psi, \rho, \omega$ and ϕ decaying into di-muons with multiplicities taken from the HSD at 25 GeV. The J/ψ signal decay assumes a thermal source with a temperature of 130 MeV. According to HSD calculations, the J/ψ multiplicity in central Au+Au collisions at 25 AGeV is about 1.9×10^{-5}.

(b) **UrQMD:** UrQMD generated 1000 events at central Au-Au collision at 25 GeV for *background particles*. Background for muons consists mainly of weak decays of charged pions and kaons. For muon transverse momenta above 1 GeV/c, pions and kaons contribute almost equally to the background. The simulations shows that a cut on the single muon transverse momentum of p_T >1 GeV/c suppresses about 99% of the background but only about 20% of the signal.

3. **GEANT3 transport Code** to transport these events through the detector.

4. Different geometries for STS and MuCh

   (a) **Standard STS Geometry:** Standard STS station has 8 detector stations positioned at 30, 35, 40, 50, 60, 75, 90, 100 from the target made of 250 μm thick gold plate. The first 3 stations are placed in vacuum in order to decrease effect of multiple scattering in the carbon beam tube on track parameters at the target.

   (b) **Reduced MuCh Geometry:** Reduced MuCh geometry has 3 iron absorbers of total thickness 225 cm with 30, 70 and 125 cm respective thickness. 9 detector station layers have been used with 3 station layers sandwiched between the absorbers. Each station layer is separated at 10cm from each other and 5 cm from the absorber as shown in figure 6.1a. Fig. 6.1b shows different parameters that have been set for this geometry that was used in the analysis.

6.2 Simulation processes

Simulation has been performed to analyse the effect of the first absorber thickness on the particle multiplicity when it is changed from 30cm to 0cm in different steps. The steps followed were:

1. Signal events(1K) from PLUTO event generator were embedded with the background events(1K) from the UrQMD event generator.

2. These embedded events where transported through the MuCh by GEANT3 transport code which uses the Monte Carlo method.

3. Hits/points, by these signal and background particles, were recorded at the STS and MuCh detector stations.

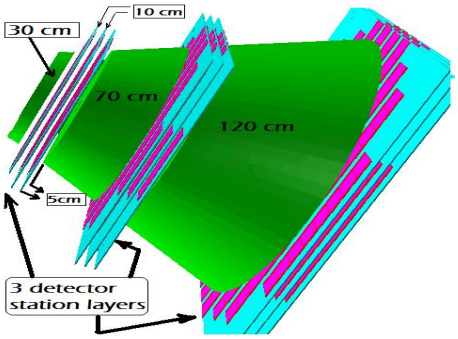

(a)

```
# General information
MuchCave Zin position [cm] :   105
Acceptance tangent min     :   0.1
Acceptance tangent max     :   0.5
Number of absorbers            3
Number of stations         :   3

# Absorber specification
Absorber Zin position [cm] :   0     65     170
Absorber thickness [cm]    :   30    70     125
Absorber material          :   I     I      I

# Station specification
Station Zceneter [cm]      :   47.5  152.5  312.5
Number of layers           :   3     3      3
Detector type              :   1     1      1
Distance between layers [cm]:  10    10     10
Support thickness [cm]     :   1.5   1.5    1.5
Use module design (0/1)    :   1     1      1

# GEM module specification (type 1)
Active volume lx [cm]      :   32.0
Active volume ly [cm]      :   32.0
Active volume lz [cm]      :   0.3
Spacer lx [cm]             :   0.5
Spacer ly [cm]             :   5
Overlap along y axis [cm]  :   2
```

(b)

Figure 6.1: (a) Reduced Geometry layout of the MuCh(3 stations = 9 station layers) (b) Different Geometrical parameters set for the detector for analysis (here I = Iron).

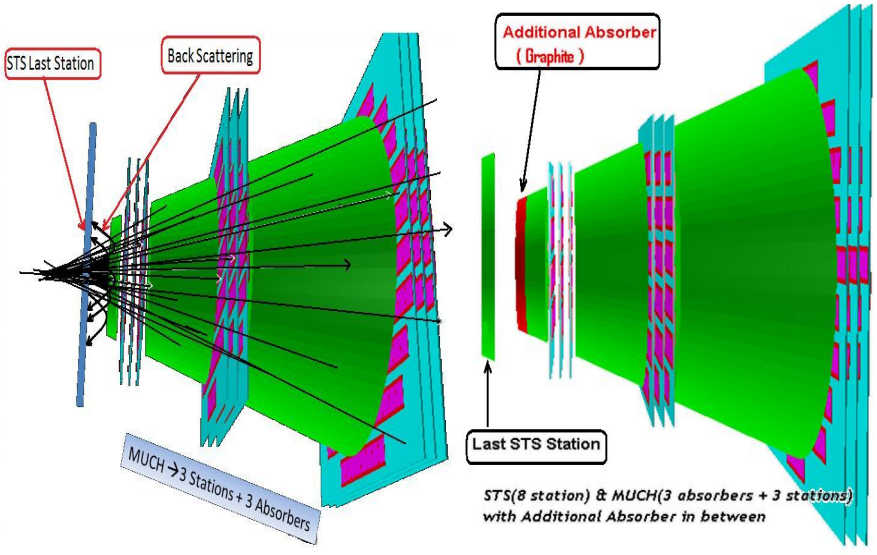

(a) (b)

Figure 6.2: (a) Muon Chamber when analysed for backscattering that affects the last STS station (b) Introducing the additional absorber of Graphite (shown as red) in between the last STS station and the first MuCh absorber.

4. A C++ code in cbmRoot environment, i.e. **macro**, was written to get the hits/points at the last station of the STS. Later points at the first detector station layer of the Much were also extracted. *This needs lot of understanding of the framework, procedure and programming.*

5. Then hits/points for different particles where extracted at the last STS station and first MuCh detector station.

6. Steps 4 and 5 were repeated for different absorber thickness of the first absorber of the MuCh while keeping other parameters fixed. Absorber thickness for first absorber was changed from 30 cm to 20 cm, 10 cm, 7 cm, 4 cm, 2 cm, 0 cm for reasons that will be discussed in the results.

7. For one case MuCh modules was removed and only hits/points at the STS last station were recorded. And for the same case then Magnetic field was doubled, halved, moved backwards and then forward in steps and STS points where recorded.

8. Additional absorber of Graphite (carbon) was introduced (via code in the framework) in between the first absorber as depicted in Fig. 6.2b and the last STS station to record the effect on the hits/points on the two stations under consideration.

9. A code was written to get the time spectra of different particles arriving at the last STS station and the first MuCh station at different absorber thickness.

10. Finally particle wise energy spectrum was extracted, by writing a code for it, at different absorber thicknesses.

Purpose is to look at the particles, at STS, that are getting back-scattered by the first absorber of MuCh while changing its thickness depicted in Fig. 6.2a. There are some particles like Neutrons that can damage the silicon stations in high multiplicity environment which the realistic case.

6.3 Results and discussions

Particle wise multiplicities recorded at last STS station(i.e. 8th station), positioned at 100cm from the target, for different absorber thickness of the first MuCh absorber are shown in the Table 6.1. Last column contains the result when MuCh module was removed from the CBM experiment set-up, called as NO-MUCH condition.

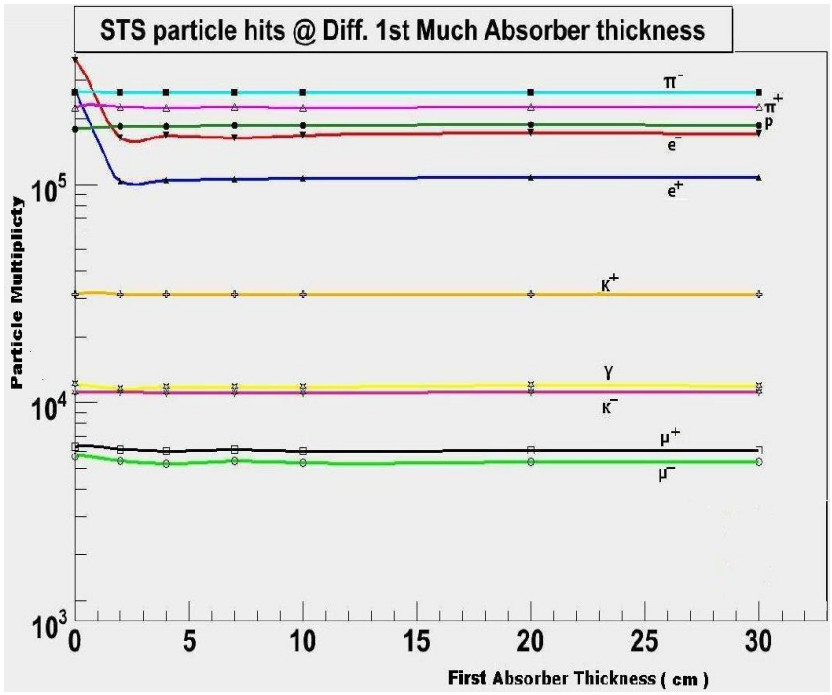

(a)

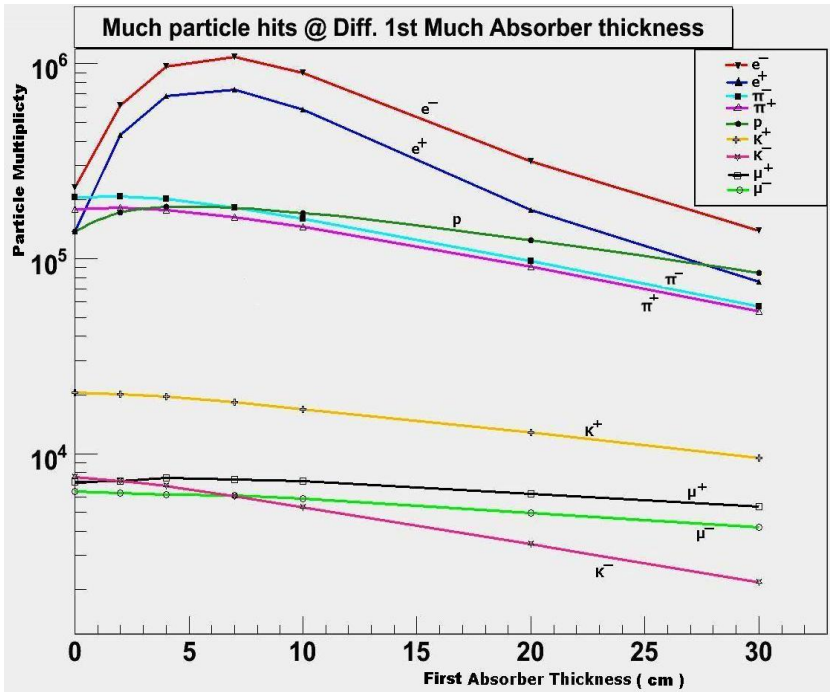

(b)

Figure 6.3: Particle multiplicity for different first absorber thickness of MuCh at (a) last STS Station. (b) first MuCh Station layer.

Table 6.1: Hits/points at last STS detector station for different thickness (in cm) of first absorber of MuCh

Particles	STS points at different first absorber thickness of MuCh							
	30 cm	**20 cm**	**10 cm**	**7 cm**	**4 cm**	**2 cm**	**0 cm**	**NoMuch**
γ	11901	12048	11801	11766	11720	11566	12103	10842
e^+	*107569*	*107286*	*107001*	*105689*	*105021*	*103520*	*270441*	*295671*
e^-	*171236*	*172567*	*168303*	*162172*	*167729*	*163434*	*368441*	*399535*
μ^+	6028	6018	5997	6074	5984	6095	6281	6017
μ^-	5354	5336	5282	5367	5237	5392	5673	5450
π^+	225842	225650	225416	225564	225251	225603	225257	223883
π^-	263367	263542	263550	263536	263100	263602	263021	262215
K^+	31316	31311	31374	31288	31323	31379	31352	31348
K^-	11123	11092	10993	11039	11042	11086	11038	11129
n	*34*	*36*	*44*	*31*	*35*	*43*	*27*	*38*
p	186471	186727	186312	185711	184848	184649	179705	171838
$\bar{p}$	237	228	242	238	247	245	229	230
Σ^+	77	74	76	74	70	58	73	83
Σ^-	363	412	390	380	394	360	383	404
Ξ^-	14	15	13	10	23	18	16	17
$\overline{\Sigma}$	2	5	1	1	0	1	3	1
$\overline{\Xi}^-$	1	0	1	0	0	0	1	2

Also, particle wise multiplicities were recorded at first MuCh station at different absorber thicknesses of the first MuCh absorber. The results are shown in Table 6.2.

6.3.1 Effects on electron - positron pairs

From the Table 6.1, it is evident that many particles show backscattering effects due to the change in the first absorber of the MuCh when its thickness was changed. On reducing the first absorber thickness of the MuCh there is there is slight increase in the e^-e^+ pairs till 0cm on STS. When thickness of the absorber is reduced to the 0cm there is abrupt increase in e^-e^+ count. Surprisingly, when MuCh module was removed from the CBM experimental set-up (shown as NO-MUCH condition in the table) there was even further increase in e^-e^+ pairs. Which clearly means that these are not the backscattered particles, and their source is something else as they are coming from apposite side towards the target. *Their probable source can be '**beam pipe**' or they may be **delta electron**-positron pairs.* These possibilities will also be explored in the analysis. Figure 6.3a shows plot of different particle multiplicities at STS last detection layer at different first absorber thickness of MuCh.

From the Table 6.2, it is clear that on reducing the Absorber thickness from 30 cm to 7 cm there is increasing trend in the e^-e^+ pairs at first MuCh station.

Table 6.2: Hits/points at first MuCh detector layer for different thickness (in cm) of first absorber of MuCh

Particles	MuCh points at different first absorber thickness						
	30 cm	**20 cm**	**10 cm**	**7 cm**	**4 cm**	**2 cm**	**0 cm**
γ	56	139	226	248	158	143	131
e^+	*76386*	*177463*	*583333*	*735927*	*682306*	*431998*	*137972*
e^-	*138673*	*315245*	*898519*	*1079524*	*965641*	*612319*	*231744*
μ^+	5371	6224	7257	7342	7531	7258	7193
μ^-	4177	4951	5892	6096	6169	6247	6370
π^+	53581	90836	146052	163523	178287	182254	179039
π^-	56586	97647	160269	182393	202459	209294	207394
K^+	9471	12841	16918	18311	19559	20240	20614
K^-	2184	3422	5282	6019	6819	7210	7606
n	0	0	1	0	0	0	0
p	84170	124641	171556	182000	183817	172703	137183
$\bar{p}$	19	37	69	82	117	130	156
Σ^+	23	39	33	30	30	24	3
Σ^-	39	54	61	68	53	51	32
Ξ^-	0	2	1	0	1	5	10
$\overline{\Sigma}$	0	0	0	0	0	0	0
$\overline{\Xi}^-$	0	0	0	0	0	0	0

From 6cm onwards up to 0cm of the absorber thickness there is decreasing trend. At 0 cm there is sudden decrease in the number. Which means that probably electromagnetic shower inside the iron absorber starts leaking, from 20cm thickness onwards, increasingly and thus contributes to e^-e^+ number. When the critical absorber thickness is reached, which is in between 7-4 cm, EM showers inside the absorber doesn't get full length to develop fully and as a result e^-e^+ contribution starts falling. Figure 6.3b shows plot between different particle multiplicities and first absorber thickness of MuCh.

6.3.2 Additional Graphite Absorber and Neutrons

From the Table 6.1, it is also observed that neutrons show slight backscattering effect, on the STS, by the first absorber when its thickness is changed. Neutrons are always unwanted stuff for the detector especially when it is made of silicon strips. They can damage the detector with time as there number will be sufficiently large in the realistic case of very high multiplicity environment.

To reduce the backscattered neutrons hitting last STS station, an additional absorber of '**graphite**' (highly dense carbon) was introduced between the last STS detector station and the first absorber of MuCh as shown in Fig. 6.2b.

Then thickness of the additional graphite absorber was changed to 0, 10 and 20 cm while keeping the first absorber thickness to a fixed value of 20 cm. Then

Table 6.3: Hits/points at STS and MuCh detector layer for different thickness (in cm) of additional absorber of 'graphite', introduced between STS and MuCh, and first absorber thickness of MuCh is kept fixed to 20 cm value.

	points at different absorber thickness of graphite (G) and first absorber thickness of MuCh = 20 cm (fixed)					
	STS Points at G=:			MuCh Points at G=:		
Particles	**0 cm**	**10 cm**	**20 cm**	**0 cm**	**10 cm**	**20 cm**
γ	12048	11935	11651	139	105	85
e^+	*107286*	*107264*	*110684*	*177463*	*148885*	*137935*
e^-	*172567*	*175855*	*181410*	*315245*	*268604*	252582
μ^+	6018	6196	6097	6224	6061	5649
μ^-	5336	5256	5383	4951	4708	4574
π^+	225650	226202	226734	90836	74852	62371
π^-	263542	264780	265066	97647	79300	65325
K^+	31311	31361	31464	12841	11633	10188
K^-	11092	11040	11102	3422	2755	2300
n	*36*	*31*	*26*	0	0	0
p	186727	178294	176666	124641	109648	94164
$\bar{p}$	228	242	244	37	17	16
Σ^+	74	79	63	39	29	28
Σ^-	412	356	358	54	35	53
$\bar{\Xi}^-$	15	15	13	2	0	0
$\overline{\Sigma}$	5	2	3	0	0	0
$\overline{\Xi}^-$	0	0	0	0	0	0

hits at last STS station and first MuCh absorber were recorded. There was negligible effect on the electron-positron but neutrons were reduced slightly as shown in Table 6.3. FLUKA transport code is considered better for neutron analysis than GEANT.

6.3.3 Magnetic field effects

Since our previous results in table. 6.1 showed unknown source electron-positrons from the backward direction. One of the assumption was considered that they may be '**delta electrons**(positrons)' recoiling in the magnetic field.

Magnetic field was halved, doubled, moved forward and moved backward while removing the MuCh module from the set-up and then particle multiplicities at STS last station were recorded.

Normal position for the magnetic field is 50 cm from the target, it was moved to 70 cm (forward) and 30 cm (backward) in the simulation. Results are presented in the Table 6.4. Results clearly show the effect of magnetic field on the particles under consideration. Which makes it evident that in presence of strong magnetic field electron-positron pairs in empty space of removed MuCh (i.e. NO MUCH case as shown in depicted in figure 6.4) recoil greatly to record

Table 6.4: Hits/points recorded at STS at 0 cm first absorber thickness of MuCh and when MuCh module is removed from the set-up then magnetic field is changed.

	`STS points at 0 cm absorber thickness` and when $\vec{B}$ (magnetic field) is changed					
	1^{st} absorber	**NO MUCH** and when				
		`Magnet` positioned from target at: (cm)			scale of $\vec{B}$ is:	
Particles	**0 cm**	**50**(normal)	**70**(forward)	**30**(backward)	**2**(double)	**0.5**(half)
γ	12103	10842	11152	10737	10723	10969
e^+	*270441*	*295671*	*312653*	*265764*	*313012*	*251822*
e^-	*368441*	*399535*	*409831*	*370004*	*384857*	*363013*
μ^+	6281	6017	7069	5752	6740	6253
μ^-	5673	5450	6539	5240	5548	5828
π^+	225257	223883	227206	223861	199298	234794
π^-	263031	262215	265894	262408	230530	275492
K^+	31352	31348	31444	31306	30106	31729
K^-	11038	11129	11115	11034	10600	11181
n	*27*	*38*	*32*	*41*	*28*	*31*
p	179705	171838	171798	171621	166262	173694
$\bar{p}$	229	230	239	229	227	237
Σ^+	73	82	60	86	70	72
Σ^-	383	404	385	377	391	392
Ξ^-	16	17	16	15	16	13
$\overline{\Sigma}$	3	1	1	0	2	1
$\overline{\Xi}^-$	1	2	0	0	0	1

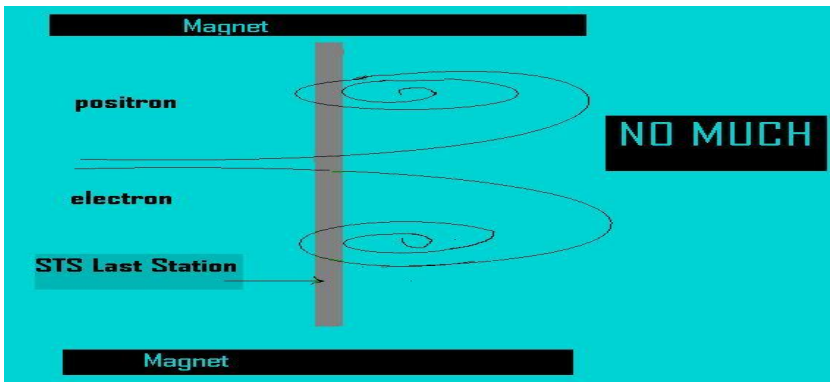

Figure 6.4: Recoiling electron-positron pairs in magnetic field hitting the STS station multiple time in presence of Magnetic Field and in absence of MuCh module

the hits multiple time. *Thus delta electron contribution is one of the reason for the increase in electron-positron hits on the STS in absence of MuCh module.*

To confirm this, simulation was carried in which case Magnetic field was switched OFF and the results will be discussed in last section.

6.3.4 Time distribution of particles

Figure 6.5 shows the time distribution of particles hitting the STS last detector station at different first absorber thickness, like 30 cm, 20 cm, 10 cm and 0 cm, of MuCh. Results can be compared with the NO-MUCH case (i.e. when MuCh is removed). It is clear that on reducing the thickness to zero or even removing the MuCh module from the set-up, the particles that take less time to hit the STS are increased in number. Which means that either the source of these increased particles is very near or they are very high energetic particles. In later case, then question is where these particles go even when there is slight increase in the absorber thickness. So, it is obvious that first assumption is most suitable. *Nearest source of these particles (most probably they are electron-positrons) can be* ***beam-pipe*** *or* ***beam pipe shielding****.* To confirm this, simulation has been done in which `beam-pipe` and `beam pipe shielding` was removed from the module and the results will be discussed in last section.

6.3.5 Particle-wise energy spectrum

Particle wise energy spectrum at STS and MuCh for different first absorber thicknesses and other conditions of MuCh are shown in figures 6.6, 6.7, 6.8 and 6.9. From Fig. 6.6a and 6.6c, electrons and positrons at STS in case of NO-MUCH shows little deviation at lower energy side. *Which means that the increased number in electron-positron pairs corresponds mainly to lower energy*

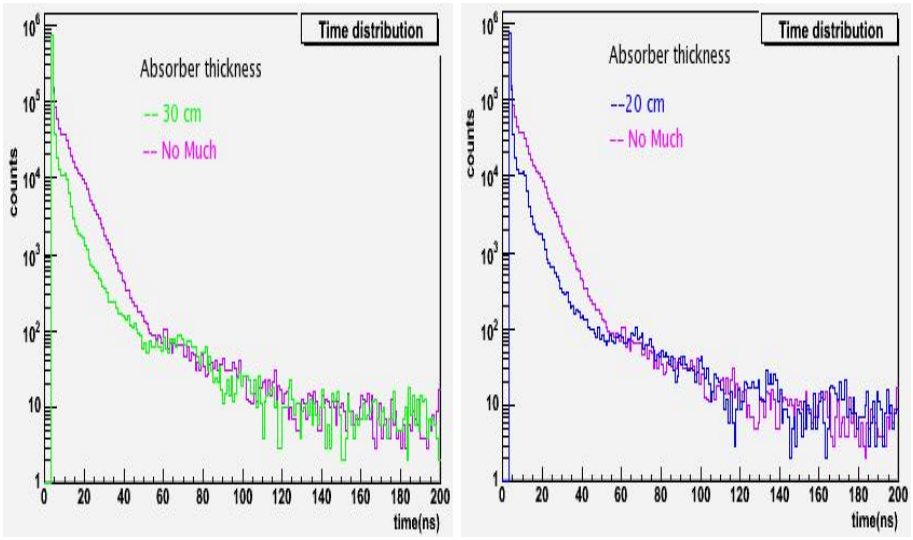

(a) (b)

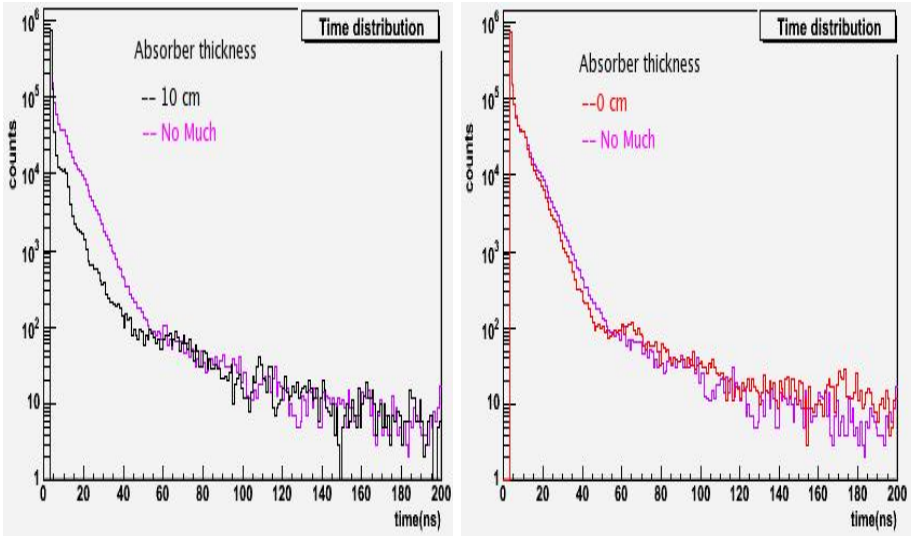

(c) (d)

Figure 6.5: Time distribution of particles at STS at different first absorber thickness of MuCh.

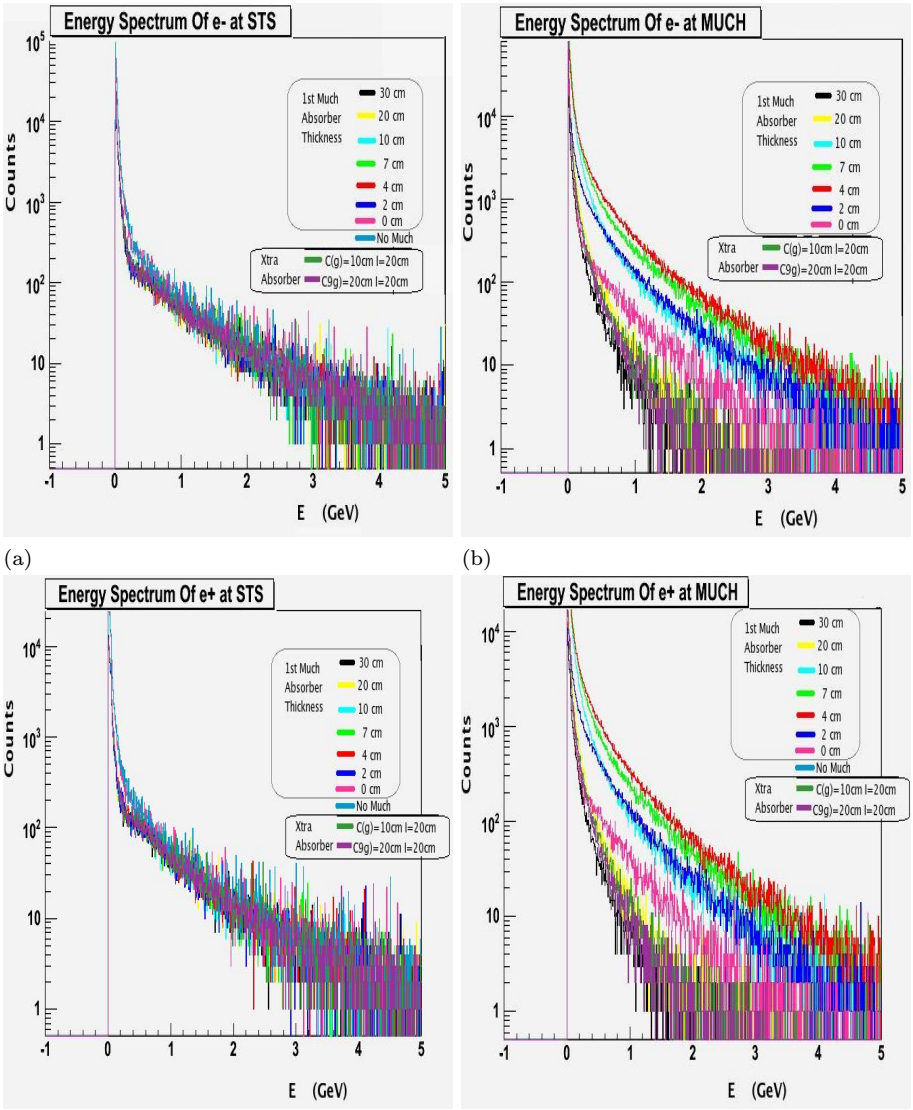

Figure 6.6: Energy spectrum, at different first absorber thickness of MuCh, of particles like: (a) `electrons` at STS (b) `electrons` at MuCh (c) `positrons` at STS (d) `positrons` at MuCh

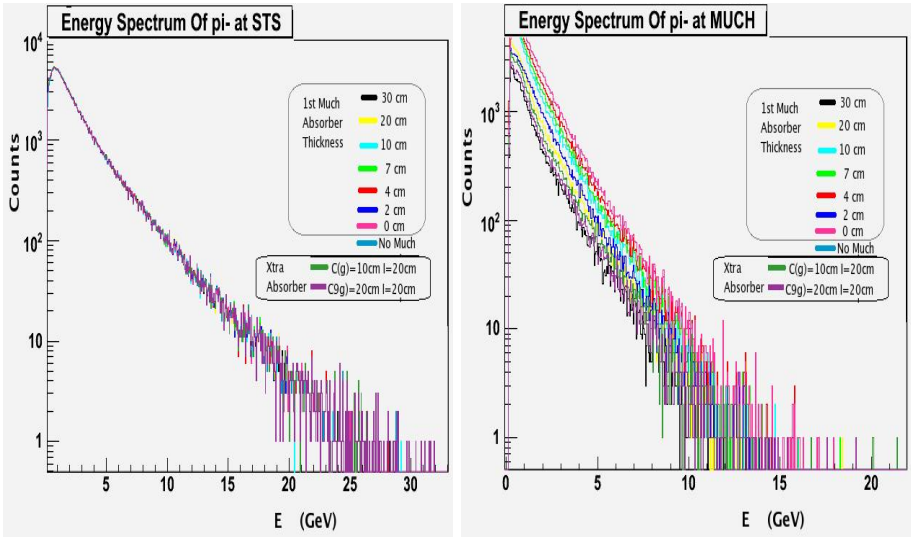

(a) (b)

(c) (d)

Figure 6.7: Energy spectrum, at different first absorber thickness of MuCh, of particles like: (a) π^- at STS (b) π^- at MuCh (c) π^+ at STS (d) π^+ at MuCh

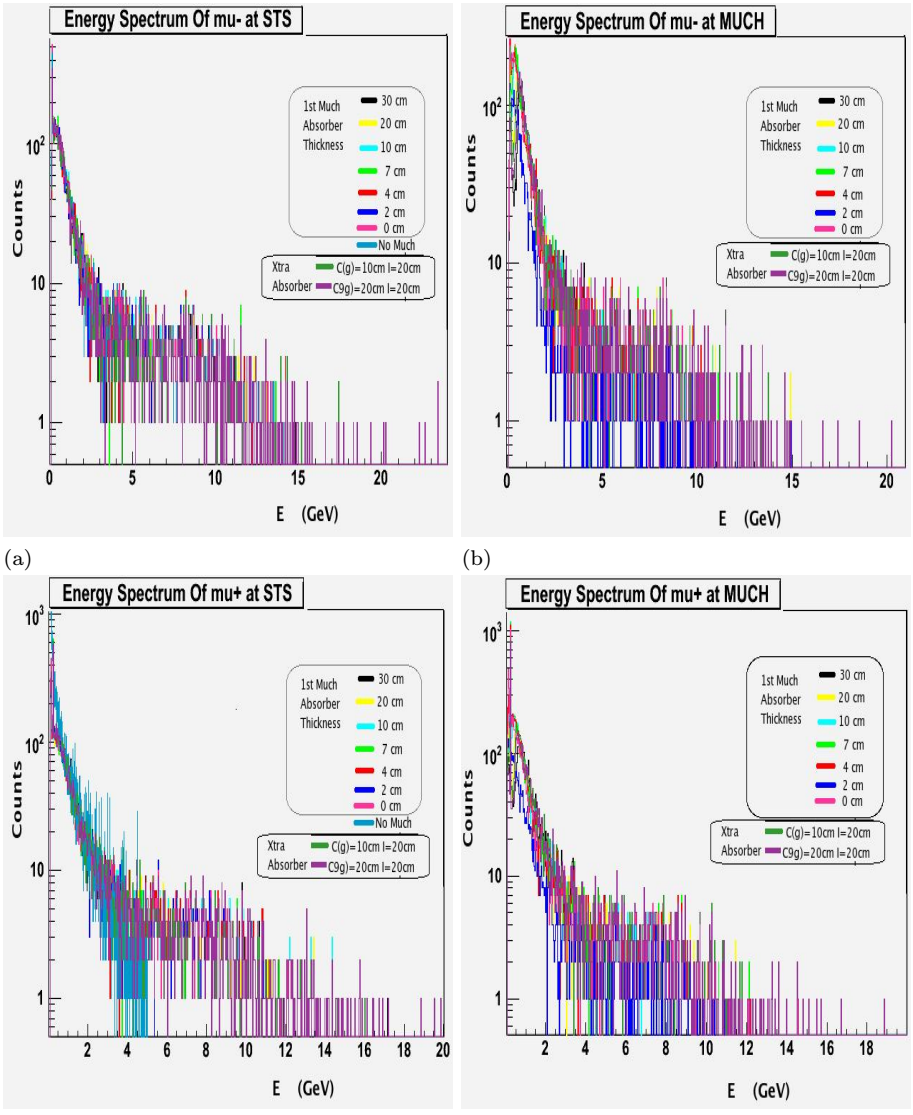

(a) (b)

(c) (d)

Figure 6.8: Energy spectrum, at different first absorber thickness of MuCh, of particles like: (a) μ^- at STS (b) μ^- at MuCh (c) μ^+ at STS (d) μ^+ at MuCh

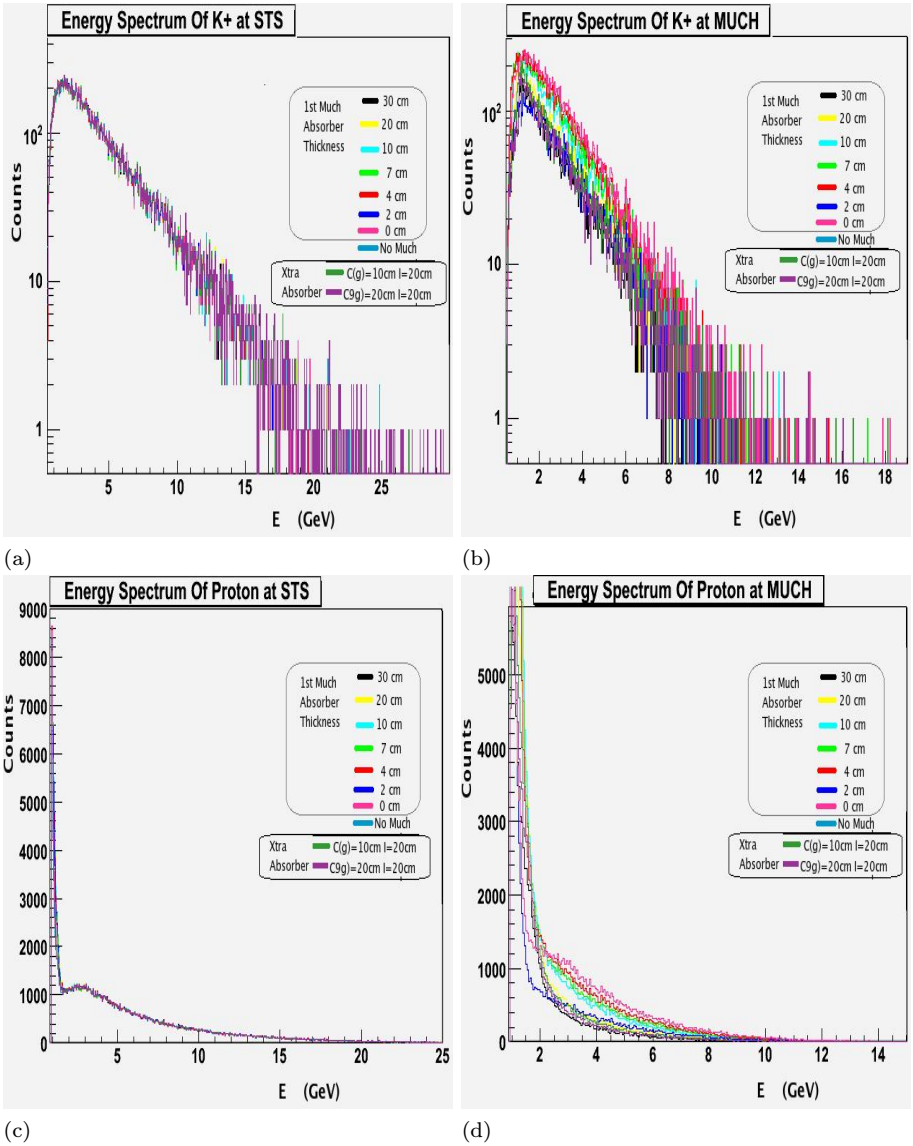

Figure 6.9: Energy spectrum, at different first absorber thickness of MuCh, of particles like: (a) K^+ at STS (b) K^+ at MuCh (c) `protons` at STS (d) `protons` at MuCh

when first absorber thickness is reduced to zero or even when MuCh is removed. Which also *means that their probability of being from high energetic collision point is low.* The possible *source can be beam pipe or its shielding.* Also, from Fig. 6.6b and 6.6d it is evident that on reducing first absorber thickness up to 4cm, there is almost proportional increase in every energy range of electron-positron pairs. But from 4cm onwards electron-positron pair count start decreasing and decrease is slightly more in lower energy side.Which may be due to electromagnetic-shower that doesn't develop fully from 4cm onwards to contribute the counts coming out from absorber without getting absorbed fully. Also on introducing the graphite absorber there is slight decrease in the the counts of particles of every energy range.

Pions ($\pi^{\pm}$), muons ($\mu^{\pm}$), Kaons and protons shows negligible backscattering effect due to changed absorber thickness when seen from the last STS detector station (Fig. 6.7a, 6.7c, 6.8a, 6.8c, 6.9a, 6.9c). While these particles show proportional decrease in the absorption due to reduction of the first absorber thickness of MuCh as seen from the first detector layer of the muon detection system (Fig. 6.7b, 6.7d, 6.8b, 6.8d, 6.9b, 6.9d).

6.4 Conclusion

Different particle multiplicities have been analysed at silicon tracking station and muon chamber by changing the thickness of the first absorber of the muon detection system. Analysing particles at STS was done to look for the backscattering effects due to the absorber and look for the optimised thickness where the effect is negligible. Analysis of particle multiplicities at the first muon detection station was done to look for the absorption effects of the absorber on different particles and look for the optimised thickness where most of the background particles, i.e. particles other than primary muons etc, are suppressed (absorbed).

Analysis were carried by using simulation in CBM frame-work. Background particle events were created by using UrQMD event generator and signal particles(muons from J/ψ) were created by using PLUTO event generator and their multiplicities were taken from HSD. These particles were transported in CBM set-up using GEANT3. A code (Root macro) was developed for analysing the simulated Monte-Carlo points on MuCh and STS for different particles by using the PDG-Code information [175].

Analysis showed that there was an unexpected increase in the yield of electron-positron pairs on silicon tracking station when thickness was reduced to zero of first absorber of muon chamber. Is this the backscattered particles from MuCh? or is their any other source of these particles?, was the immediate analysis task

taken. To carry this job, MuCh module was removed from the CBM set-up in simulation and results (Table 6.1) showed further increase in these particles. This result removed the assumption that these particles are backscattered from MuCh rather they have any other source. In next analysis task, magnetic field was changed and results (Table 6.4) showed considerable increase in these particles with increase in magnetic field strength. Which showed that some of the increased hits coming from opposite side are due to the recoiling `delta electrons` (positrons). Then further analysis was carried in which time spectra of all the particles were plotted (Fig. 6.5). These results showed that these increased particles have source nearest than collision point as there is increase in the number of particles taking less time when MuCh was removed. Next analysis was carried in which energy spectrum of the particles was obtained. This also pointed a some source other than collision point for these increased electron positron pairs. Nearest source of these large number of electron-positrons pairs coming in opposite direction can be either `beam pipe` or `wolfram(tungsten) shielding`. In next analysis, to be under taken in Ph.D. programme, beam pipe and beam pipe shielding will be explored as a probable source for this high yield of electron-positron pairs. If they proved to be the source, then other materials to be used for the shielding/beam pipe will be explored. Accordingly suggestions will be incorporated in the R & D work for constructing the MuCh.

As far as backscattered neutrons are concerned, analysis showed some numbers on the STS in presence of the MuCh chamber, beam pipe and shielding. In high multiplicity environment their increased number is the point of concern for the STS detector, as they can destroy the silicon tracking stations. Analysis was done in which additional absorber of graphite was introduced in between the two detectors (STS and MuCh). Slight decrease was seen (Table 6.3) in the neutron number but it has to be reduced to the lowest number. In Ph.D. programme *beam pipe and shielding will also be explored for this purpose.* Also GEANT is not considered best for neutron analysis, so *FLUKA transport code option will also be used.*

As far as absorption (reflected by hits on MuCh detector station) of the particles is concerned our analysis along with research already done [116] in this regard shows a first iron absorber of 20 - 30 cm thickness as the best compromise between hit density and background[116] suppression.

But as far as backscattering effects (reflected by hits on STS detector station) are concerned analysis so far paved the way towards the optimisation that will be finished in Ph.D. work. Then finally compromise will be made between the two contrasting effects (back-scattering and absorption) due to first absorber to finalise its thickness. Also options for neutrons number reduction will also be undertaken by utilising new tools in simulation.

Bibliography

[1] M. Gell-Mann, Phys. Lett. **8**, 214 (1964).

[2] G. Zweig, CERN preprints TH-401 and TH-412 (1964).

[3] M. Breidenbach et al., Phys. Rev. Lett. **23**, 935 (1969).

[4] J.Schukraft and H.R Schmidt, J. Phys. **G 19**, 1705 (1993).

[5] F. Halzen and A. D. Martin, *Quarks and Leptons*, John Wiley & Sons (1984).

[6] D. H. Perkins, *Introduction to High Energy Physics*, 4th Ed. (2000).

[7] M. Schmelling, *Proceeding of XXVII International Conference on High Energy Physics*, Warsaw (1996).

[8] J. D. Wells, *Lectures on Higgs Boson Physics in the Standard Model and Beyond*, arXiv:0909.4541v1 [hep-ph] (2009).

[9] C. Amsler et al., Phys. Rev. Lett. **B 667**, 1 (2008).

[10] http://pdg.lbl.gov/2008/listings/q009.pdf

[11] D. Decamp et al., Phys. Lett. **B 231**, 519 (1989).

[12] A. Fisher, *Searching for the Beginning of Time: Cosmic Connection*, Popular Science, 238 (1991)

[13] J.D. Barrow, *The Origin of the Universe,* Science Masters Series (1997).

[14] http://www.fnal.gov/pub/inquiring/matter/madeof/index.html

[15] D.H. Perkins, *Particle Astrophysics*, Oxford University Press (2003).

[16] Morii et al, *The physics of the standard model and beyond*, World Scientific (2004).

[17] V. Barger and R. Phillips, *Collider Physics*, Addison Wesley (1997).

[18] T. Y. Wu and W.Y. Pauchy Hwang, *Relativistic quantum mechanics and quantum fields*, World Scientific (1991).

[19] T. Muta, *Foundations of quantum chromodynamics* (3rd ed.), World Scientific (2009).

[20] A. Smilga, *Lectures on quantum chromodynamics.* World Scientific (2001).

[21] Rohlf and J. William, *Modern Physics from α to Z^o* (1st ed.), Wiley (1994).

[22] H. Satz, Nucl. Phys. **A 418**, 447 (1984).

[23] C. Y. Wong, *Introduction to High-Energy Heavy-Ion Collisions*, World Scientific Publishing Company (1994).

[24] G. Baym, Nucl. Phys. **A 590**, 233 (1995).

[25] M. Alford, K. RajaGopal, and F. Wilczeck, Nucl. Phys. **B 537**, 443 (1998).

[26] T. Blum et al., Phys. Rev. **D 51**, 5153 (1995).

[27] M. Anselmino, *Strangeness and spin in fundamental physics*, IOP Press US (2008)

[28] J. Kapusta, P. Lichard, and D. Seibert, Phys. Rev. **D 44**, 2774 (1991).

[29] WA98 Collaboration, *Direct Photon Production in 158A GeV 208Pb+208Pb Collisions*, Phys. Rev. Lett. **85 (17)**, 3595 (2011).

[30] S. Drell and T.M.Yan, Phys. Rev. Lett. **25**, 316 (1970).

[31] E. V. Shuryak, Phys. Lett. **B 78**, 150 (1978).

[32] P. V. Ruuskanen, Nucl. Phys. **A 544**, 169 (1992).

[33] J. Kapusta, Nucl. Phys. **A 566**, 45 (1994).

[34] K. Kajantie, J. Kapusta, L. McLerran and A. Mekijan, Phys. Rev. **D 34**, 2746 (1986) .

[35] C. Gale and P. Lichard, Phys. Rev **D 49**, 3338 (1994).

[36] C. Song, C. M. Ko and C. Gale, Phys. Rev. **D 50**, 1827 (1994) .

[37] T. Matsui and H. Satz, Phys. Lett. **B 178**, 416 (1986).

[38] C. Baglin et al., Phys. Lett. **B 220**, 471 (1989).

[39] J. Rafelski and B. Muller, Phys. Rev.Lett. **48**, 1066 (1982).

[40] J. Rafelski and B. Muller, Phys. Rev.Lett. **56**, 2334 (1986).

[41] B. Muller and J. Rafelski, Phys. Rep. **142**, 167 (1986).

[42] J. Rafelski, Phys. Lett. **B 262**, 333 (1986).

[43] J. Rafelski, Phys. Rep. **88**, 331 (1982).

[44] Kenneth H. Hicks, *Strange Quarks in Hadrons, Nuclei, and Nuclear Matter*, World Scientific (2001).

[45] X-N. Wang and M. Gyulassy, Phys. Rev. Lett. **68**, 1480 (1992).

[46] M. Gyulassy and M. Plumer, Phys. Lett. **B 243,** 432 (1990).

[47] M. Gyulassy and X-N. Wang , Nucl. Phys. **A 590**, 511 (1995).

[48] http://cms.web.cern.ch/news/jet-quenching-observed-cms-heavy-ion-collisions

[49] M. Gyulassy , Nucl. Phys. **B 571**, 197 (2000).

[50] M. Gyulassy , Nucl. Phys. **A 661**, 637 (1999).

[51] C. Adler et al, Phys. Rev. Lett. **89**, 202301 (2002).

[52] K. Yagi, T. Hatsuda, and Y. Miake, *Quark-Gluon Plasma*, Cambridge University Press (2005).

[53] H. Heiselberg, Phys. Rep. **351**, 161 (2001).

[54] M. A. Stephanov, K. Rajagopal and E. Shuryak, Phys. Rev. Lett. **81**, 4816 (1998).

[55] M.M. Aggarwal et al. (WA98 Collaboration), Phys. Rev. **C 65**, 054912 (2002).

[56] S. Jeon and V. Koch, Phys. Rev. Lett. **85**, 2076 (2000).

[57] E. Shuryak and M.A. Stephanov, Phys. Rev. **C 63**, 064903 (2001).

[58] B. Mohanty, J. Alam, and T.K. Nayak, Phys. Rev. **C 67**, 024904 (2003). 633, 275 (2006). (2004). 72, 044902 (2005). 32, L37 (2006).

[59] F. Karsch, *Lattice Results on QCD Thermodynamics*, Nucl. Phys. **A 698**, 199 (2002).

[60] STAR Collaborations, Nucl. Phys. **A 757**, 102 (2005).

[61] J. D. Bjorken, Phys. Rev. **D 27**, 140 (1983).

[62] B. Friman, C. Hohne et al, *The CBM Physics Book*, Springer (2010).

[63] FAIR Baseline Technical Report, http://www.gsi.de/fair/reports/btr.html 865, 868, 877 (2006).

[64] T. Satogata et al., *RHIC Low-Energy Challenges and Plans*, PoS(CPOD07)**051**, 837, 864 (2007).

[65] A. Laszlo (NA60 collaboration), *NA61/SHINE at the CERN SPS*, Pos(CPOD07)**054**, 837, 864 (2007).

[66] V. Toneev, *The NICA/MPD Project at JINR (Dubna)*, Pos(CPOD07)**057**, 837, 864, 921 (2007).

[67] H. Morii et al., Nucl. Instr. and Meth. **A 526**, 399 (2004).

[68] http://www.gsi.de/forschung/fair_experiments/CBM/detector_e.html

[69] http://cbm-wiki.gsi.de/cgi-bin/view/Public/PublicMuon

[70] V. Friese et al., *The CBM Experiment at FAIR*, CBM Progress Report 2007 and 2008.

[71] J. M. Heuser, Nucl. Instrum. Meth. **A 582**, 910 (2007).

[72] C. Haohne, J. Phys. **G 35,** 104160 (2008).

[73] A. Dubey et al., *R&D with GEMs and THGEMs Towards Developing a Muon Tracker for CBM*, CBM Progress Report 2007 and 2008.

[74] D. Gonzålez-Diaz et al., *Progress in the CBM-TOF Wall: R&D and Simulation*, GSI Report 2007 and 2008.

[75] A. Akindinov et al., Nucl. Instrum. Meth. **A 572**, 676 (2007).

[76] A. Ivashkin, *Projectile Spectator Detector in CBM setup at SIS300, Talk given on the 1st CBM-Russia-JINR Collaboration Meeting in Dubna*, (2009).

[77] R. Rapp and J. Wambach, Adv. Nucl. Phys. **25**, 1 (2000).

[78] Z. Fodor, *Proc. Critical Point and Onset of Deconfinement, 4th International workshop*, GSI-DarmStadt Germany (2007).

[79] A. Delbert et. al., Nucl. Instrum. and Meth. **A 461**, 84 (2001).

[80] http://dx.doi.org/10.1016/0168-9002(96)00175-1

[81] J. P. Cussonneau et al., Nucl. Instr. and Meth. in Phys. Res. **A 419**, 452 (1998).

[82] I. Giomataris and G. Charpak, *Hadron Blind Detector(HBD),* NIM **A 310**, 589 (1991).

[83] http://cerncourier.com/cws/article/cern/44361

[84] http://www.compass.cern.ch/

[85] A. Dubey et al., CBM Progress Report 2010.

[86] N. H. Hamann et al., Nucl. Instr. and Meth. **A 346**, 57 (1994).

[87] S. Graessle et al., Nucl. Instr. and Meth. **A 367**, 138 (1995).

[88] K. Nuenighoff et al., Nucl. Instr. and Meth. **A 477**, 410 (2002).

[89] http://www.eudet.org

[90] I. V. Boguslavskiy1 et al., CBM Progress Report 2009.

[91] E. Kryshen and M. Ryzhinskiy, CBM Progress Report 2009.

[92] A. Prakash, P. P. Bhadhuri et al, *Proceeding of the DAE Symp. on Nucl. Phys.* **55** (2010).

[93] C. Hoehne, Quark Matter Proceedings(2008) to be published in J. Phys. G

[94] A. Prakash, P. P. Bhadhuri et al., CBM Progress Report 2010.

[95] A. S. Brogna et al, NIM **A 568**, 301 (2006).

[96] CBM-Progress Report 2006 p. 49.

[97] C. J. Schmidt1 et al, CBM Progress Report 2007 p. 48.

[98] N. Abel1 et al, CBM Progress Report 2007 p. 53.

[99] CBM Report by Peter Senger, April 2011.

[100] CBM Report 2012-01, *Nuclear matter physics at SIS-100*, p. 16-17.

[101] http://www.hades.gsi.de/computing/pluto

[102] A. K. Chaudhur, J. Phys. **G 35**, 095107(2008).

[103] G. E. Brown and M. Rho, Phys. Rev. Lett. **66**, 2720 (1991).

[104] M. Cheng et al., Phys. Rev. **D 74**, 054507 (2006).

[105] Y. Aoki, Z. Fodor, S. D. Katz, and K. K. Szabo, Phys. Lett. **B 643**, 46 (2006).

[106] K. Tsushima, D. H. Lu et al., Phys. Rev. **C 59**, 2824 (1999).

[107] A. Sibirtsev et al, Eur. Phys. J. **A 6**, 351 (1999).

[108] A. Hayashigaki, Phys. Lett. **B 487**, 96 (2000).

[109] A. Mishra, E. L. Bratkovskaya et al, Phys. Rev. **C70**, 044904 (2004).

[110] A. Andronic et al, Nucl. Phys. **A 715**, 529 (2003).

[111] S. Bass et. al., Nucl. Part. Phys **25**, 1859 (1999).

[112] H. van Hees and R. Rapp, *Medium Modifications of Vector Mesons and NA60,* arXiv:hep-ph/0604269v1.

[113] W. Cassing, E. Bratkovskaya, and A. Sibirtsev, Nucl. Phys. **A 786**, 183 (2007).

[114] A. Prakash et al., Nucl. Phys. **A 862-863**, 493 (2011).

[115] A Kiseleva et al., Indian J. Phys. **85(1),** 211 (2011).

[116] A. Kiseleva1 et al, *Optimization of the CBM muon detection system*, CBM Progress Report 2008 p. 27.

[117] http://cbmroot.gsi.de

[118] S. Bass, et al., Prog. Part. Nucl. Phys. **41**, 225 (1998).

[119] W. Cassing, E. Bratkovskaya, and S. Juchem, Nucl. Phys. **A 674**, 249 (2000).

[120] R. Brun, *GEANT - detector description and simulation tool*, CERN Program Library Long Writeup **W 5013**.

[121] M. Al-Turany, D. Bertini and I. Koenig, *Simulation and Analysis framework for CBM Experiment*, GSI Darmstadt Germany.

[122] D. Bertini et al., *The FAIR simulation and analysis framework", International Conference on Computing in High Energy and Nuclear Physics*, IOP **119**, 032011 (2008).

[123] http://www.cmake.org/

[124] A. Dellacqua et al., *Geant4: an object-oriented toolkit for simulation in HEP*, CERN/DRDC/**94-29** (1994).

[125] G. Cosmo et al., *Geant4: an object-oriented toolkit for simulation in HEP, LCRB Status Report,* CERN/LHCC/**95-70** (1995).

[126] T. Wenaus et al., *Geant4: an object-oriented toolkit for simulation in HEP, LCB Status Report*, CERN/LHCC/**97-40** (1997).

[127] S. Giani et al., *Geant4: an object-oriented toolkit for simulation in HEP, LCB Status Report*, CERN/LHCC/**98-44** (1998).

[128] GEANT4 Collaboration, *GEANT4: a simulation toolkit*, Elsevier Science **506** , 250 (2003).

[129] M. Bleicher et al., J. Phys. **G 25**, 1859 (1999).

[130] H. Petersen et al., *UrQMD-2.3 - Changes and Comparisons*, arXiv:0805.0567v1 [hep-ph].

[131] B. Andersson, G. Gustafson and B. Nilsson-Almqvist, Nucl. Phys. **B 28**1, 289 (1987).

[132] B. Nilsson-Almqvist and E. Stenlund, Comput. Phys. Commun. **43**, 387 (1987).

[133] T. Sjostrand, Comput. Phys. Commun. **82**, 74 (1994).

[134] K. Geiger, Phys. Rev. **D 46**, 4986 (1992).

[135] K. Geiger, Phys. Rept. **258**, 237 (1995).

[136] D. Molnar and M. Gyulassy, Nucl. Phys. **A 697**, 495 (2002).

[137] Z. W. Lin et al., Phys. Rev. **C 72**, 064901 (2005).

[138] Z. Xu and C. Greiner, Phys. Rev. **C 71**, 064901 (2005).

[139] L. Gerland et al., Phys. Rev. Lett. **8**1, 762 (1998).

[140] L. V. Bravina et al., Phys. Lett. **B 434**, 379 (1998).

[141] L. V. Bravina et al., Phys. Rev. **C 60**, 024904 (1999).

[142] S. A. Bass et al., Phys. Rev. Lett. **81**, 4092 (1998).

[143] M. Bleicher et al., Phys. Lett. **B 447**, 227 (1999).

[144] S. Soff et al., Phys. Lett. **B 471**, 89 (1999).

[145] C. Spieles et al., Eur. Phys. J. **C 5**, 349 (1998).

[146] C. Spieles et al., Phys. Rev. **C 60**, 054901 (1999).

[147] M. Bleicher et al., Phys. Lett. **B 435**, 9 (1998).

[148] M. Bleicher et al., Nucl. Phys. **A 638**, 391 (1998).

[149] L.D. Landau and E.M. Lifshitz, *Fluid Mechanics*, Pergamon Press (1959).

[150] H. Stocker, W. Greiner, Phys. Rep. **137**, 277 (1986).

[151] R. B. Clare, D. Strottman, Phys. Rep. **141**, 177 (1986).

[152] E. Schnedermann, J. Sollfrank, U. Heinz, Phys. Rev. **C 48**, c2462 (1993).

[153] J. Brachmann, A. Dumitru, J. Maruhn, H. Stocker, W. Greiner, and D. Rischke, Nucl. Phys. **A 619**, 391 (1997).

[154] B. Anderson et al, Phys. Rep. **97**, 31 (1983).

[155] K. Werner, Phys. Rep. **232**, 87 (1993).

[156] N. S. Amelin et al, Sov. J. Nucl. Phys. **51**, 327 (1990).

[157] H. Sorge, H. Stocker, W. Greiner, Ann. Phys. (N.Y.) **192**, 266 (1989).

[158] A. Capella et al, Phys. Rep. **236**, 227 (1994).

[159] M. Gyulassy and X. N. Wang, Comp. Phys. Commun. **83**, 307 (1994).

[160] J. Aichelin and H. Stocker, Phys. Lett. **B 176**, 14 (1986).

[161] C.M. Ko, Q. Li, R. Wang, Phys. Rev. Lett. **59**, 1048 (1987).

[162] W. Botermans and R. Malfliet, Phys. Rep. **198**, 115 (1990).

[163] W. Cassing and U. Mosel, Prog. Part. Nucl.Phys. **25**, 235 (1990).

[164] M. A. Kagarlis, GSI Report 2000-03 (2000).

[165] G. Agakichiev et al., Phys. Rev. Lett. **98**, 052302 (2007).

[166] P. Senger, Nucl. Part. Phys. **30**, 1087 (2004) .

[167] I. Froehlich et al., *Pluto:A Monte Carlo Simulation Tool for Hadronic Physics*, PoS ACAT2007:**076** (2007).

[168] PANDA Collaboration, *Hadron Physics with Anti-Protons: The PANDA Experiment at FAIR,* ECONF C070910:**123**, (2007).
B. Seitz [PANDA Collaboration], *The PANDA Project at FAIR*, Published in London, Deep inelastic scattering **232** (2008).

[169] V. Friese, Nucl. Phys. **A 774**, 377 (2006).
P. Senger, T. Galatyuk, D. Kresan, A. Kiseleva and E. Kryshen, *CBM at FAIR*, PoS CPOD2006, 018 (2006).

[170] A. Andronic et al., Phys. Lett. **B6 59**, 149 (2008).

[171] V. Friese, *The CBM Experiment at FAIR*, PoS CPOD07, 056 (2007).

[172] Indian CBM Collaboration, *Participation in the Compressed Baryonic Matter (CBM) experiment at FAIR*, CBM Technical Document (2008).

[173] CBM collaboration, *Compressed Baryonic Matter Experiment*, CBM Technical Status Report (2005).

[174] https://subversion.gsi.de/fairroot/release/DEC09

[175] http://pdg.lbl.gov/2011/mcdata/mc_particle_id_contents.html